

AD-A146 979

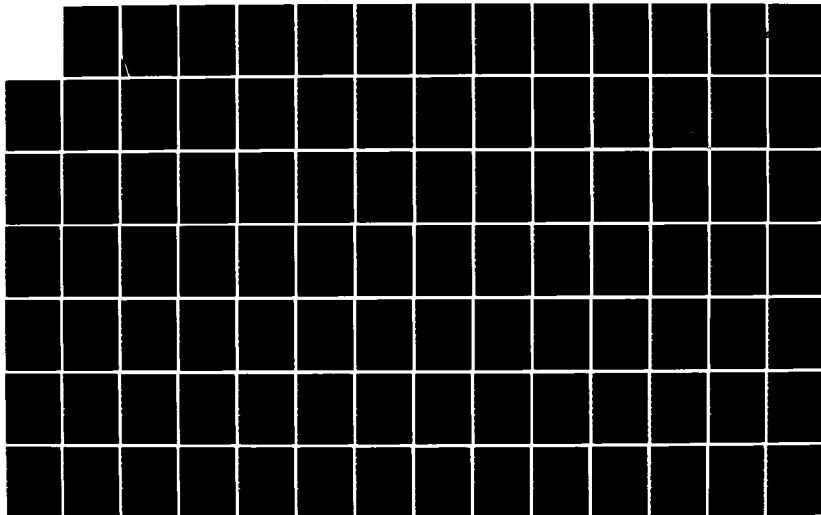
LASER ANNEALING OF ION IMPLANTED SEMICONDUCTORS(U)  
PARIS-6 UNIV (FRANCE) J F MORHANGE ET AL. JUL 84  
DAJA37-81-C-0587

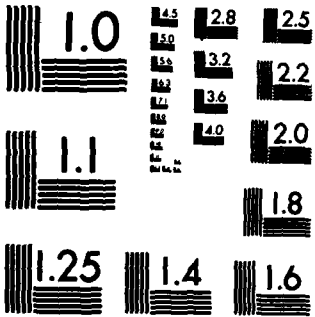
1/2

UNCLASSIFIED

F/G 28/12

NL





12

LASER ANNEALING OF ION IMPLANTED  
SEMICONDUCTORS

Final Technical Report

by

J-F. MORHANGE and M. BALKANSKI

July 1984

United States Army  
EUROPEAN RESEARCH OFFICE OF THE U.S. ARMY  
London England

CONTRACT NUMBER DAJA 3781C0587

DTIC  
SELECTED  
OCT 30 1984  
S E

Professor M. BALKANSKI  
Laboratoire de Physique des Solides - Paris

Approved for Public Release - distribution unlimited

AD-A146 979

Unclassified

SECURITY CLASSIFICATION OF THIS PAGE (When Data Entered)

REPORT DOCUMENTATION PAGE		READ INSTRUCTIONS BEFORE COMPLETING FORM	
1. REPORT NUMBER	2. GOVT ACCESSION NO.	3. RECIPIENT CATALOG NUMBER	
	AD-A146 979		
4. TITLE (and Subtitle)		5. TYPE OF REPORT & PERIOD COVERED	
Laser annealing of Ion Implanted Semiconductors		Final Technical Report July 84	
		6. PERFORMING ORG. REPORT NUMBER	
7. AUTHOR(s)		8. CONTRACT OR GRANT NUMBER(s)	
J.F. Morhange and M. Balkanski		DAJA37-81-C-0587	
9. PERFORMING ORGANIZATION NAME AND ADDRESS		10. PROGRAM ELEMENT, PROJECT, TASK AREA & WORK UNIT NUMBERS	
Universite Pierre et Marie Curie Laboratoire de Physique des Solides 4 Place Jussieu, Tour 13, 75230 Paris Cedex 05, France		61102A 1T161102BH57-05	
11. CONTROLLING OFFICE NAME AND ADDRESS		12. REPORT DATE	
ESABDSG-UK PO BOX 65 100 Hill 09510		July 1984	
		13. NUMBER OF PAGES	
		76	
14. MONITORING AGENCY NAME & ADDRESS (if different from Controlling Office)		15. SECURITY CLASS. (of this report)	
		Unclassified	
		15a. DECLASSIFICATION/DOWNGRADING SCHEDULE	
16. DISTRIBUTION STATEMENT (of this Report)			
Approved for public release; distribution unlimited.			
17. DISTRIBUTION STATEMENT (of the abstract entered in Block 20, if different from Report)			
18. SUPPLEMENTARY NOTES			
19. KEY WORDS (Continue on reverse side if necessary and identify by block number)			
LASER ANNEALING, RAMAN SCATTERING, SEMICONDUCTORS, SILICON, GALLIUM ARSENIDE, SUB-PICOSECONDE SPECTROSCOPY.			
20. ABSTRACT (Continue on reverse side if necessary and identify by block number)			
<p>The effect of laser annealing on implanted semiconductors (Silicon and Gallium Arsenide) has been studied by using Raman spectroscopy. Various properties are reported :</p> <p>The behaviour of the normal modes of Gallium Arsenide after laser annealing is interpreted with a theoretical model of the dynamic of vibration of a microcrystallite.</p> <p>The temperature at the spot of an Argon laser focussed onto</p>			



LASER ANNEALING OF ION IMPLANTED  
SEMICONDUCTORS

Final Technical Report

by

J-F. MORHANGE and M. BALKANSKI

July 1984

United States Army  
EUROPEAN RESEARCH OFFICE OF THE U.S. ARMY  
London England

CONTRACT NUMBER DAJA 3781C0587

Professor M. BALKANSKI  
Laboratoire de Physique des Solides - Paris

Approved for Public Release - distribution unlimited

Accession For	
NTIS GRA&I	<input checked="" type="checkbox"/>
DTIC TAB	<input type="checkbox"/>
Unannounced	<input type="checkbox"/>
Justification	
By _____	
Distribution/	
Availability Codes	
Dist	Avail and/or Special
A-1	

↓  
TABLE OF CONTENTS :

1. INTRODUCTION.....	1
2. RAMAN SPECTROSCOPY OF GaAs AMORPHOUS OF CRYSTALLINE TRANSITION INDUCED BY LASER ANNEALING;.....	2
2.1. Experimental techniques.....	2
2.2. Experimental results.....	3
3. THE VIBRATION OF A GALLIUM ARSENIDE MICROCRISTALLITE;.	5
3.1. Lattice dynamics of a thin ionic slab of GaAs....	5
3.2. Results and discussion.....	7
4. EXPERIMENTAL DETERMINATION OF THE TEMPERATURE OF SILICON AT THE SPOT OF A CONTINUOUS LASER;.....	8
4.1. The Stokes to anti-Stokes ratio.....	8
4.2. Anharmonic properties of Silicon.....	10
4.3. Temperature of a thin layer of Silicon under continuous laser irradiation.....	13
4.3.1. Fused Silica substrate.....	14
4.3.2. Silicon substrate.....	14
5. RAMAN SPECTROSCOPY OF VERY HEAVILY DOPED SILICON;.....	14
5.1. The vibrational modes introduced by the defects...	15
5.2. Free carriers-phonons interaction in heavily doped Silicon.....	15
5.3. Experimental results.....	16
5.3.1. Laser annealing of p doped Silicon.....	16
5.3.2. Laser annealing of compensated Silicon.....	17
5.3.3. Laser annealing of n doped Silicon.....	18
6. SUB-PICOSECOND SPECTROSCOPY.....	20
6.1. The sub-picosecond optical source.....	20
6.2. Characterization of the source oscillator.....	21
7. DISCUSSION AND CONCLUSION.....	22
References	
Annexes	

LASER ANNEALING OF ION IMPLANTED SEMICONDUCTORS.  
MECHANISM OF AMORPHOUS CRYSTALLINE TRANSITION.

1. INTRODUCTION

One of the most fascinating debates in the field of Semiconductors Physics in recent years, centers on the fundamental interpretation of laser annealing. The question of the energy transfer from an intense beam to a disordered material, such as amorphous silicon, resulting in the crystallization of the amorphous substance has been approached from two different points of view, both referring to a set of fairly clear experimental results. On one hand, a claim has been made that the laser beam simply heats the sample up to melting the amorphous material which on cooling crystallizes from melt<sup>(1-4)</sup>. On the other hand, one has considered that amorphous to crystalline phase transition can occur at low temperatures without passing through the molten state<sup>(5)</sup>. Many arguments have been developed in support of these interpretations. A large number of publications have appeared in the literature.

The results we are reporting here constitute a contribution toward the elucidation of the mechanism of amorphous to crystalline transition. Our effort has been focussed on the two extreme time scales : infinite time observation of the structural modifications which have been retained after laser annealing and very short time : the evolution of the system in the femtosecond range. We have attempted to correlate the steady state observations with the sub-picosecond modification of the system. If the general conclusion is that random nucleation in the high density plasma fluid state governs the final crystallization of the system, we are using essential links to demonstrate such an opinion. The description of the system in the highly excited non linear regime maintained during the irradiation of 100 fs is not available. The description of the relaxation processes in the fs range is not clearly established. The relation between the excited short living fluid and melting is not known. The theory of melting and recrystallization in this regime is not established.

We are presenting here a great deal of interesting and important results. They are contributing to ask the right questions more than they have solved the essential problems. As a result of this effort nevertheless, we are convinced today that the radiation energy introduced into the condensed matter is retained in a highly excited phase with more than  $10^{22}$  antibonding states as long as the radiation field continues to arrive on the system. The evolution of this particular fluid is the interesting question with which one should be concerned now.

In addition to the fundamental interest, laser annealing has been considered to have a strong potential in the technology of semiconductor doping by ion implantation. For all these reasons, the attention of a large audience has been focussed on this problem.

We believe that the results, we are presenting here show the possibilities and set the limits of the use of laser annealing in the semiconductor technology.

## 2. RAMAN SPECTROSCOPY OF GALLIUM ARSENIDE AMORPHOUS TO CRYSTALLINE TRANSITION INDUCED BY LASER ANNEALING.

Raman spectroscopy of laser annealed semiconductors rendered amorphous by ion implantation gives the possibility to follow the recrystallization of the material. This technique which has successfully been applied to silicon<sup>(6,7)</sup> can as well be used to characterize ionic semiconductors as Gallium Arsenide.

### 2.1. Experimental techniques:

Semi insulating GaAs have been implanted and laser annealed at the Laboratoire Central de Recherches de la Thomson C.S.F. (Corbeville). The dose chosen was  $2 \cdot 10^{14} \text{As/cm}^2 + 2 \cdot 10^{14} \text{Ga/cm}^2$  under 300keV in order to keep a correct stoichiometry in the samples. Laser annealing was achieved by using a YAG laser equipped with a frequency doubler. This laser delivers energy pulses in the energy range 0.3 to  $0.6 \text{J/cm}^2$  at a wavelength of 530nm. Raman spectra were recorded by using the 488nm line of an Argon laser. The diameter of the spot of the Argon laser was of the order of 80  $\mu\text{m}$ . This size, compared to the 1mm diameter spot of the YAG laser permits a rather good Raman characterization of all the surface of the annealed

region by sweeping the Raman laser spot inside the annealed zone.

## 2.2. Experimental results.

Figures 1 and 2 present the Raman spectra of two GaAs samples in a backscattering geometry on faces (100) and (110). On these two different faces, the selection rules are complementary, the TO phonon being forbidden on the (100) face, the LO phonon forbidden on the (110) face. For perfectly crystalline samples, the selection rules are verified, the residual forbidden peaks in each case are due to residual misalignment. The frequencies of the lines are respectively  $\omega_{TO} = 268 \text{ cm}^{-1}$ ,  $\omega_{LO} = 291 \text{ cm}^{-1}$ , their widths, measured with an instrumental resolution of  $2 \text{ cm}^{-1}$ , is equal to  $3.6 \text{ cm}^{-1}$  for both peaks. After an implantation of  $2.10^{14}$  ion Gallium per  $\text{cm}^2$  and  $2.10^{14}$  ion Arsenic per  $\text{cm}^2$ , the samples are rendered amorphous and the spectra observed are typical for this kind of amorphous material (8) i.e. a density of states spectrum.

After laser annealing, the spectra are drastically modified. For a low energy density, the forbidden peaks are respectively activated for each face ; this is especially spectacular for the (100) face for which the forbidden TO is larger than the allowed LO. Moreover, the frequencies of these peaks are shifted towards the low frequency region and their widths are broadened to more than  $6 \text{ cm}^{-1}$ . As the annealing energy is increased, the forbidden peaks intensities tend to decrease, their frequency shift and their widths reduce. However, the normal characteristic are not completely recovered at  $0.6 \text{ J/cm}^2$  especially for the (100) face.

The spectacular behaviour of the (100) face for low energy annealing has lead us to study the Raman spectra at the periphery of the annealed zone by sweeping the Raman laser spot across the limit of the annealed region where the irradiation energy continuously varies.

As can be seen in Figure 3, the spectra are continuously modified, the amorphous band at  $250 \text{ cm}^{-1}$  shifts and get structured changing into the TO phonon. The allowed LO phonon appears only as a shoulder on this band. The polarization analysis has been made on the (100) face sample, with the incident electric field parallel to the  $\langle 011 \rangle$  axe, the scattered field been either parallel or perpendicular to

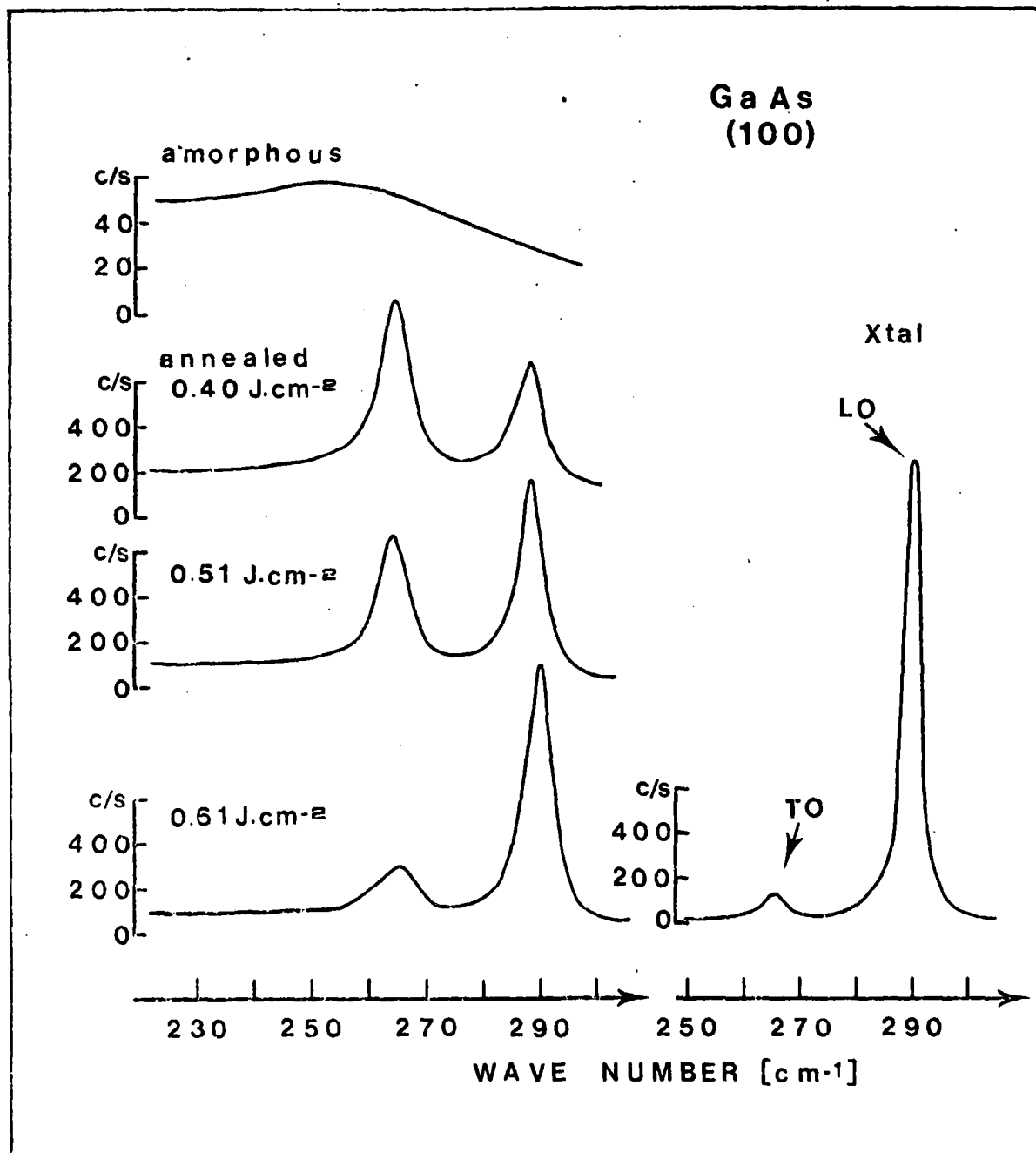


**Figure 1** : Raman spectra of a laser annealed sample of GaAs(100) for various energy densities.

the incident field. For this last polarization both peaks TO and LO are forbidden in a perfectly crystalline sample whereas the LO phonon normally appears when both fields are parallel. In Figure 4, it can be seen that the selection rules are well observed when the analysis is made at the center of the annealed zone but are not at the intermediate region, where spectra are rather identical for both polarization.

The more important feature presented here seems to be the gradual transition from the amorphous spectrum to a crystalline one. This fact involves a continuous variation of the degree of order versus the annealing density energy. The late apparition of the longitudinal optical phonon when increasing the annealing energy confort this hypothesis as the existence of this phonon is due to long range Coulombian forces. A way of understanding such a continuous variation is to consider the presence of microcrystallites in the annealed region. Such crystallites have yet been observed in laser annealed Silicon and Gallium Arsenide<sup>(9,10)</sup>. There are very few published results on Raman spectroscopy of small crystals. The only extensively studied case is the graphite<sup>(11)</sup> where only very small size crystallites are available. In this material, new peaks as well as a shift of the high frequency  $E_{2g}$  first order peak are reported and attributed to the wave vector selection rules relaxation. The shift observed is toward the high frequency region. This is not contradictory with our observation of a low frequency shift in GaAs if the special shape of the dispersion curves of graphite is considered. In this material, the highest branch of the dispersion curves reaches a region of higher frequency ( $\sim 1600 \text{ cm}^{-1}$ ), than the zone center  $E_{2g}$  mode ( $1581 \text{ cm}^{-1}$ )<sup>(12)</sup>. Furthermore, this  $E_{2g}$  mode is transformed into a band situated at higher frequency ( $1600 \text{ cm}^{-1}$ ) in the amorphous state of graphite (glassy Carbon) which is an opposite behaviour as compared to GaAs or Si.

Only a complete calculation of the lattice dynamic of a microcrystallite would fully justify the hypothesis of the size effect. A similar computation has already be done at the laboratory on Silicon<sup>(2)</sup>. The extension of this model to GaAs is not straightforward because of the presence of the long range Coulombian forces which ensure the stability of this ionic crystal. This extension is the object of the following chapter.

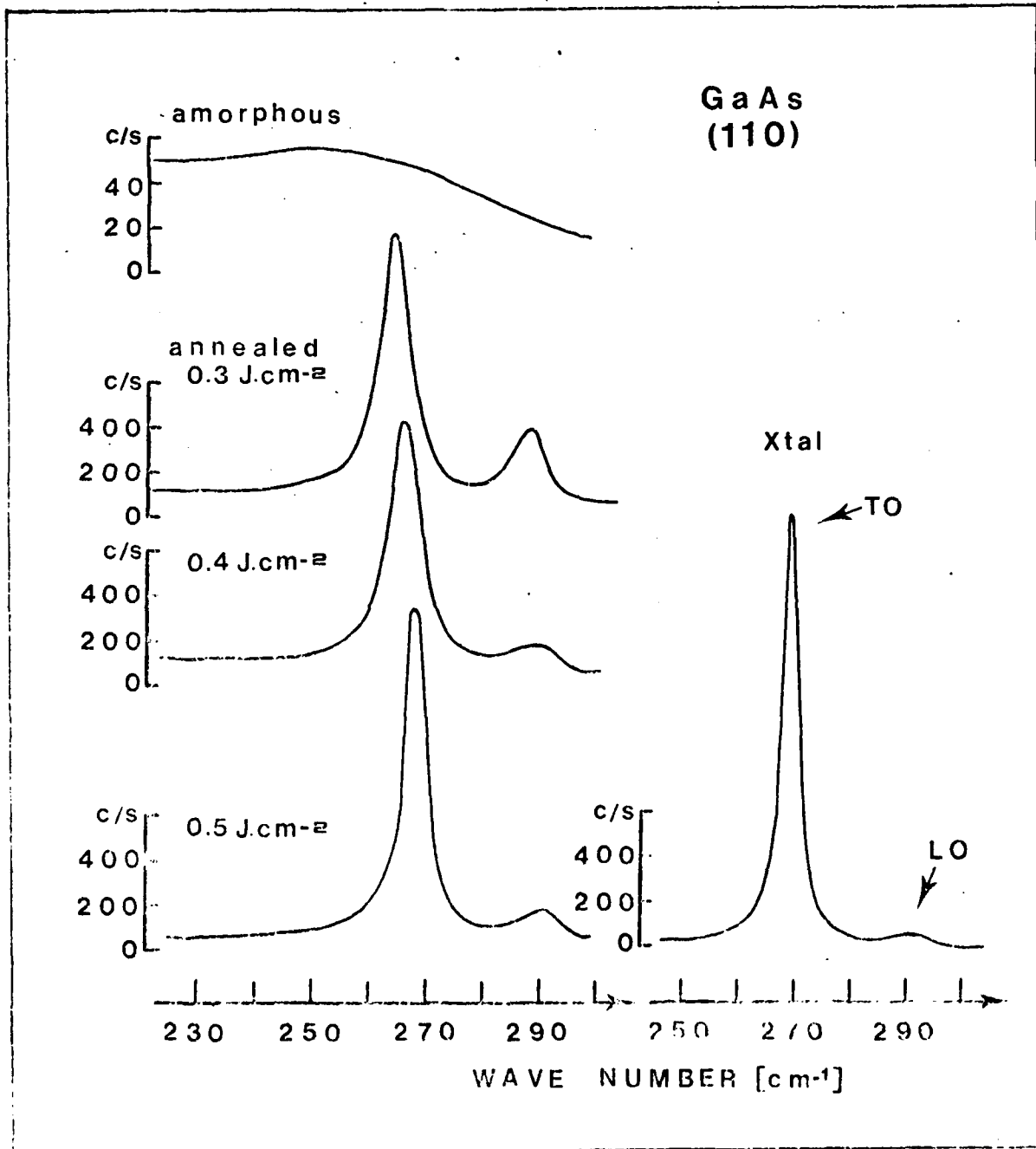


Figure 2 : Raman spectra of a laser annealed sample of GaAs(110) for various energy densities.

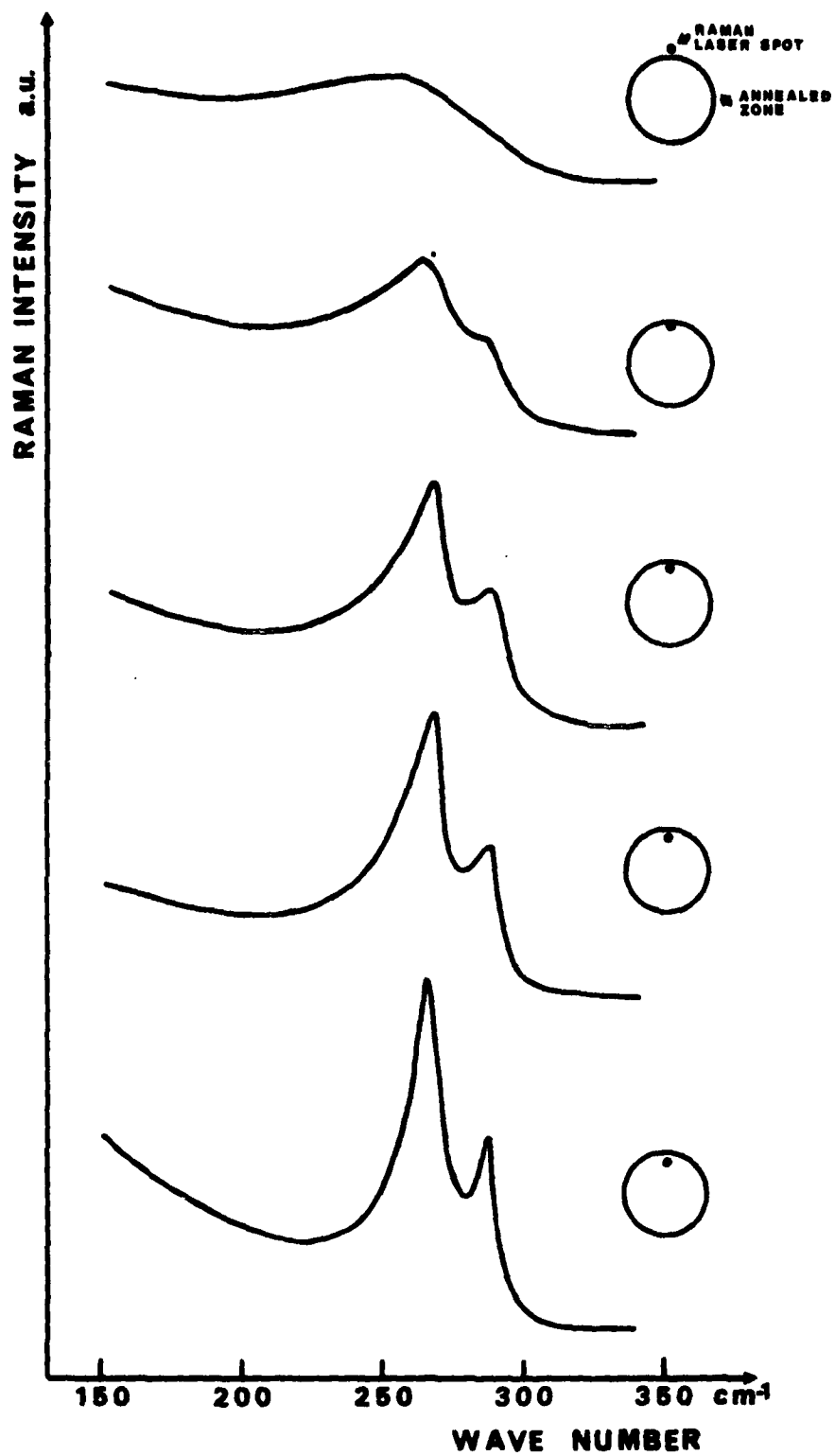


Figure 3 : Raman spectra of a laser annealed sample of GaAs(100) at the edge of the annealed zone.

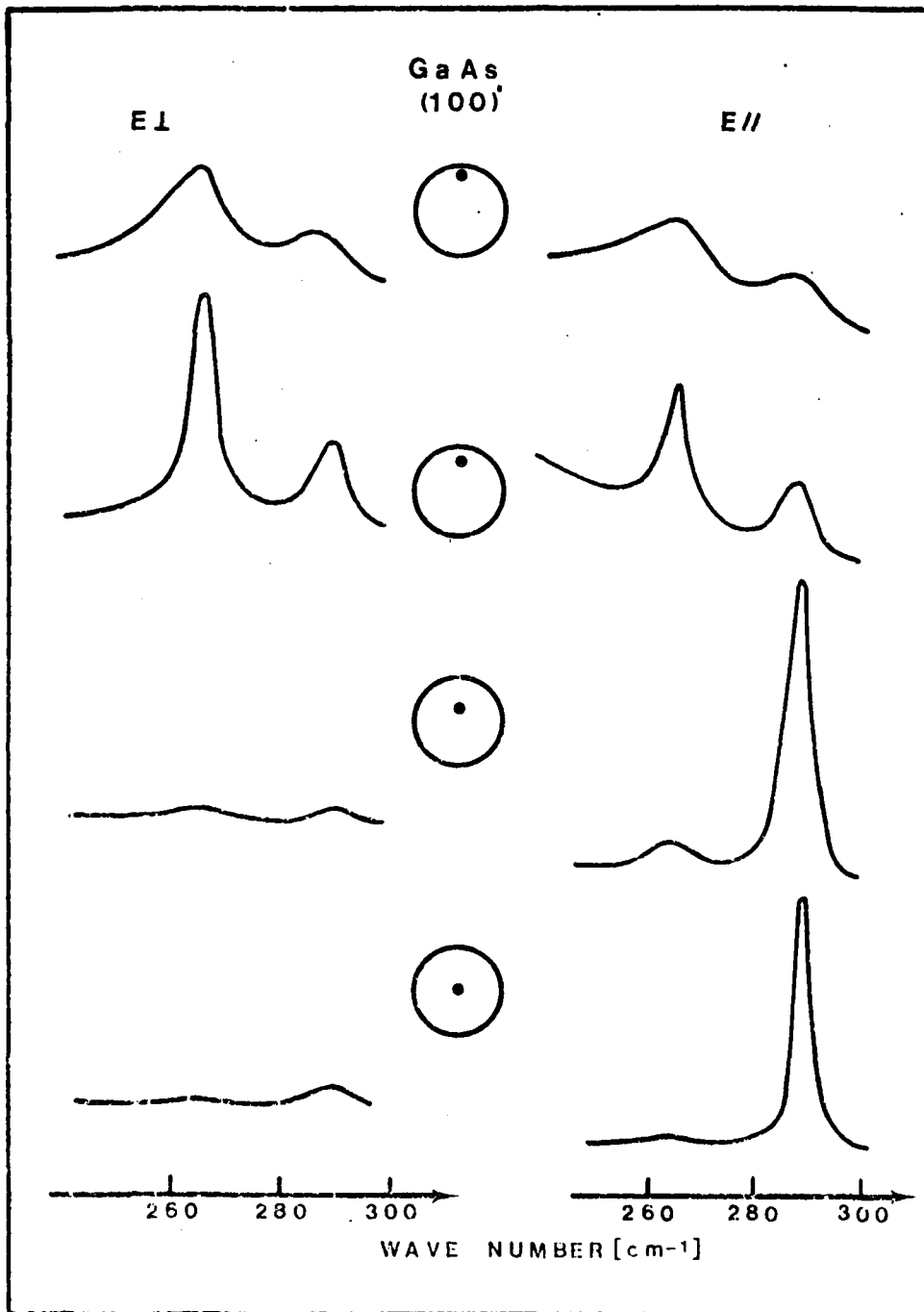


Figure 4 : Raman spectra of a laser annealed sample of GaAs (100) from various points of the sample. The incident field is parallel to a  $\langle 100 \text{ axis} \rangle$ , the scattered field is perpendicular or parallel to the incident field.

### 3. THE VIBRATIONS OF A GALLIUM ARSENIDE MICROCRISTALLITE.

#### 3.1. Lattice dynamics of thin ionic slab of GaAs.

The complete calculation is presented in three publications added in annexe (A1). We just summarize here the method and the results.

A full lattice dynamics of a microcrystallite is outside our possibilities as it should need the exact knowledge of the geometric shape of the grain and as it would need the diagonalization of matrix of order  $3N$  where  $N$  is the number of atoms inside the crystallite. Even for very small crystallites  $N$  exceeds some thousands so that computation duration should be excessive. That is the reason for which the crystallite has been modeled by a thin layer of material infinite along two dimensions and finite along the third. The finite dimension should be sufficient to introduce a shift on the frequencies of vibration as compared to a crystal infinite along 3 dimensions.

To resolve this problem, it is necessary to solve the equations of motion of the atoms of the slab, that is to say to diagonalize the corresponding dynamical matrix. To simplify the problem, the choice of a crystallographic orientation of the slab is of premium importance as symmetry consideration can reduce the computation. In our case, the slab is parallel to the plane (111). With classical notations, the equation of motion are :

$$m_k \ddot{u}_\alpha(1k) = - \sum_{1'k'\beta} \phi_{\alpha\beta}(1k;1'k') u_\beta(1'k') \quad (1)$$

The slab being infinite along two dimensions, the cyclic condition of Born Van Karman can be applied along these two directions. The solution of equation (1) can be expressed in the form :

$$u_\alpha(1k) = \frac{v_\alpha(13k)}{m_k^{1/2}} \exp\{-i\omega t + 2\pi i \bar{y} \cdot \bar{x}(1k)\} \quad (2)$$

where the vector  $v(l_3, K)$  depends only on  $l_3$  the parameter which labels the cells along the limited dimension.

$y$  is a two dimensional vector of the two dimensions Brillouin zone associated to the structure. By reporting (2) into (1), we obtain :

$$\omega^2 v_\alpha(l_3 k) = \sum_{l'_3 k' \beta} \sum D_{\alpha\beta}(l_3 k; l'_3 k' | \bar{y}) v_\beta(l'_3 k') \quad (3)$$

with

$$D_{\alpha\beta}(l_3 k; l'_3 k' | \bar{y}) = \sum_{l_1 l_2} \frac{\phi_{\alpha\beta}(l k; l' k')}{(m_k m_{k'})^{1/2}} \exp\{2\pi i \bar{y} \cdot \bar{x}(l k; l' k')\} \quad (4)$$

$D_{\alpha\beta}$  is the dynamical matrix,  $\phi_{\alpha\beta}$  being the matrix of force constants.

Since cyclic boundary condition does not apply to the limited dimension, no further reduction is possible except those associated to symmetry considerations. Under these consideration the  $3 \times 3$  matrixes  $D(l_3, K, l'_3, K')$  which describe the interactions between the plane lattices take the form :

$$D(l_3, K, l'_3, K') = \begin{pmatrix} A-B & 0 & 0 \\ 0 & A-B & 0 \\ 0 & 0 & A+2B \end{pmatrix}$$

which shows that the modes of vibration can be separated in two groups, one doubly degenerated which describes the vibrations parallel to the slab, the other non degenerated which describes the vibrations perpendicular to the slab.

To go further, we need now to choose a model of force constants. The long range interactions and the short range interactions must be processed differently as it is well known that Coulombian forces introduce discontinuity.

For short range interaction, the model chosen is the Valence Force Field force constants with 10 parameters describing the linear and angular bondings between first and second neighbours. The potential energy for this model take the form :

$$\begin{aligned} \phi = & r_0^\xi \sum_{\text{Ga-As}} \Delta r_{ij} + \frac{\lambda}{2} \sum_{\text{Ga-As}} (\Delta r_{ij})^2 + r_1^\rho \sum_{\text{Ga-Ga}} \Delta r_{ik} + \\ & + \frac{\mu}{2} \sum_{\text{Ga-Ga}} (\Delta r_{ik})^2 + r_1^\sigma \sum_{\text{As-As}} \Delta r_{j1} + \frac{\nu}{2} \sum_{\text{As-As}} (\Delta r_{j1})^2 + \\ & + \frac{k_\theta r_0^2}{2} \sum_{\text{As-Ga-As}} (\Delta \theta_{jil})^2 + \frac{k'_\theta r_0^2}{2} \sum_{\text{Ga-As-Ga}} (\Delta \theta_{ijk})^2 + \\ & + \frac{k_{rr}}{2} \sum_{\text{As-Ga-As}} \Delta r_{ji} r_{i1} + \frac{k'_{rr}}{2} \sum_{\text{Ga-As-Ga}} \Delta r_{ij} \Delta r_{jk}, \end{aligned}$$

where  $\xi, \lambda, \rho, \mu, \sigma, \nu, k_\theta, k'_\theta, k'_{rr}$  are the ten parameters and  $r_0$  and  $r_1$  the first and second nearest neighbour distances.

### 3.2. Results and discussion.

The frequencies of vibrational modes of a thin slabs have been calculated for a thickness varying from 2 to 25 unity cells.

The Figure 5 shows the variation of frequency of six modes versus the thickness of slabs. These modes are grouped in two optical modes (TO and LO) and four surface modes. The two optical modes are the more interesting as they are the modes that correspond to the Raman active TO and LO modes in the limit of large number of unit cells (infinite crystal). As can be seen, the frequencies of these modes tend very rapidly to their limits. After 10 unit cells the frequencies have reached a stable value corresponding to the frequencies of the infinite crystal. For a small number of cells than ten, the frequencies of the TO and LO modes are inferior to the bulk frequencies, result which correlates the Raman spectra observed. The surface modes are not easily seen by Raman spectroscopy so that their interest is only theoretic

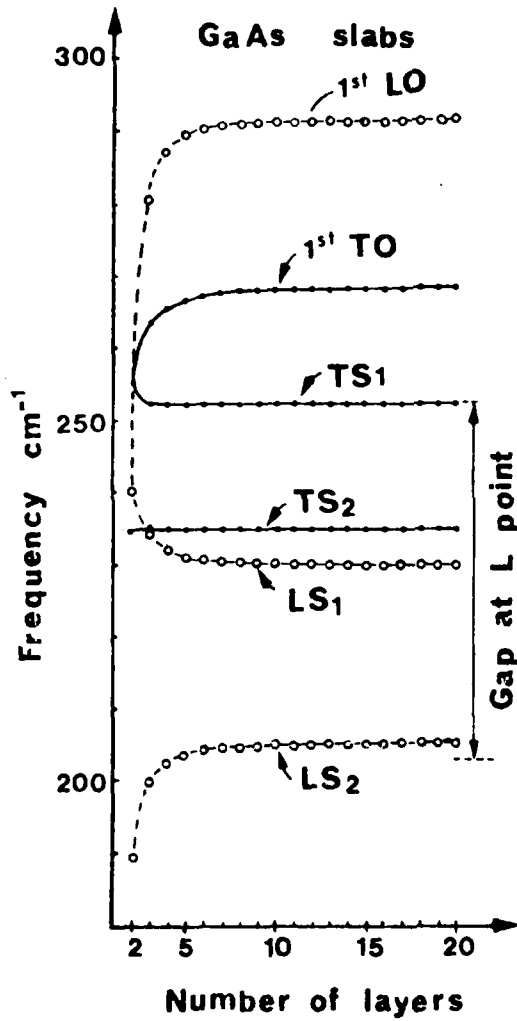
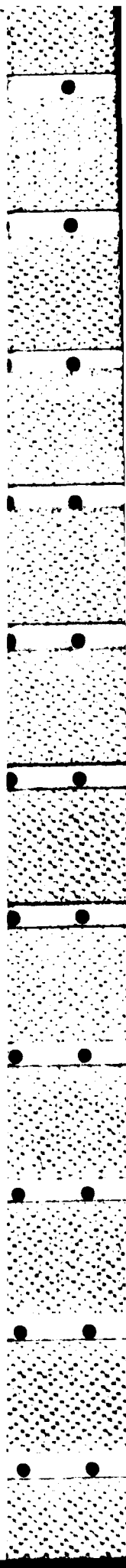


Figure 5 : Frequency variation of vibrational modes versus the thickness of the slab.



as they cannot be compared to experimental results. Another interesting theoretical deduction is that for a given slab of definite thickness, all the modes except the surface ones, fall on the dispersion curves of the infinite structure of GaAs (Fig.6). The four missing point at the edge of the Brillouin zone correspond to the four surface modes. These surface modes can thus be considered as a superposition of the four missing modes. This fact implies that the continuum of frequencies obtained by several authors when calculating solution for different wavevectors on the plane of the slab, is the projection of the dispersion surface on the two dimensional Brillouin zone.

#### 4. EXPERIMENTAL DETERMINATION OF THE TEMPERATURE OF SILICON AT THE SPOT OF A CONTINUOUS LASER.

The possibility to characterize the laser annealing during the impulsion by using the Raman spectroscopy was evidenced by Compaan et al.<sup>(13)</sup>. Their measures showed that the temperature reached immediately after the end of the pulse was of the order of 400°C. This result, which is still controverted, is the last experimental evidence for a non thermal annealing during manosecond scale. To test the validity of this kind of measurements, we have measured the temperature of a Silicon sample during a continuous laser irradiation by using Raman spectroscopy. Three quantities have been studied : the Stokes to anti-Stokes ratio, the shift of the normal mode and the broadening of the normal mode.

##### 4.1. The Stokes to anti-Stokes ratio.

Raman scattering consists of an inelastic scattering of the light by quantified excitations. In the case of a semiconductor, the elementary excitations responsible of the scattering are the phonons. Two processes coexist in the scattering.

In the Stokes process, incident photons of frequency  $\omega_i$  create phonons of frequency  $\Omega$  and are scattered with a frequency  $\omega_s = \omega_i - \Omega$ .

In the anti-Stokes process, the incident photons interact and annihilate the phonons and are scattered with a frequency  $\omega_{AS} = \omega_i + \Omega$ .

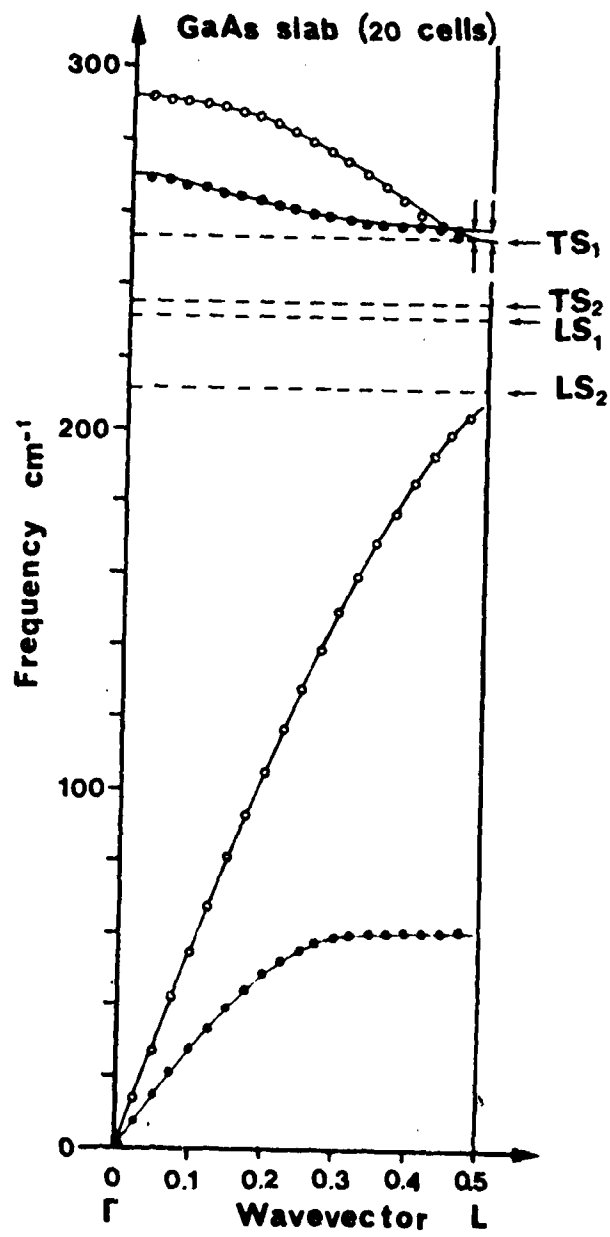


Figure 6 : Phonon dispersion curves of GaAs along the  $\Lambda$  direction for a 20 layers thick slab.

Raman spectra are thus formed by a set of peaks symmetrically disposed in comparison with the incident frequency  $\omega_i$ . The intensity ratio of these two processes is governed by the statistic of Bose-Einstein :

$$\frac{I_s}{I_{As}} = \frac{n+1}{n} \quad \text{where } n = 1 / (\exp|\hbar\Omega/kT|-1)$$

In fact, this term only describes the thermodynamical part of the intensity ratio and in order to be accurate, it is necessary to take into account some corrective terms.

First, the Raman effect is a scattering phenomenon and then, the scattered intensity varies as the fourth power of the frequency of the incident light. More precisely, it varies as the product  $\omega_i \cdot \omega_s^3$  where  $\omega_i$  and  $\omega_s$  are the incident and scattered frequencies ( $\omega_s = \omega_i - \Omega$ ,  $\Omega$  being the phonon frequency). This term introduces the corrective factor  $(\omega_s/\omega_{As})^3$  which is temperature independent.

Another dependence upon the incident frequency is due to a resonance effect. Raman scattering intensity increases as the incident light comes close to the direct gap of the material. This resonance term is difficult to compute so we have chosen to use experimental results obtained at the laboratory<sup>(14)</sup>. This corrective factor  $\frac{S(\omega_i, \omega_s)}{S(\omega_i, \omega_{As})}$  is temperature dependent by the intermediary of the energy gap variation. However, this temperature dependence can be neglected when the energy gap is far from the energy of incident wavelength which is the case in our conditions.

A third correction is due to the difference between the values of the absorption coefficient at the incident and scattered energy. This gives a correction of the form :

$$\frac{\alpha_i + \alpha_{As}}{\alpha_i + \alpha_{As}}$$

Besides all those theoretical corrections, there is an experimental correction induced by the variation of the overall response of the spectrometer. This factor K can be measured with a standard spectral lamp. With all these corrective factors, the ratio of Stokes to anti-Stokes intensities is expressed by the equation :

$$\frac{I_s}{I_{As}} = \frac{\alpha_i + \alpha_{As}}{\alpha_i + \alpha_s} \left(\frac{\omega_s}{\omega_{As}}\right)^3 \cdot \frac{S(\omega_i, \omega_s)}{S(\omega_i, \omega_{As})} \cdot \exp\left(\frac{h\omega}{kT}\right)$$

In the case of Silicon, the entire correction has been computed and for an energy of  $\omega_i$  of  $20.492 \text{ cm}^{-1}$  is equal to 0.83.

$$\frac{I_s}{I_{As}} = 0.83 \frac{n+1}{n} = 0.83 \exp\left(\frac{h\Omega}{kT}\right)$$

A measure of the Raman intensities of Stokes and anti-Stokes peaks versus temperature has been realized on a Silicon heated in an oven. The points on Figure 7 represent the ratio of  $I_{As}/I_s$ . On the same figure is represented by a continuous line the theoretical function  $I_{As}/I_s = 1.2 \exp(-748.3/T)$ . As can be seen on the figure, the fit is only good at low temperature. At high temperature, this curve is significantly lower than the experimental points. The reasons of this discrepancy is the incertitude on some of the coefficients which form the correction stated above. In order to increase the precision of the measure, we have chosen to realize a least square best fit of the experimental results with a theoretical curve of the form :

$I_{As}/I_s = A \exp(-748.3/T)$  where A is the parameter to be adjusted. This computation gives a value for A of 1.284 so that we can practically measure the temperature by using the formula :

$$I_{As}/I_s = 1.284 \exp(-748.3/T)$$

This curve is represented on Figure 7 by the interrupted line. The temperature obtained by this method is exact with a precision of about 20 %.

#### 4.2. Anharmonic properties of Silicon.

The ratio between the Stokes and anti-Stokes intensities is not the only quantity which can be used to determine the temperature. Anharmonic properties which involve a shift and a widening of the Raman peaks can be also used. These effects are due to interaction between phonons. The simpler model<sup>(15, 16)</sup> supposes that the optical phonon annihilates giving rise to two acoustical phonons with half

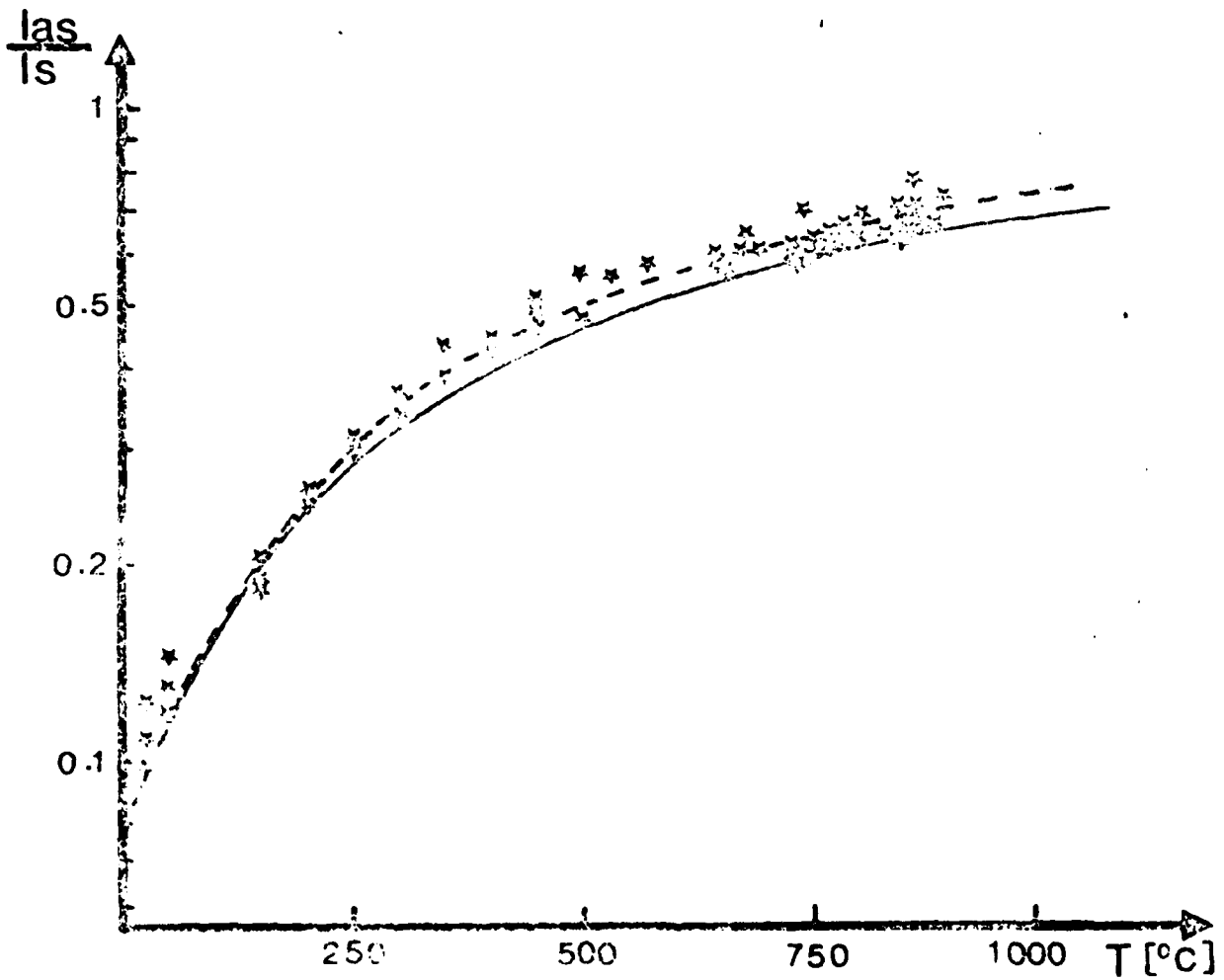


Figure 7 : Intensity ratio of anti-Stokes to Stokes Raman peaks of Silicon versus temperature. Stars correspond to experimental points.

the frequency of the optical mode. In this case, the width of the optical phonon responsible of the Raman peak can be evaluated to :

$$\Gamma(T) = \Gamma(0) \left| 1 + \frac{2}{e^x - 1} \right| \quad (1)$$

The damping constant and the frequency shift have been investigated systematically as a function of temperature. Figure 8 gives the temperature variation of the damping constant  $\Gamma(T)$  between 5 and 1400K. The dashed curve represents  $\Gamma(T)$  calculated from the relation.

This equation (1) is an approximate expression for the temperature dependence of the damping constant based on three-phonon processes (cubic anharmonicity in second order) and the simple Klemens model<sup>(16)</sup>. It seriously underestimates the damping constant at high temperatures. We attribute this discrepancy at least in part to the neglect of four-phonon processes.

It is of interest to investigate whether this discrepancy can be eliminated by generalizing Equation 1 to include the contribution of four-phonon processes. Following the approach of Klemens<sup>(11)</sup>, we write the kinetic equation for the net rate of decay of an incident phonon into three thermal phonons in the form :

$$\begin{aligned} \frac{d}{dt} (\delta n_0) = & -B \left[ (\delta n_0 + n_0)(n_1 + 1)(n_2 + 1)(n_3 + 1) \right. \\ & \left. - (\delta n_0 + n_3 + 1)n_1 n_2 n_3 \right], \end{aligned} \quad (2)$$

where  $\delta n_0$  is the deviation of the incident phonon occupation number from its thermal equilibrium value  $n_0$  and B is a constant. Using the equilibrium condition :

$$n_0(n_1 + 1)(n_2 + 1)(n_3 + 1) - (n_0 + 1)n_1 n_2 n_3 = 0, \quad (3)$$

We can rewrite Eq.(3.5) as :

$$\frac{d}{dT} (\delta n_0) = B(n_1 n_2 + n_1 n_3 + n_2 n_3 + n_1 + n_2 + n_3 + 1) \delta n_0. \quad (4)$$

Energy conservation can be satisfied in the simple Klemens fashion by setting  $\omega_1 = \omega_2 = \omega_3 = \omega_0/3$ . Consequently,  $n_1 = n_2 = n_3$ . The generalization of Eq.(3.4) to four-phonon processes then takes the form :

$$\Gamma(T) = A \left( 1 + \frac{2}{e^x - 1} \right) + B \left( 1 + \frac{3}{e^y - 1} + \frac{3}{(e^y - 1)^2} \right) \quad (5)$$

Where  $y = \hbar\omega_0/3K_B T$  and A and B are constants. In the high-temperature limit, the factors multiplying A and B in Eq.(5) vary as T and  $T^2$ , respectively.

Equation (5) has been used to fit the experimental data presented in Figure 8 by suitably choosing the constants A and B. The best values of A and B are found to be 1.295 and  $0.105 \text{ cm}^{-1}$ , respectively, and the resulting plot of  $\Gamma(T)$  vs T is given by the solid curve in Figure 8. We see that the agreement between the calculated curve and the experimental points is now quite good.

The experimental results for the line position  $\Omega(T)$  as a function of T are shown in Figure 9. Also shown is the fit to the data (solid curve) specified by the expressions :

$$\Omega(T) = \omega_0 + \Delta(T) \quad (6)$$

and

$$\Delta(T) = C \left( 1 + \frac{2}{e^x - 1} \right) + D \left( 1 + \frac{3}{e^y - 1} + \frac{3}{(e^y - 1)^2} \right), \quad (7)$$

Where  $\omega_0$ , C and D are constants with the values 528, - 2.96, and  $- 0.174 \text{ cm}^{-1}$ , respectively. Equation (7) is the analog of Equation (5) and specifies the contributions of three-phonon and four-phonon

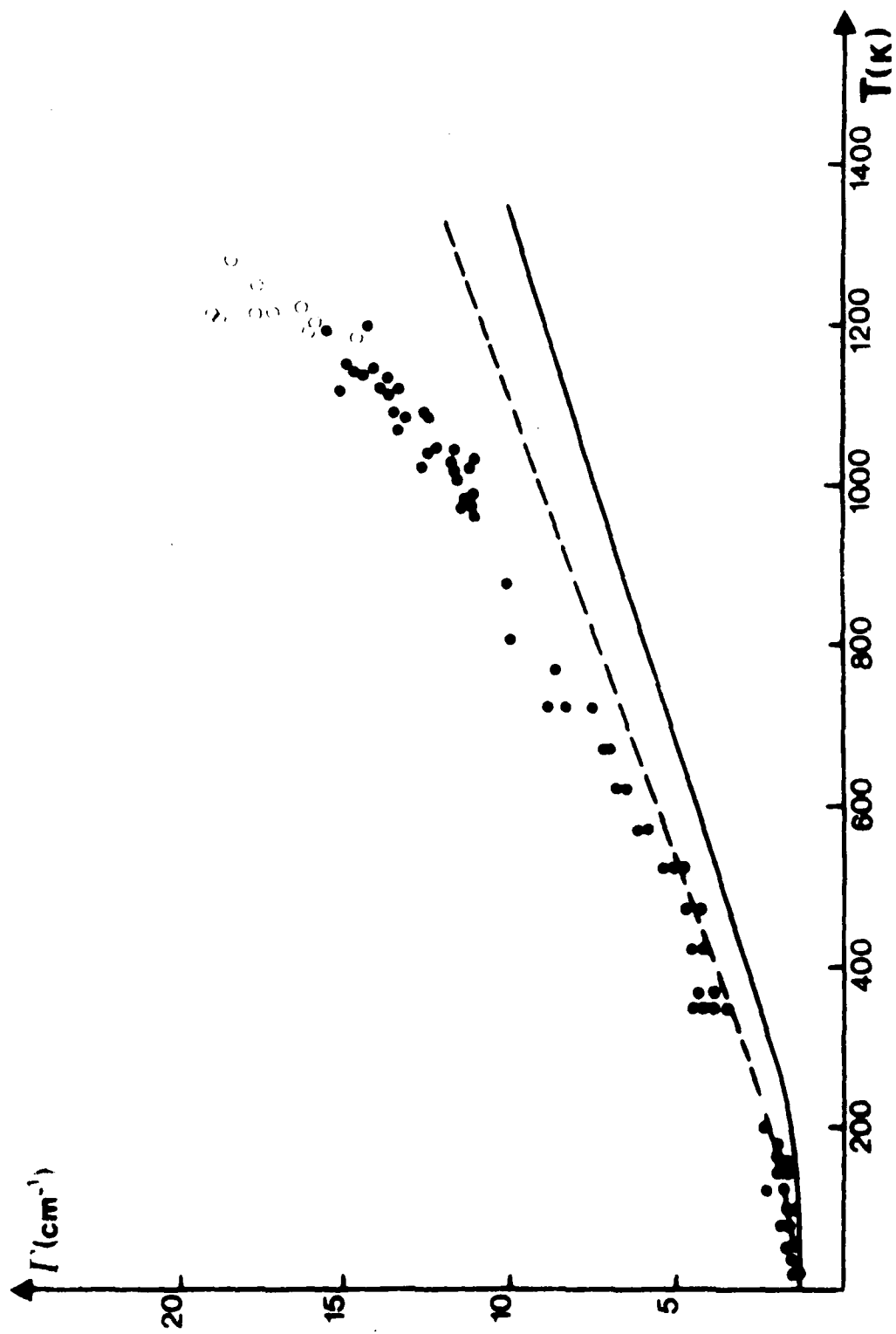


Figure 8 : Variation of the width of the zone center phonon of Silicon versus temperature.

processes to the frequency shift. The agreement between the experimental points and the solid curve is seen to be good.

If we try to fit the experimental data with three-phonon processes only by omitting the term in Eq.(3.10) with the factor  $D$ , we obtain the dashed curve in Figure 9 with  $\omega_0 = 529 \text{ cm}^{-1}$  and  $C = 4.24 \text{ cm}^{-1}$ . Although this curve fits the data well at temperatures up to 600K, it is clearly inadequate at higher temperatures. This demonstrates the necessity of including terms corresponding to four-phonon processes in the expression for  $\Delta(T)$ .

In principle, the four-phonon contributions in Equations (5) and (7) should include terms arising from difference processes. We have omitted such terms on the grounds that their inclusion would simply introduce additional terms varying as  $T$  and as  $T^2$  in the high-temperature limit and would not add any new qualitative features.

The temperature determined by measuring the width and the frequency shift of the Raman peak and using the formulas with the fitted parameter can give a good correlation with the temperature measured by using the Stokes to anti-Stokes ratio.

As an example of using these methods, we give now a determination of the temperature reached at the spot of an Argon laser focussed onto thin layers of Silicon deposited on Silicon substrates and on Silica substrates.

#### 4.3. Temperature of a thin layer of Silicon under continuous laser irradiation.

Thin layers of Silicon have been deposited by C.V.D. technique (Chemical Vapour Deposition) at a temperature of  $700^\circ\text{C}$ . The layer of Silicon is then a polycrystalline material. Two kind of substrate have been used : Silica and monocrystalline Silicon. The difference of thermal conductivity of these two materials gives rise to a different behaviour under laser irradiation. The laser used to irradiate the samples is a continuous Argon laser. The power density of the irradiation has been varied between 0 and  $10\text{kW}/\text{cm}^2$ .

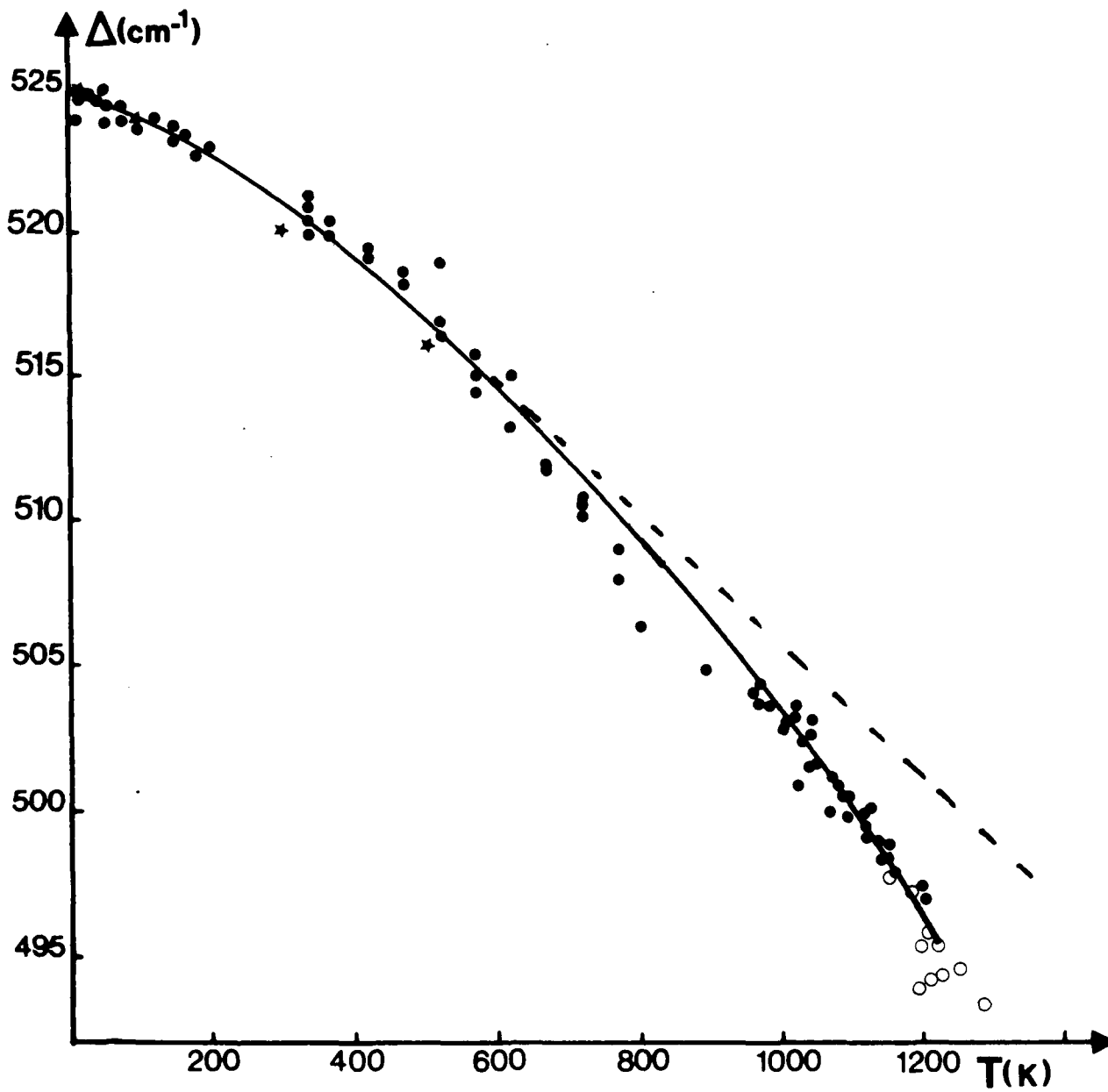


Figure 9 : Variation of the shift of the zone center phonon of Silicon versus temperature.

#### 4.3.1. Fused Silica substrate.

The Raman spectra for this layer versus the irradiation power are presented on Figure 10. The spectra shows a dissymetry towards the low frequencies region which is due to the presence of strains inside the thin layer. This fact prevents the use of the frequency shift and the width of the Raman peak. These strains are due to the difference between the dilatation coefficients of Silica and Silicon and this problem could be neglected in the case of an homogeneous sample.

The temperature of the layer has thus just be determined using the curve of the Figure 7.

#### 4.3.2. Silicon substrate.

The Raman spectra of a deposited layer of Silica on Silicon are presented on Figure 11. In this case, the thermal conductivity is so high that the temperature elevation is very small. The Figure 12 shows the temperature for both substrates versus the power irradiation. As can be seen, the temperature exceeds  $1000^{\circ}\text{C}$  for the Silica substrate whereas the temperature does not reach  $100^{\circ}\text{C}$  under the same conditions for the Silicon substrate.

### 5. RAMAN SPECTROSCOPY OF VERY HEAVILY DOPED SILICON.

Ionic implantation followed by laser annealing can produce new samples doped with a concentration of impurities which can exceed the solubility limit. This new material could present a technological interest in the field of solar cells or I.I.L. logic devices.

The Raman spectroscopy can characterize the doping effect by controlling two different characteristic of the spectra. The first one is the occurrence of new peaks in the spectra ; these peaks are related to the position of the implanted impurity. The second one is the interaction between free carriers and normal or impurity modes. This effect is responsible of a deformation of the line shapes of these modes.

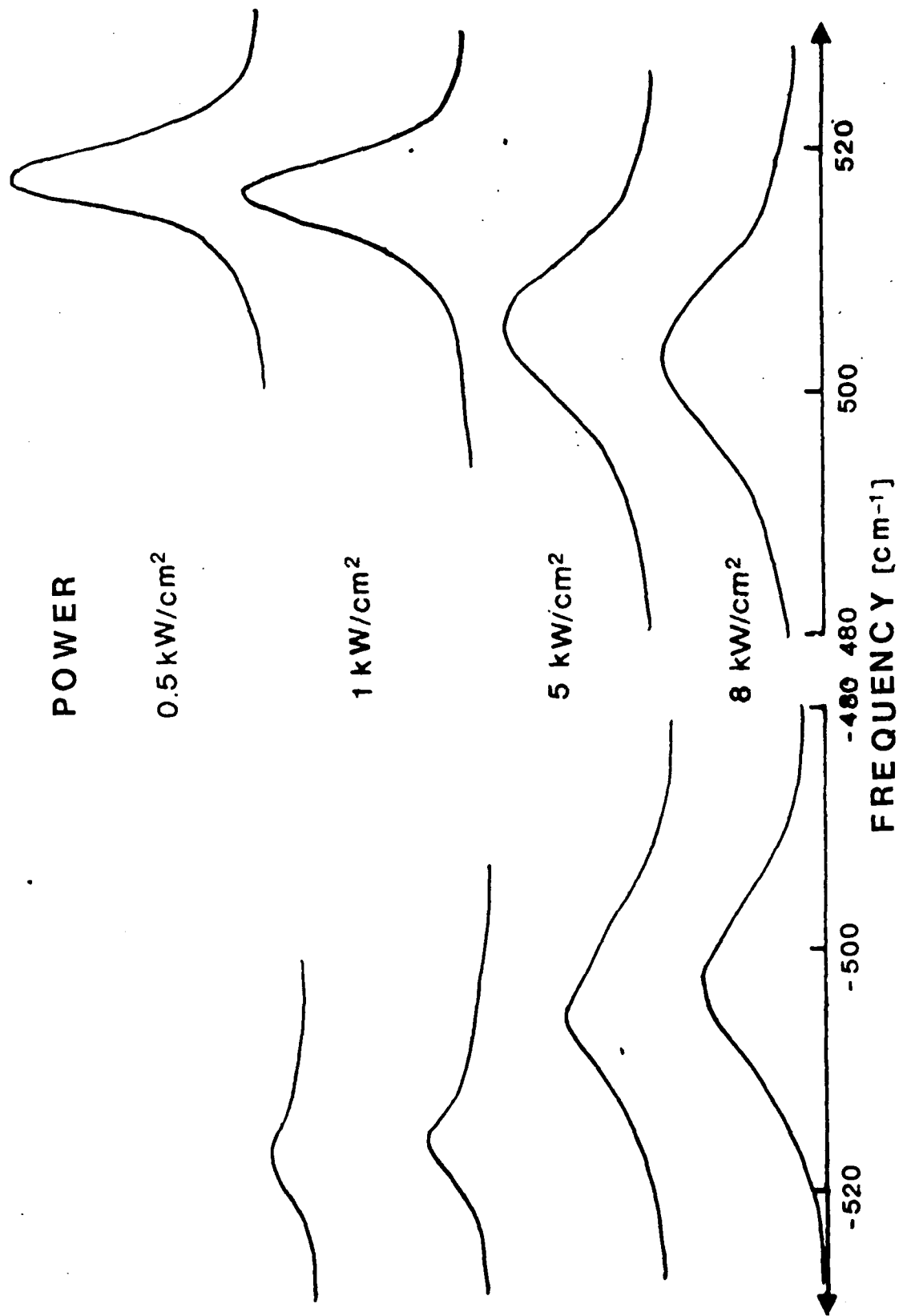


Figure 10 : Raman spectra of a polycrystalline layer of Silicon deposited on Silica versus irradiation energy.

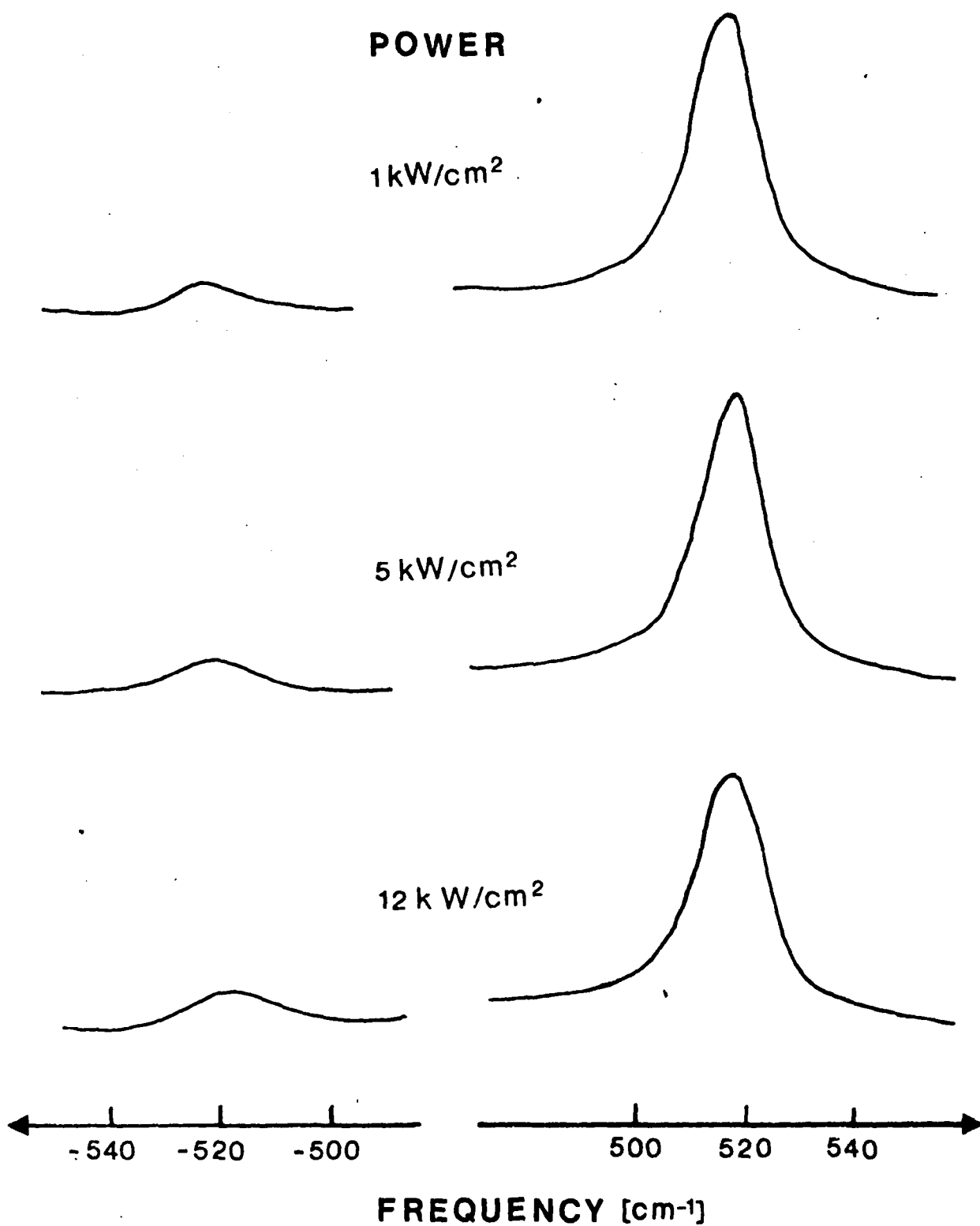


Figure 11 : Raman spectra of a polycrystalline layer of Silicon deposited on Silicon versus irradiation energy.

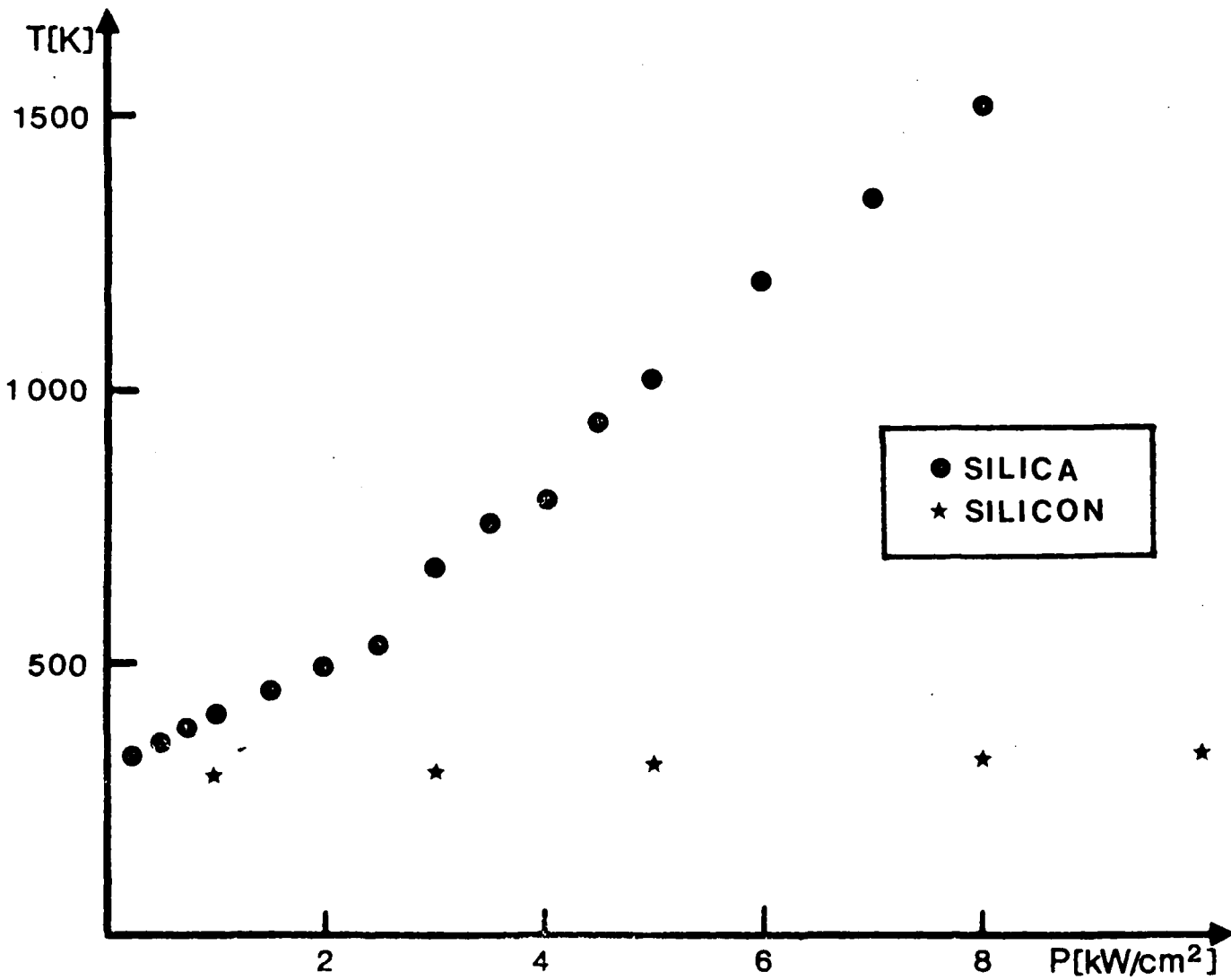


Figure 12 : Temperature of Silicon layers for both substrates versus irradiation energy.

### 5.1. The vibrational modes introduced by the defects.

When defects are introduced in a perfect crystalline lattice, the translation symmetry is suppressed and the vibrational properties of the crystal are modified. The calculation of the new frequencies is rather difficult. The simplest method to achieve it is the use of the Green functions first introduced by Lifshitz<sup>(17)</sup> and then used by Dawber and Elliott<sup>(18)</sup> in a model describing the vibrations of a unique substitutional impurity in the Silicon.

Depending upon the mass of the impurity two kind of vibrations are distinguishable. When this mass is higher than that of the matrix, the vibrations are of the "band mode" sort. These vibrations can propagate along the lattice. When the mass of the impurity is lower than that of the matrix, the vibrations are of the "localized mode" sort which are located in the neighbourhood of the impurity. The Raman spectroscopy is usually more sensitive to localized modes than to band modes. In the Silicon, the only light impurity with a high solubility is the Boron so this impurity has been widely investigated by optical spectroscopy. The localized mode induced by this atoms in substitutional positions have been observed some times ago in diffused or implanted materials by infrared spectrometry<sup>(19)</sup> or Raman spectroscopy<sup>(20,21)</sup>.

### 5.2. Free carriers-phonons interaction in heavily doped Silicon.

The simultaneous presence of two kind of excitations a discrete one and a continuous one gives rise in the Raman spectrum of Silicon to specific effect<sup>(22,23)</sup>. The discrete excitation corresponds to the phonon and the continuous one to the free carriers. Both excitations are Raman active, the phonon giving a sharp peak contribution to the spectrum, the free carriers giving a very broad continuum. The coupling between these two excitations modifies the Raman spectrum in such a way that what is observed is not only a simple superposition of the sharp peak upon a broad continuum but an interference which modify the shape of the phonon line (Fano effect). This shape which is Lorentzian in Lorentzian in absence of free carriers ( $I(\omega) = \frac{I_0}{\Gamma^2 + (\omega - \omega_0)^2}$ ) becomes asymmetric in presence of electronic following the equation :

$$I(\omega) = \frac{I_0(q+\epsilon)^2}{\Gamma^2 + (\omega - \omega_0)^2} \quad \text{where } q \text{ is proportional to the ratio of the}$$

tensors for purely lattice and purely electronic Raman scattering.  $\epsilon = \frac{\omega - \Omega}{\Gamma}$  where  $\Omega$  is the "dressed" phonon frequency and  $\Gamma$  the phonon damping in presence of free carriers but without interference. The sign of the factor  $q$  governs the sense of the asymmetry observed on the spectrum. This sign is itself depending upon the type of the free carriers (electrons or holes). The doping with P type impurities (Boron, ...) induces an asymmetry towards the high frequency whereas doping with n type impurities gives rise to asymmetry towards the low frequency region.

### 5.3. Experimental results.

#### 5.3.1. Laser annealing of p-doped Silicon.

The sample used for this study is a Silicon (111) implanted with Boron ( $10^{16}$  ions/cm<sup>2</sup>, 70 kV). Boron being a light ion, the material is not continuously amorphized. After implantation, the Raman spectrum of the sample is still a crystalline one. When compared to the Raman spectrum of the sample before implantation, only a decreasing in intensity and a small asymmetry towards low frequency are noticeable (Fig.13). This asymmetry is due to strains induced by the implantation process and to small clusters of amorphous material. A very small peak appears at  $618 \text{ cm}^{-1}$  which is the frequency of the localized mode due to B<sub>11</sub> isotope in substitutional position. After irradiation with a YAG laser ( $0.6 \text{ J/cm}^2$  at  $1.06 \mu\text{m}$  +  $0,2 \text{ J/cm}^2$  at  $0,53 \mu\text{m}$ ), the center of zone mode presents a strong asymmetry towards the high frequencies and a rather high intensity mode appears at  $618 \text{ cm}^{-1}$ . This peak too, presents an asymmetry towards the high frequencies. The appearance of the  $618 \text{ cm}^{-1}$  peak is a proof of the high concentration of substitutional Boron. The asymmetry of both peaks (normal mode and localized mode) is the indication of a high free carrier concentration. The comparison of laser annealing and thermal annealing is done on Figure 14. The thermal annealing was achieved in an oven at a temperature of  $1000^\circ\text{C}$  during 2 hours. As can be seen, the Raman spectra are more or less similar, the intensity of the Boron local mode being a little more intense in the case of the laser annealing.

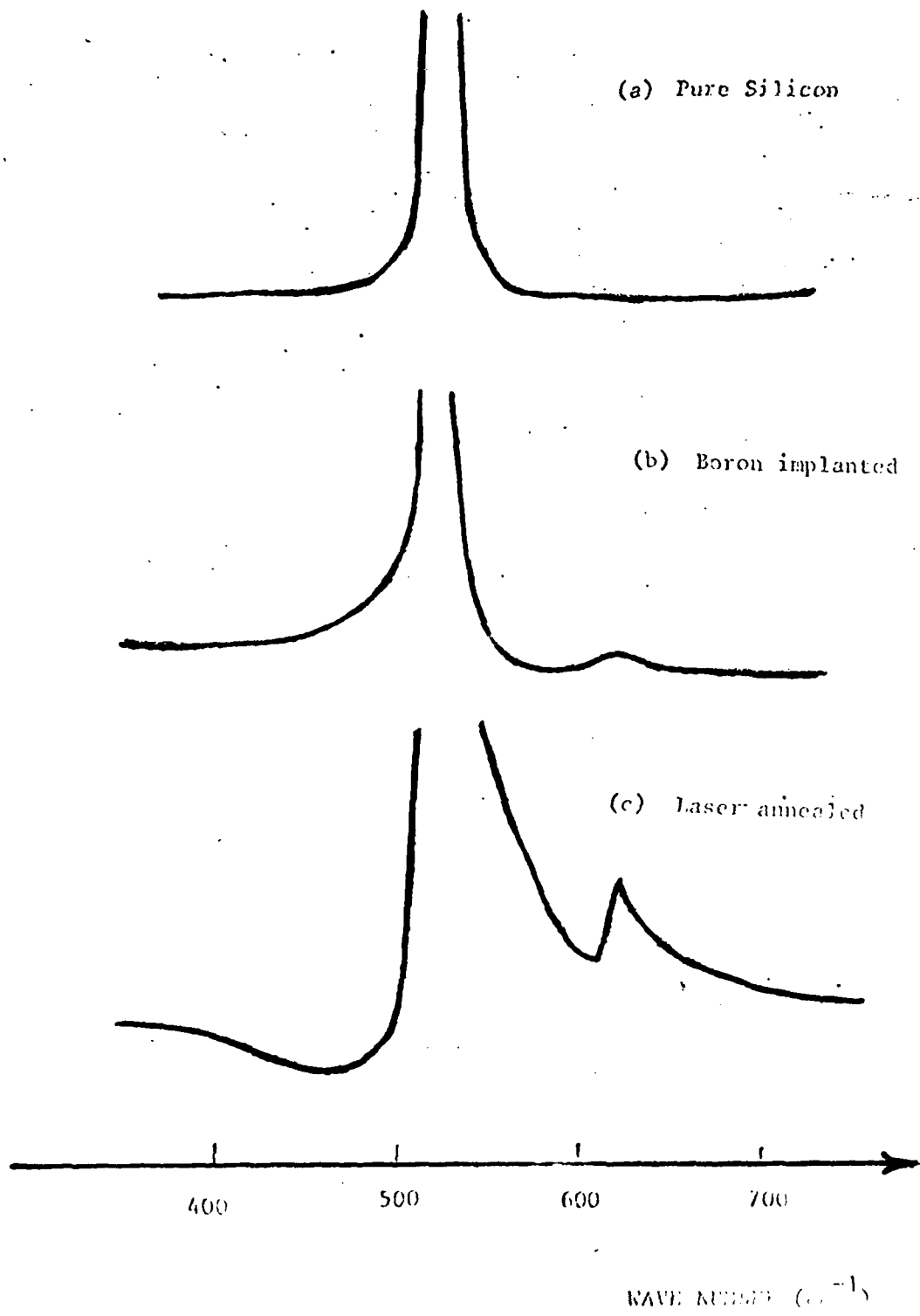


Figure 13 : Raman spectra of pure Silicon (a) ; Silicon implanted with  $10^{16}$  B/cm<sup>2</sup> (b) ; Silicon implanted and laser annealed.

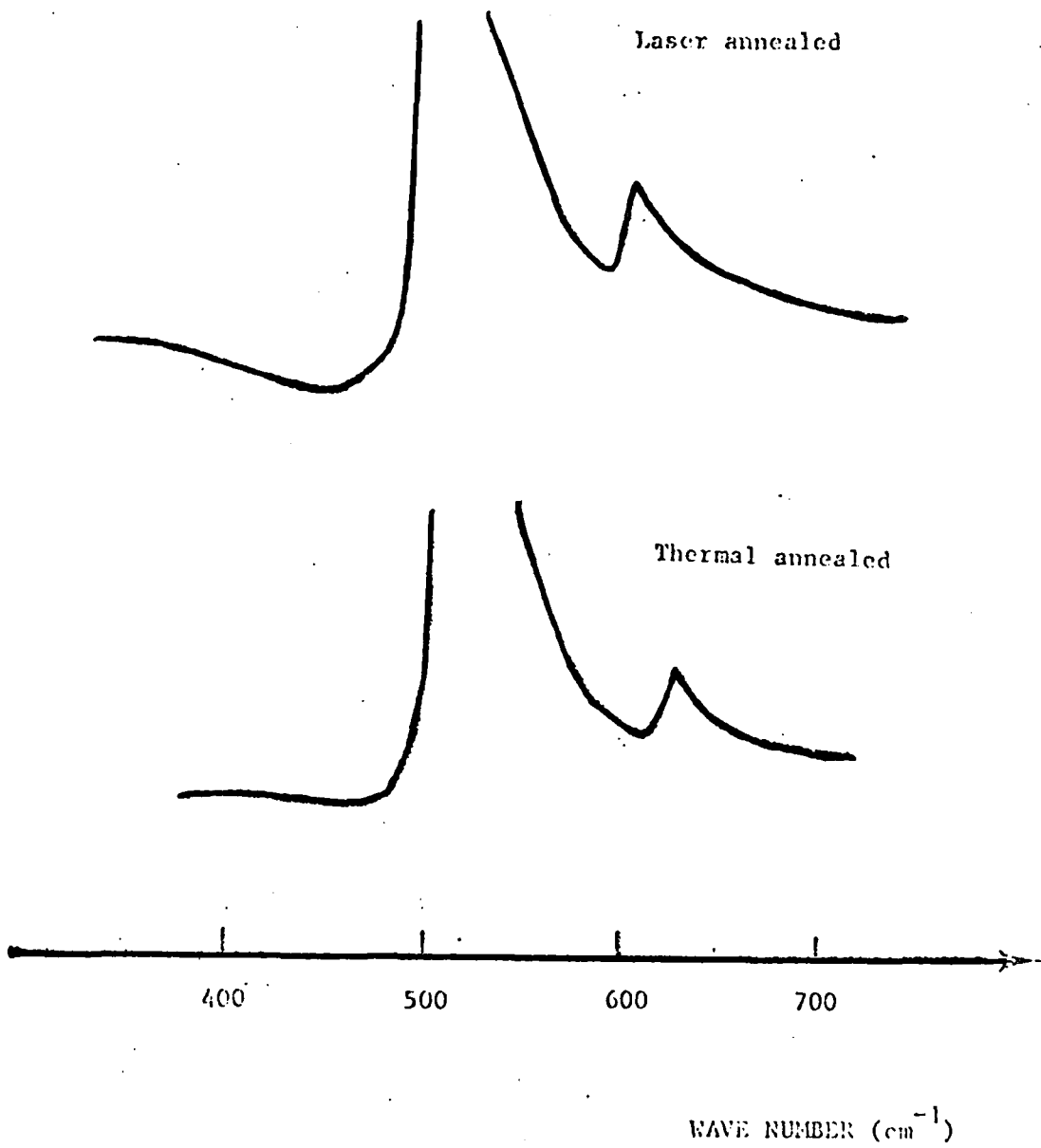


Figure 14 : Comparison of Raman spectra of Boron implanted Silicon laser annealed and thermal annealed.

### 5.3.2. Laser annealing of compensated Silicon.

Phosphorus ions in substitutional site do not give rise to local mode because of their mass which is of the order of the Silicon mass. These ions should give a band mode but these band modes are usually difficult to observe by Raman spectroscopy. However, when a Silicon sample is doped with Boron plus Phosphorus, the Phosphorus atoms can modify the local modes due to Boron atoms. As a matter of fact, the local mode of isolated Boron in substitutional positions is triply degenerated. If a Phosphorus atom is situated in the neighbourhood of the Boron atom, the symmetry is modified and the triply degenerated mode at  $618 \text{ cm}^{-1}$  is split into two modes at  $628 \text{ cm}^{-1}$  and  $600 \text{ cm}^{-1}$  (24). The Figure 15 presents the Raman spectra of Silicon implanted with  $2 \cdot 10^{16}$  Boron per  $\text{cm}^2$  under 50 kV and  $2 \cdot 10^{16}$  Phosphorus per  $\text{cm}^2$ . The implantation energies have been chosen in order to approximately balance the penetration depths of both impurities. After implantation a spectrum characteristic of amorphous material is observed. After laser annealing ( $0,6 \text{ J/cm}^2$  at  $1,06 \text{ m}$  +  $0,2 \text{ J/cm}^2$  at  $0,53 \text{ m}$ ), the Raman mode of the zone center is dissymmetric towards the lower frequencies region, proof of a surcompensation of free carriers as compared to the sample implanted with Boron only. The concentration in electrons is thus superior to that of holes on the region sampled by the Raman laser beam. The local mode does not see its frequency modified. The intensity of this mode is higher than for a sample implanted with Boron only because of the reduction of the interference due to the partial compensation of free carriers. The fact that the frequency of this mode has not moved, seems to prove that there are very few Boron and Phosphorus atoms on nearest neighbours sites. On the contrary, in the case of the thermal annealing of the same sample ( $1000^\circ\text{C}$  - 2 hours), the local mode has moved to  $626 \text{ cm}^{-1}$  which is a frequency characteristic of a pair mode B-P. The other peak of a pair mode situated around  $600 \text{ cm}^{-1}$  is not observed. The normal mode is slightly asymmetric towards the lower frequencies. The sample is thus rather well compensated with just a weak over concentration of electrons on the path of the Raman laser beam.

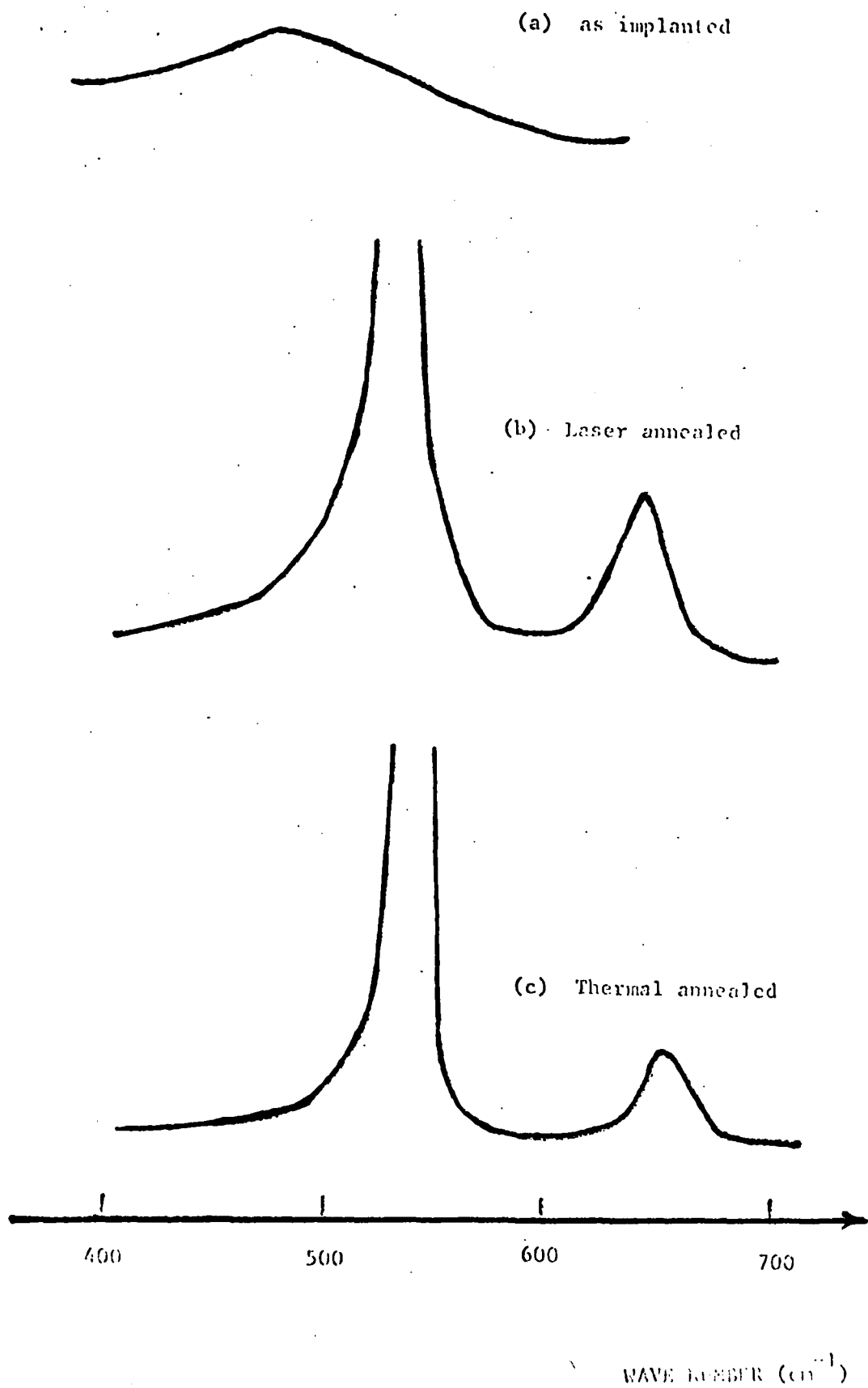


Figure 15 : Raman spectra of Boron and Phosphorus implanted Silicon ;  
as implanted (a) ; laser annealed (b)

Laser annealing and Thermal annealing have thus different effects on Boron + Phosphorus implanted Silicon. In the case of thermal annealing, atoms of Boron and Phosphorus have enough time to pair on neighbours lattice sites whereas in the case of Laser annealing this is not possible.

### 5.3.3. Laser annealing of n-doped Silicon.

The samples used were cut along a (100) face and implanted with Arsenic dose varying from  $5.10^{15} \text{ cm}^{-2}$  to  $5.10^{16} \text{ cm}^{-2}$ . After implantation, the samples were subjected to the irradiation beam of a Q switched YAG laser equiped with a frequency doubler. The duration of the pulses was typically 100ns and energy density up to  $2.5\text{J}/\text{cm}^2$ . The processing of the samples was done at the "Groupe PHASE" at the C.R.N. (Strasbourg).

After implantations, the amorphous character of each sample has been verified by detecting the classical "density of states" Raman spectrum of Silicon. This typical broad band situated at  $480 \text{ cm}^{-1}$  is due to the scattering of the light induced by all the phonons in the Brillouin zone in contrary to the sharp peak at  $520.5 \text{ cm}^{-1}$  observed on crystalline Silicon for which only the mode of the center of the zone is active. For the samples implanted in the range  $5.10^{15}$  to  $3.10^{16} \text{ As}/\text{cm}^2$ , the large amorphous band is well observed and no thin crystalline peak can be observed in addition to this band. This signifies that these samples are amorphous on a thickness larger than the penetration depth of the laser. For the last sample, a thin crystalline peak at  $520.5 \text{ cm}^{-1}$  is detected, superposed to the broad amorphous band. This peak could be due to a part of the sample which has been partially recrystallized during the implantation process itself. The high dose of Arsenic implanted ( $5.10^{16}/\text{cm}^2$ ) imposed a very high beam current in order to keep reasonable the time of processing. This high flux induces then an elevation of the temperature of the sample sufficient to recrystallize a thin thickness of the just amorphized layer (Ion beam annealing).

After laser annealing, the disappearance of the broad amorphous band confirms the recrystallization of each sample. Two features of interest are visible on the spectra presented on Figure 16. A peak at  $520.5 \text{ cm}^{-1}$  is due to the light scattered by the substrate

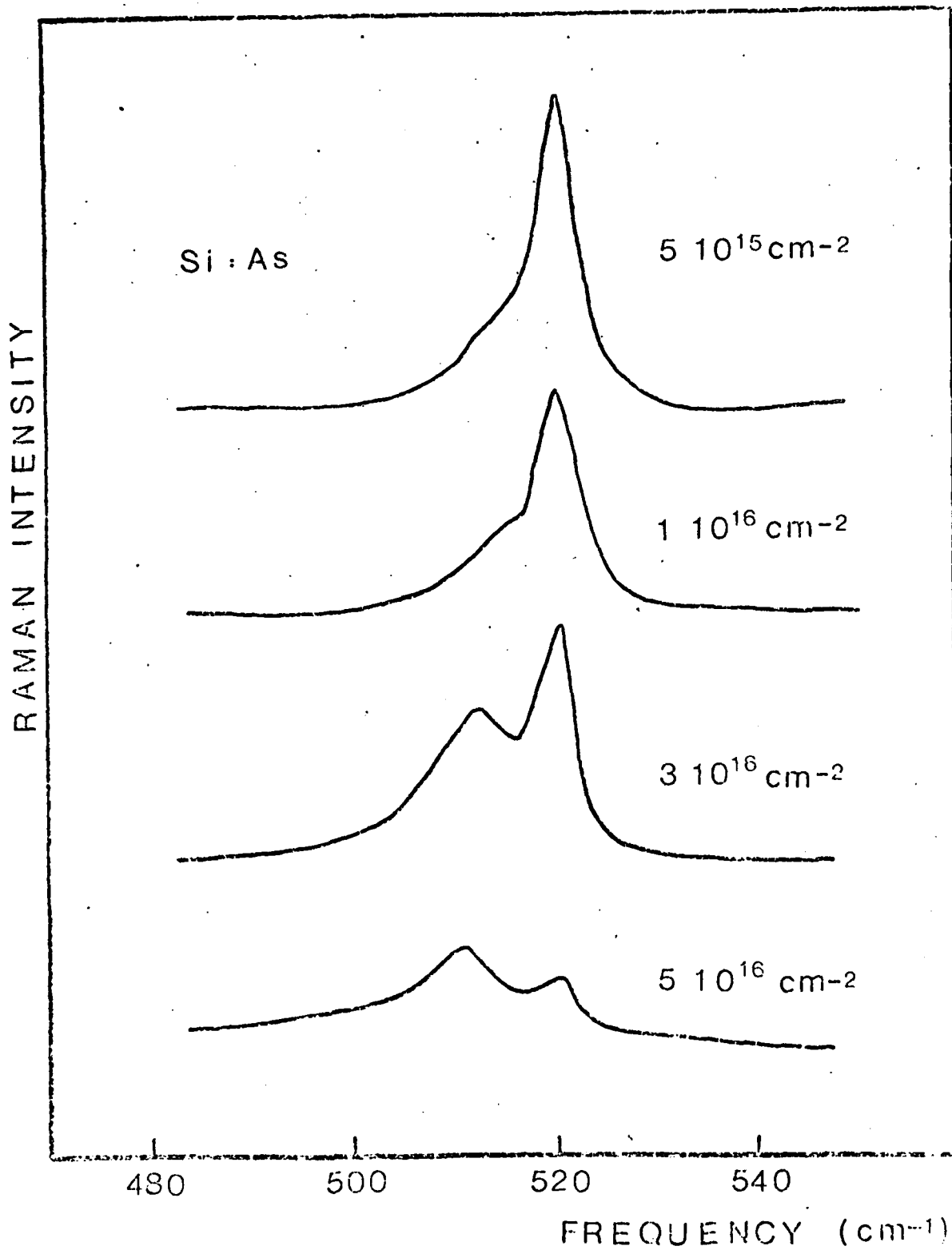


Figure 16 : Raman spectra of asler annealed Arsenic implanted Silicon for various implantation doses.

through the perturbed layer. Besides this line and shifted towards the lower frequency region, a broader and slightly asymmetric peaks can be observed. The frequency of this peak varies from  $515.5 \text{ cm}^{-1}$  to  $511.5 \text{ cm}^{-1}$  as the implantation dose increases from  $5 \cdot 10^{15}$  to  $5 \cdot 10^{16} \text{ As/cm}^2$ .

Two processes can explain the presence of this shifted peaks in the spectra. First, a size effect could be induced by the presence of microcrystallites in the annealed area<sup>(1)</sup>. This effect can be ruled out, considering the good monocrystalline quality of the samples, determined by Rutherford backscattering measurements. This other effect is the coupling of the continuum of electronic transitions with the discrete phonon state (Fano effect) discussed in paragraph 5.2. This effect is usually weak in N type semiconductors but the special processing of these samples (implantations and laser annealing) can lead to a free carriers concentration far above the saturation and thus to a very large Fano effect.

On Figure 17 are presented the spectra of an  $1.5 \cdot 10^{16} \text{ As/cm}^2$  implanted sample laser annealed before and after a thermal annealing ( $600^\circ\text{C} - 1 \text{ jour}$ ). The shift peak has disappeared after the thermal processing. This thermal processing has released the out of equilibrium heavily doped state of the sample thus leading to the disappearance of shifted peak of the Raman spectrum.

From the value of the frequency shift, it is possible to calculate the free carriers concentration. The table summarizes the results obtained for 4 samples and compared to the values of concentration measured by resistivity at Strasbourg.

TABLE

	$0.5 \cdot 10^{16} \text{ cm}^{-2}$	$1 \cdot 10^{16} \text{ cm}^{-2}$	$3 \cdot 10^{16} \text{ cm}^{-2}$	$5 \cdot 10^{16} \text{ cm}^{-2}$
Raman shift ( $\text{cm}^{-1}$ )	5	5.5	8	9
Raman concentration ( $\text{cm}^{-3}$ )	$1.6 \cdot 10^{21}$	$2 \cdot 10^{21}$	$5.5 \cdot 10^{21}$	$7.5 \cdot 10^{21}$
Resistivity concentration ( $\text{cm}^{-3}$ )	$0.37 \cdot 10^{21}$	$0.52 \cdot 10^{21}$	$1.2 \cdot 10^{21}$	$2.25 \cdot 10^{21}$

RAMAN INTENSITY

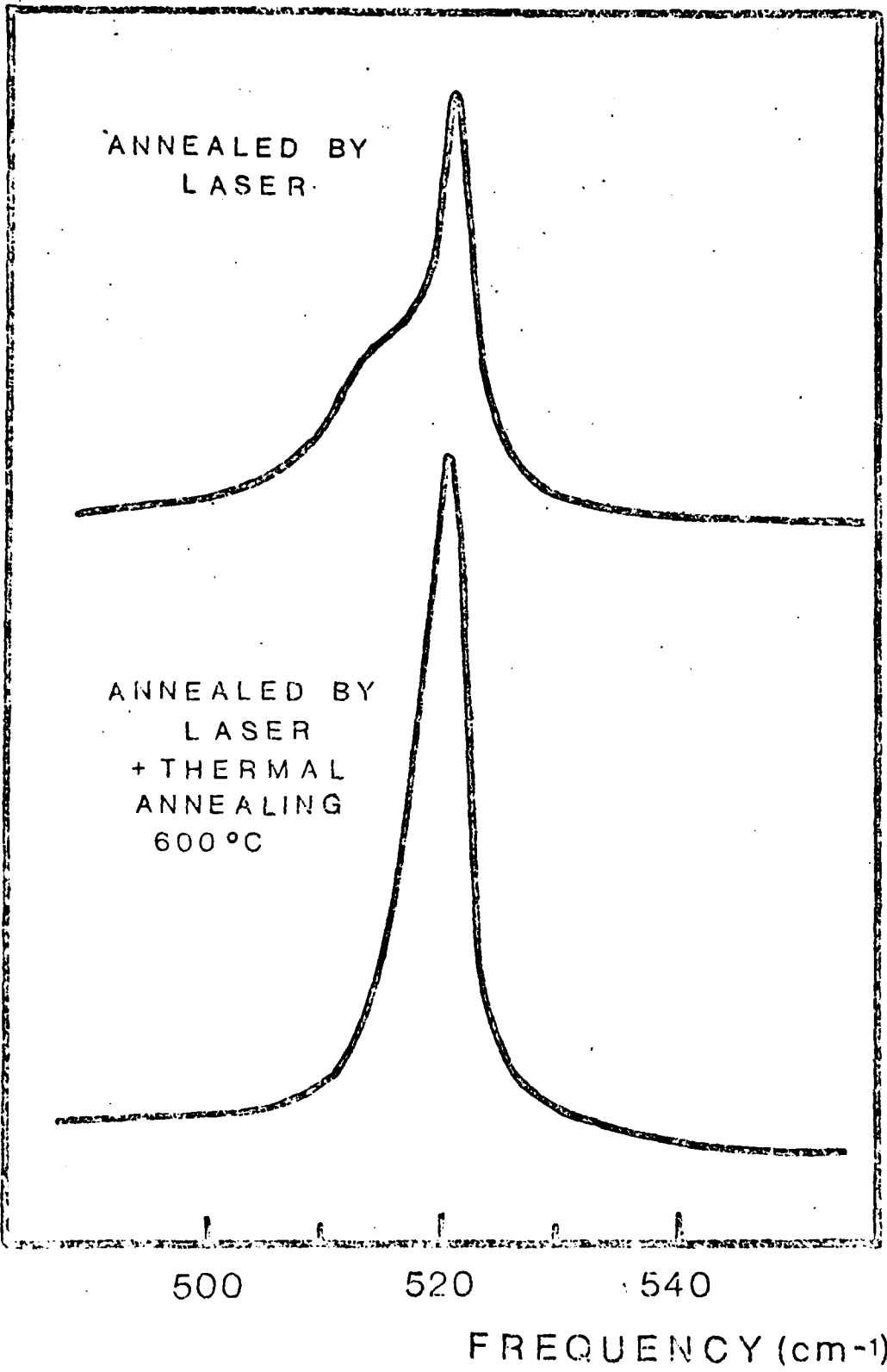


Figure 17 : Influence of thermal treatment on Raman spectra.

As it can be seen, the concentration measured by the mean of Raman scattering gives higher values than the concentration obtained by electrical measurements. This discrepancy can perhaps be explained by the hypothesis made to compute the concentration from the Raman shift. The model used to achieve this computation suppose the parabolicity of the band structure<sup>(25)</sup>. For very heavily doped Silicon, the Fermi level reaches regions where this parabolic approximation is no longer valid. The flattening of the bands increases the effective masse of electrons which in turn increases the joint density of states. A complete calculation using the real shape of the band structure would lowers the free carriers concentration and thus gives a closer agreement with the values obtained by electrical measurements.

## 6. SUB-PICOSECOND SPECTROSCOPY.

The experiments presented in the previous chapter were made after laser annealing. This kind of experiments can characterize the samples and are thus of interest for devices development. However, it is not possible to get information on the process of laser annealing itself from such studies. In order to understand the laser annealing process, time resolved spectroscopy is required. Since the real problem is the understanding of the relaxation processes during the first hundredths of femtoseconds, the laboratory has now built a sub-picosecond laser source.

### 6.1. The sub-picosecond optical source.

The oscillator part of this source is of the "colliding pulse modelocked" (CPM) type described by C.V. SHANK<sup>(26)</sup>. A Rodhamine 6G dye laser is continuously pumped by a C.W. Argon laser in a ring geometry cavity. In the path of the cavity, a thin jet of saturable absorbant (DODCI) allows the synchronization and the shortening of the pulses (Fig.18). This geometry automatically involves that the two pulses travelling in both directions in the cavity, collide on the absorber where the sum of their intensity is sufficient to reach the threshold of transmission. Pulse widths of 90 fs ( $10^{-15}$ s) are easily achieved in those conditions with this Colliding Pulse Mode - locking (C.P.M.) oscillator.

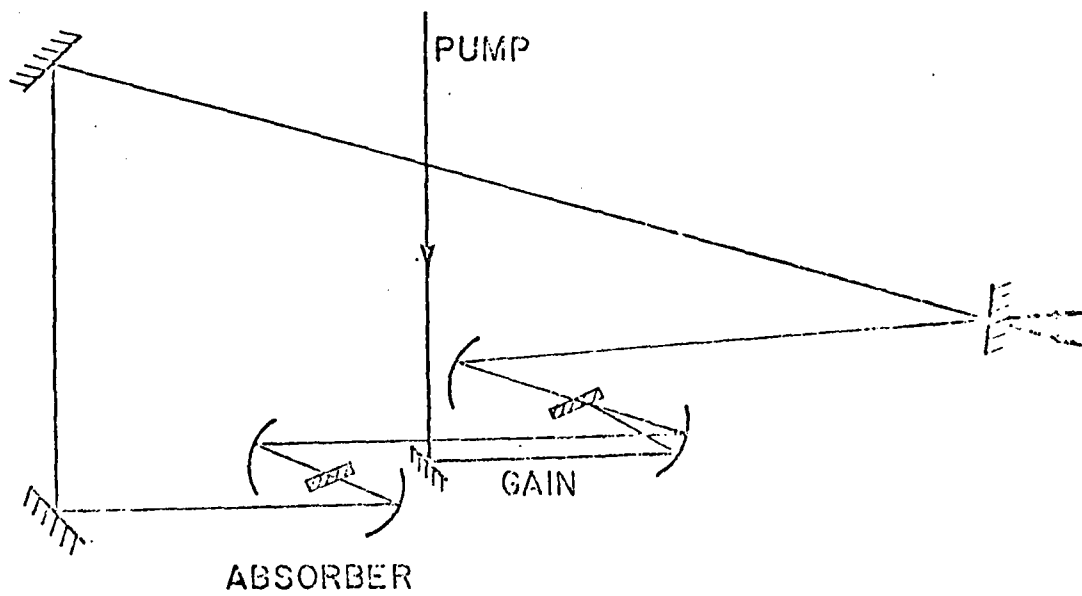


Figure 18 : Schematic diagram of a CPM oscillator.

This oscillator is now working and is extensively tested in order to characterize the mean power, peak power and duration of the pulses.

The second part of the experimental set up is the amplifier. The construction of this part is now in progress. This is a four stages amplifier, each stage being separated from the others by absorber jets to provide isolation. The 3 first gain cells are pumped transversally by a YAG laser. The last stage is pumped longitudinally by the same laser. At the output, the pulse is recompressed by a Treacy compressor which comprises two gratings in a subtractive mounting. The gain in peak power should be of the order of  $10^6$ .

#### 6.2. Characterization of the source oscillator.

Three diagnostic tools are used to characterize the pulses. The first one is an avalanche photodiode followed by a sampling oscilloscope. This measure can only ensure that the laser is pulsing as the intrinsic pulse duration is much smaller than the response of the apparatus. The period of recurrence can be measured and is equal to 14ns which is the time of flight of the pulses in the cavity.

The spectrum of the pulse is qualitatively checked by sending a small part of the light diffracted by a grating onto a screen. The length of the trace on the screen is, the shorter is the pulse as time and frequency are related through a Fourier transformation.

The third measure allows an indirect determination of the pulse duration by means of an autocorrelator. This autocorrelator is made up of a folded Michelson interferometer where the pulse is divided into two parts on a semitransparent layer. One of the two pulses is delayed through a vibrating prism. The two pulses are then recombined on a doubler crystal of KDP. At the output of the crystal a beam of ultra-violet light is created when the two pulses are overlapping. This light is detected by a photomultiplier and the signal is sent on the vertical channel of an oscilloscope. A voltage synchronized with the vibration movement of the prism is sent on the horizontal channel of the oscilloscope. The net result

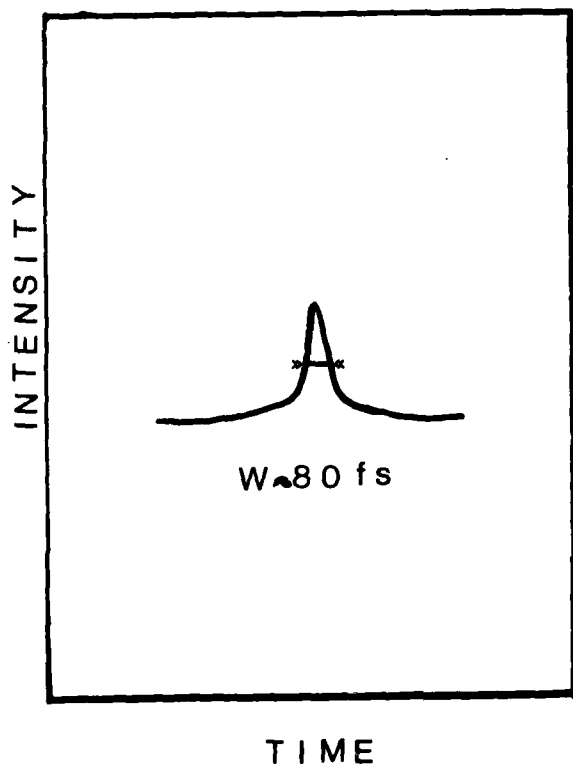
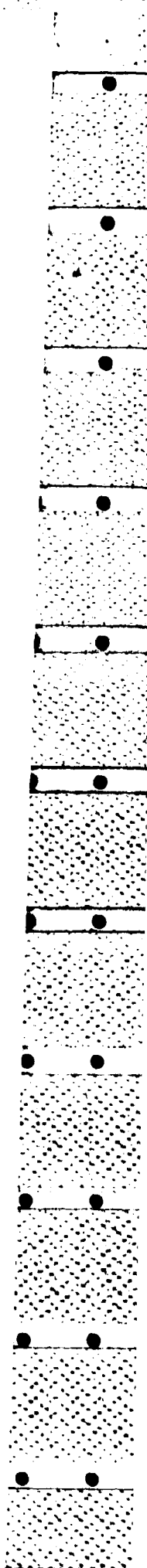


Figure 19 : Auto-correlation trace of the CPM oscillator.



is the autocorrelation trace of the pulse on the screen of the scope. The measure of very short time is thus transformed in the measure of the elongation length of the prism movement. The Figure 19 shows an autocorrelation trace of the oscillator. The width at half height is about 80fs (femtosecond).

The mean power of the source is easily measured with a power-meter of the calorimeter type. It has been determined to be 6mW for a power of the Argon pump laser of 4W.

Knowing the recurrence period, the mean power and the pulse duration, it is possible to determine a peak power of 100kW.

## 7. DISCUSSION AND CONCLUSIONS.

Laser annealing has now a long history and an abundant literature. The interesting question, which still remains to be answered, is what are the elementary processes in the interaction of a strong radiation field with matter.

The process of laser annealing consists of two sets of phenomena. The first concerns the effect of a dense radiation field on matter creating elementary excitation far from equilibrium. The initial hot plasma redistributes through interactions between carriers and ultimately thermalizes giving up energy to heavier particles which are the lattice constituents. The second set of phenomena, of a completely different nature, concerns the modifications induced to the solid as a result of the creation of the dense hot plasma. If the laser pulse is short enough, the e-h density reached corresponds to an amount of broken covalent bonds which is a significant portion of the total number of bonds, the crystal becomes fluid even at  $T = 0$  K. Ultimately, the solid sets in a new phase whose structure depends on the elementary mechanisms of interaction and organization of the lattice constituents. We shall discuss successively these two states as : i) direct laser effect and ii) consequences of the laser action.

### 7.1. Direct laser effect.

The incident laser energy is absorbed by electron-hole pairs creation and by free carrier excitation. In indirect gap semiconductors, electron-hole pairs are created via indirect absorption processes involving the emission and absorption of phonons. Because phonon energies are much smaller than photon energy, the amount of energy transferred to the lattice during absorption is negligible in comparison to the total amount absorbed. The rise of carrier density leads, in turn, to increased free carrier absorption. The net result is the production of hot-electrons and holes far from equilibrium which subsequently thermalize with the set of the carriers and eventually with the lattice. The observations by Shank et al<sup>(27)</sup> demonstrate that with short, 90 femtoseconds optical pulse, an unstable form of highly excited state is created near the surface which persists for a fraction of picosecond.

For very short impulsion of radiation, from the experiments<sup>(21-27)</sup> one perceives clear indications that there are two steps of the laser action on a crystal well separated in time. In the first step, the electromagnetic energy transferred from the laser beam to the solid is retained in the highly excited non-equilibrium electronic state. In a second step, this energy is transferred to the lattice.

Recently, a theoretical model<sup>(28)</sup> is proposed which takes into account the space time evolution of the plasma during the pulse in order to explain the processes in densities higher than  $10^{22} \text{ cm}^{-3}$  reached in 100fs pulses. The novelty in this model is the argument that free carrier absorption is dominated by e-h collisions with a characteristic relaxation time  $\tau = 3 \cdot 10^{-16} \text{ s}$ .

A different situation is reached with much longer pulses :  $\tau_L = 10 \text{ ns}$  and a photon absorption rate  $g \sim 10^{31} \text{ cm}^{-3} \text{ s}^{-1}$  : Auger recombination becomes the dominant recombination mechanism at these densities.

Most of the laser energy is absorbed by the carriers within the absorption depth. Eventually, these carriers loose their energy to the lattice, the rise of the lattice temperature then depends

on the distance they have diffused before substantial phonon emission occurs. At moderate density, the phonon scattering time is  $\tau \sim 10^{-13}$  s. Screening does not affect the rate of intervalley phonon emission until  $N_e \sim 10^{21}$  cm<sup>-3</sup>. Because screening increases the electron-phonon scattering time, it not only decreases the rate of phonon emission but also enhances diffusion. This increases the volume of the region in which the energy of the excited carriers is transferred to the lattice. Owing to the extreme non linearity of the hot carrier effects, it is impossible to make an accurate estimate of the precise temperature to which the lattice is heated or to determine the laser power threshold above which melting will occur.

#### 7.2. Consequences of the laser action.

The equilibrium observations are clear : an amorphous or glass solid is transformed into crystal under laser action and a crystal submitted to very short laser irradiation is transformed into amorphous material. An implication of both of these transformations is that melting precedes the transition. Another alternative is that the phase transition is directly induced in the highly excited state.

The effect of a dense plasma on the melting temperature is itself an interesting problem of solid state theory. This question has been recently addressed by Bok and Combescot<sup>(30)</sup>. It is shown that in the presence of a dense plasma, the melting temperature of a solid changes. The melting temperature decreases with increasing plasma density. For a laser pulse of 1J/cm<sup>2</sup> during 10ns, it is considered that e-h plasma reaches a steady state in a time shorter than the laser pulse. Considering the plasma expansion due to its high pressure, its collision with phonons and Auger recombination, the highest plasma density is of the order 10<sup>21</sup> cm<sup>-3</sup>. This density is nevertheless considered to be sufficient to considerably reduce the melting temperature so that a metallic layer of liquid Silicon is formed at the surface.

The role of a high plasma density in laser annealing has been discussed by Van Vechten et al<sup>(5)</sup> in a quite different way but still involving electron-phonon coupling and lattice instability induced by this interaction. Above a critical carrier density estimated at  $8 \cdot 10^{21} \text{ cm}^{-3}$ , a second order phase transition occurs. At this plasma density, the bond charges will be so depleted that they will no longer be able to stabilize the TA phonon modes<sup>(25)</sup>. The crystal will no longer resist shearing stresses and will become fluid. This fluid is distinct from the normal molten phase of Si the latter being the result of a strictly first order phase transition driven by the atomic motion at high temperatures. The assumption of Van Vechten is that the plasma is supposed to directly induce the structural transformation. The energy is retained in the electronic system instead of being entirely associated with the atomic motion. As the plasma becomes less dense due to expansion and to transfer of energy to the lattice, the material will pass back through the second order phase transition at  $8 \cdot 10^{21} \text{ cm}^{-3}$  and covalent bonding will gradually appear. The material will finally recrystallize if this process is relatively slow or will solidify in the amorphous phase if the process is very fast.

This dense plasma phase could be compared to the highly excited Silicon which persists for a fraction of a picosecond<sup>(27,28)</sup>. The interpretation of the laser action differs nevertheless with regard to the following step ; it is generally considered that the solid melts after the initial interaction stage.

In conclusion, few points appear clear today. The laser interaction with the solids results first in the creation of a highly excited non equilibrium phase which persists for a fraction of a picosecond. The question of how this highly excited fluid interaction with the lattice remains still open. Further investigation in the very short impulse regime are certainly desirable to clarify the physical processes in laser annealing.

116

## REFERENCES

1. J.C. WANG, R.F. WOOD and P.P. PRONKO,  
Appl. Phys. Lett. 33, 455 (1978).
2. P. BAERI, S.U. CAMPISANO, G. FOTI and E. RIMINI,  
J. Appl. Phys. 50, 788 (1979).
3. C.M. SURKO, A.L. SIMONS, D.H. AUSTON, J.A. GOLOVCHENKO  
and R.E. SLUSHER,  
Appl. Phys. Lett. 34, 635 (1979).
4. J.C. SCHULTZ and R.J. COLLINS,  
Appl. Phys. Lett. 34, 363 (1979).
5. J.A. VAN VECHTEN, R. TSU and F.W. SARIS,  
Phys. Lett. 74A, 417 (1979) and 74A, 422 (1979).
6. J-F. MORHANGE, G. KANELLIS and M. BALKANSKI,  
Sol. St. Commun. 31, 805 (1979).
7. G. KANELLIS, J-F. MORHANGE and M. BALKANSKI,  
Phys. Rev. B21, 1543 (1980).
8. J.E. SMITH Jr., M.H. BRODSKI, B.L. CROWDER and M.I. NATHAN,  
Light scattering in solids Proceedings of the International  
Conference, Paris (1971), p.330, Flammarion.
9. W.F. TSENG, J-F. MAYER, S.U. CAMPISANO, G. FOTI and E. RIMINI,  
Appl. Phys. Lett. 32, 825 (1978).
10. T.N.C. VENKATESAN, D.H. AUSTON, I.A. GOLOVCHENKO, C.M. SURKO,  
Laser solids Interaction and Laser processing. 1978 AIP  
Conf. Proc. edited by S.D. Ferris, H.J. Leamy and J-M. Poate,  
p.629.

11. R.J. NEMANICH, S.A. SOLIN,  
Phys. Rev. B20, 392 (1979).
12. R. NIKLOW, N. WAKABAYASHI, H.G. SMITH,  
Phys. Rev. B5, 4951 (1972).
13. H.W. LO, A. COMPAAN,  
Appl. Phys. Lett. 38, 499 (1981).
14. M. JOUANNE,  
Private Communication.
15. T.R. HART, R.L. AGGARWAL, B. LAX,  
Phys. Rev. B1, 638 (1970).
16. P.G. KLEMENS,  
Phys. Rev. 148, 845 (1966).
17. M. LIFSHITZ,  
Nuovo Cimento 3, suppl. 716 (1956).
18. P.G. DAWBER, R.J. ELLIOTT,  
Proc. Phys. Soc. 81, 521 (1963).
19. M. BALKANSKI, W. NAZAREWICZ,  
J. Phys. Chem. Sol., 25, 437 (1964).
20. W. NAZAREWICZ, M. BALKANSKI, C. SEBENNE, J-F. MORHANGE,  
Sol. St. Commun. 9, 1719 (1971).
21. J-F. MORHANGE, R. BESERMAN, M. BALKANSKI,  
Physica St. Sol. (a), 23, 383 (1974).
22. M. BALKANSKI, K.P. JAIN, R. BESERMAN and M. JOUANNE,  
Phys. Rev. B12, 4328 (1975).

23. M. JOUANNE, R. BESERMAN, I. IPATOVA, A. SUBASHIEV,  
Solid St. Commun., 16, 1047 (1975).
24. R.C. NEWMAN, R.S. SMITH,  
Proc. of the first Intern. Conf. on Localized Excitation  
in Solids Editor R.F. Wallis, p.117, ( ).
25. M. CHANDRASEKHAR, I.B. RENUCCI and M. CARDONA,  
Phys. Rev., B17, 1623 (1978).
26. R.L. FORK, B.I. GREENE and C.V. SHANK,  
Appl. Phys. Lett., 38, 671 (1981).
27. C.V. SHANK, R. YEN and C. HIRLIMANN,  
Phys. Rev. Lett., 50, 454 (1983).
28. D. HULIN, M. COMBESCOT, J. BOK, A. MIGNS, J-Y. VINET and  
A. AUTENOTTI,  
(To be published).
29. M. BENSOUSSAN and J. de MOISON,  
Phys. Rev., B27, 5192 (1983).
30. M. COMBESCOT and J. BOK,  
Phys. Rev. Lett., 48, 1413 (1982).
31. R.M. MARTIN,  
Phys. Rev. 186, 871 (1969).

ANNEXES :

A.1. LATTICE DYNAMICS OF THIN IONIC SLABS :

- Part I. The electrostatic energy
- Part II. The long range forces
- Part III. Application to GaAs slabs

G. KANELLIS, J-F. MORHANGE and M. BALKANSKI  
Phys. Rev., B28, 3390 (1983).

A.2. ANHARMONIC EFFECTS IN LIGHT SCATTERING DUE TO OPTICAL  
PHONONS IN SILICON :

M. BALKANSKI, R.F. WALLIS and E. HARO  
Phys. Rev., B28, 1928 (1983).

A.3. FUNDAMENTAL OF LASER ANNEALING :

M. BALKANSKI  
International Conference on Laser Processing and  
Diagnostic, July 1984, LINZ.

## Lattice dynamics of thin ionic slabs. I. The electrostatic energy

G. Kanellis,\* J. F. Morhange, and M. Balkanski

*Laboratoire de Physique des Solides de l'Université Pierre et Marie Curie associé au Centre National de la Recherche Scientifique, 4 Place Jussieu, F-75230 Paris Cedex 05, France*

(Received 15 March 1982; revised manuscript received 11 March 1983)

The electrostatic energy per cell for thin slabs of ionic crystals is calculated as a function of the thickness of the slab, its orientation, and the position of the cell with respect to the surfaces. The summation method used is simple and quite general to allow for direct application to slabs of any structure. The depolarization field associated with slabs of certain orientations is also calculated and discussed. Numerical results are given for slabs of the zinc-blende and rocksalt structures.

### I. INTRODUCTION

The properties of small particles of solids (10–~500 Å) and thin films are sometimes very different compared to those of the bulk material. Since the infinite crystal approximation is widely used, calculation of these properties has to overcome, in most cases, the problem of the presence of surfaces.

In particular, lattice-dynamical calculations in finite ionic crystals involve the evaluation of slowly and conditionally converging sums, depending on the shape of the crystal. Hence quantities such as the electrostatic energy per cell, the internal field, and the long-range interaction depend on both the size and the shape of the finite crystal.

De Wette and Schacher<sup>1</sup> discussed these matters in connection with a planewise summation method employed to calculate the internal field in general dipole lattices. Monkhorst and Schwalm<sup>2</sup> treated the electrostatic energy of two-dimensional periodic charge distributions, where they demonstrate the cancellation of singularities in the case of a vanishing dipole moment on the plane of the film and calculated the Madelung energy of some ionic layers.

In this paper (paper I) we report on the electrostatic energy per lattice cell in a thin ionic slab, calculated as a function of its thickness and of the position of the cell with respect to the surfaces, for slabs of different orientations in the zinc-blende and rocksalt structures. Surface cells show up to 10% higher electrostatic energies in certain orientation, assuming they maintain the same structure as the bulk. This fact could be of importance for surface reconstruction and other surface phenomena. Moreover, the depolarization field associated with certain orientations may also influence the stability of the surface layer, through the rearrangement of the elec-

tronic charge it necessitates.

In Sec. II we describe the planewise summation method employed, a variant of Ewald's method, which assures fast convergence and which is very simple and quite general in order to allow for direct application in any case. It has advantages also over the traditional Ewald's method currently used in lattice-dynamical calculations, for it converges faster and it provides results practically independent of the dividing point  $R$ .

In Sec. III we calculate the depolarization field associated with certain orientations of the slab as a function of its thickness. Finally in Sec. IV we give and discuss some results for slabs of the zinc-blende and rocksalt structures.

### II. DEFINITIONS AND METHOD

As defined in the case of an infinite structure, the Madelung constant is a dimensionless number expressing the electrostatic energy per lattice cell with respect to some unit of length (usually the nearest-neighbor separation  $r_0$ ). This energy is of course the same for any cell in an infinite structure, but in a finite crystal it depends on the position of the cell with respect to the surfaces.

Hence it is possible to define two "constants," one the average over the whole finite crystal  $a_{av}(N)$ , depending only on the total number  $N$  of cells in the crystal, and one  $a(l, N)$ , depending both on the position of the cell under consideration [ $l = (l_1 l_2 l_3)$ ] with respect to some reference point in the crystal [ $l = (000)$ ], and the total number  $N$  of the cells in it. In the case of a slab,  $N$  is the number of the cell layers and  $l$  runs from  $(-\infty, -\infty, 0)$  to  $(\infty, \infty, N)$ .

Between these two constants the following relation holds:

$$a_{av}(N) = \frac{1}{N} \sum_l^N a(l, N), \quad (1)$$

where the sum extends over the  $N$  layers of the crystal, and the limit for  $N \rightarrow \infty$  should give the value of the Madelung constant for the infinite crystal.

The position-dependent "constant" can be defined as

$$a(l, N) = \frac{1}{2} \sum_{l \neq l'}^N \sum_{\kappa \neq \kappa'}^N \frac{r_0 \xi_\kappa \xi_{\kappa'}}{|\bar{x}(l', \kappa') - \bar{x}(l, \kappa)|}, \quad (2)$$

where  $\xi_\kappa$  is the fraction of the electronic charge attributed to ion  $\kappa$ .

In the case of a slab parallel to the plane  $(hkl)$  of the crystal, we can always choose such a unit cell that the primitive translation vectors  $\bar{a}_1$  and  $\bar{a}_2$  lie on the plane  $(hkl)$  and  $\bar{a}_3$  lies out of it. The thickness of the slab is measured by the number  $N$  of cells superimposed on the direction perpendicular to the plane  $(hkl)$ . Since the unit cell chosen that way may be a multiple one, the summation over  $\kappa$  has to be performed over all atoms in that cell.

The structure is considered as two dimensional and a two-dimensional reciprocal lattice is associated with it, defined by the vectors

$$\bar{b}_1 = \frac{\bar{a}_2 \times (\bar{a}_1 \times \bar{a}_2)}{|\bar{a}_1 \times \bar{a}_2|^2}, \quad \bar{b}_2 = \frac{(\bar{a}_1 \times \bar{a}_2) \times \bar{a}_1}{|\bar{a}_1 \times \bar{a}_2|^2}. \quad (3)$$

We note also that since the structure is infinite in two dimensions,  $a(l, N)$  becomes a function of the index  $l_3$ , which gives the position of the cell with respect to the surfaces of the slab.

To evaluate the right-hand side of Eq. (2) we use a variant of Ewald's method. We will comment later

$$V(x) = \frac{2}{\sqrt{\pi}} \int_0^\infty \sum_{l'_3=1}^N \sum_{\kappa'=1}^N \xi_{\kappa'} \exp[-|\bar{x}_\perp(l'_3, \kappa') - \bar{x}_\perp|^2 \rho^2] \sum_{l'_1, l'_2} \exp[-|\bar{x}(l'_1, l'_2) + \bar{x}_\parallel(l'_3, \kappa') - \bar{x}_\parallel|^2 \rho^2] d\rho. \quad (8)$$

The sum over  $l'_1, l'_2$  in the above expression is a periodic function in two dimensions and can be expanded in Fourier series,

$$\frac{2}{\sqrt{\pi}} \sum_{l'_1, l'_2} \exp[-|\bar{x}(l'_1, l'_2) + \bar{x}_\parallel(l'_3, \kappa') - \bar{x}_\parallel|^2 \rho^2] = \frac{2\sqrt{\pi}}{s_a \rho^2} \sum_{h_1, h_2} \exp\{-\pi^2 |\bar{y}(h_1, h_2)|^2 / \rho^2 - 2\pi i \bar{y}(h_1, h_2) \cdot [\bar{x}_\parallel(l'_3, \kappa') - \bar{x}_\parallel]\}, \quad (9)$$

where  $s_a = |\bar{a}_1 \times \bar{a}_2|$  and  $\bar{y}(h_1, h_2)$  is a vector of the two-dimensional reciprocal lattice, defined by relations (3).

To keep in close analogy with Ewald's method, one should split the integral in Eq. (8), into two integrals over the intervals  $(0, R)$  and  $(R, \infty)$  using both sides of relation (9). This leads to an expression containing error functions which converges rapidly, but its numerical value depends on the dividing point  $R$  more strongly

on the consequences of using this method.

The potential at a point  $\bar{x}$  due to all ions in a crystal slab is given by

$$V(x, N) = \sum_{l'_3=1}^N \sum_{\kappa'=1}^N \sum_{l'_1, l'_2} \frac{\xi_{\kappa'}}{|\bar{x}(l'_1, l'_2, l'_3, \kappa') - \bar{x}|}, \quad (4)$$

where the sum over  $l'_1$  and  $l'_2$  runs to infinity. To find  $a(l_3, N)$  one takes the limit

$$a(l_3, N) = \frac{r_0}{2} \sum_{\kappa} \xi_{\kappa} \lim_{\bar{x} \rightarrow \bar{x}(l_3, \kappa)} \left[ V(x) - \frac{\xi_{\kappa}}{|\bar{x}(l_3, \kappa) - \bar{x}|} \right], \quad (5)$$

where  $\bar{x}(l_3, \kappa) \equiv \bar{x}(0, 0, l_3, \kappa)$ .

Since by assumption the vectors  $\bar{a}_1$  and  $\bar{a}_2$  lie on the plane of the slab, we can write

$$\begin{aligned} |\bar{x}(l'_1, l'_2, l'_3, \kappa') - \bar{x}|^2 &= |\bar{x}(l'_1, l'_2) + \bar{x}_\parallel(l'_3, \kappa') - \bar{x}_\parallel|^2 \\ &\quad + |\bar{x}_\perp(l'_3, \kappa') - \bar{x}_\perp|^2, \end{aligned} \quad (6)$$

where  $\parallel$  and  $\perp$  designate, respectively, the components of the vectors parallel and perpendicular to the plane  $(hkl)$ .

With the use of relation (6) and the integral representation of  $1/x$ ,

$$\frac{1}{x} = \frac{2}{\sqrt{\pi}} \int_0^\infty \exp(-x^2 \rho^2) d\rho, \quad (7)$$

Eq. (4) becomes

than if unnecessary splitting is avoided.

Since we are going to take the limit of  $V(x)$  for  $\bar{x} \rightarrow \bar{x}(l_3, \kappa)$  [Eq. (5)], the first exponent in Eq. (8) will vanish in the term  $l'_3, \kappa' = l_3 \kappa$ . It will vanish also for  $l'_3 = l_3$  and  $\kappa' = \kappa'' \neq \kappa$  for all ions  $\kappa''$  lying on the plane ( $hkl$ ). Hence we separate out these terms ( $l'_3 = l_3$  and  $\kappa' = \kappa''$ ) and we use only the right-hand side of relation (9) in all terms of Eq. (8) except the last ones, for which the integral has to be split and use of both sides of relation (9) has to be made. We get

$$\begin{aligned}
 V(x, N) = & \frac{2\sqrt{\pi}}{s_a} \sum_{\substack{l'_3=1 \\ l'_3 \neq l_3}}^N \sum_{l_3=1}^N \sum_{\substack{\kappa'=1 \\ \kappa' \neq \kappa''}}^N \sum_{\kappa''=1}^N \xi_{\kappa'} \sum_{h_1, h_2} \int_0^\infty \exp[-|\bar{x}_\perp(l'_3, \kappa') - \bar{x}_\perp|^2 \rho^2 - \pi^2 |\bar{y}(h_1, h_2)|^2 / \rho^2] \frac{d\rho}{\rho^2} \\
 & \times \exp\{-2\pi i \bar{y}(h_1, h_2) \cdot [\bar{x}_\parallel(l'_3, \kappa') - \bar{x}_\parallel]\} \\
 & + \frac{2}{\sqrt{\pi}} \sum_{\kappa''} \xi_{\kappa''} \sum_{l'_1, l'_2} \int_R^\infty \exp[-|\bar{x}(l'_1, l'_2) + \bar{x}_\parallel(l_3, \kappa'') - \bar{x}_\parallel|^2 \rho^2 - |\bar{x}_\perp(l_3, \kappa'') - \bar{x}_\perp|^2 \rho^2] d\rho \\
 & + \frac{2\sqrt{\pi}}{s_a} \sum_{\kappa''} \xi_{\kappa''} \sum_{h_1, h_2} \int_0^R \exp[-\pi^2 |\bar{y}(h_1, h_2)|^2 / \rho^2 - |\bar{x}_\perp(l_3, \kappa'') - \bar{x}_\perp|^2 \rho^2] \frac{d\rho}{\rho^2} \\
 & \times \exp\{-2\pi i \bar{y}(h_1, h_2) \cdot [\bar{x}_\parallel(l_3, \kappa'') - \bar{x}_\parallel]\}, \quad (10)
 \end{aligned}$$

where  $\kappa''$  runs over all ions in the unit cell lying on the same plane ( $hkl$ ) with ion  $\kappa$  ( $\kappa$  included).

Taking the limit in Eq. (5) using the function

$$H(x) \equiv \frac{1}{x} \operatorname{erfc}(x) = \frac{2}{\sqrt{\pi}} \frac{1}{x} \int_x^\infty e^{-t^2} dt, \quad (11)$$

the result<sup>3</sup>

$$\lim_{\bar{x} \rightarrow \bar{x}(l_3, \kappa)} \left[ RH(R |\bar{x}(l_3, \kappa) - \bar{x}|) - \frac{1}{|\bar{x}(l_3, \kappa) - \bar{x}|} \right] = -\frac{2R}{\sqrt{\pi}}, \quad (12)$$

and  $V(x, N)$  from Eq. (10), Eq. (5) becomes

$$\begin{aligned}
 a(l_3, N) = & \frac{r_0}{2} \sum_{\kappa} \xi_{\kappa} \left\{ \frac{2\sqrt{\pi}}{s_a} \sum_{\substack{l'_3=1 \\ l'_3 \neq l_3}}^N \sum_{l_3=1}^N \sum_{\substack{\kappa'=1 \\ \kappa' \neq \kappa''}}^N \sum_{\kappa''=1}^N \xi_{\kappa'} \sum_{h_1, h_2} \int_0^\infty \exp[-|\bar{x}_\perp(l_3, \kappa, l'_3, \kappa')|^2 \rho^2 - \pi^2 |\bar{y}(h_1, h_2)|^2 / \rho^2] \frac{d\rho}{\rho^2} \right. \\
 & \times \exp[-2\pi i \bar{y}(h_1, h_2) \cdot \bar{x}_\parallel(l_3, \kappa, l'_3, \kappa')] \\
 & + R \sum_{\kappa''} \xi_{\kappa''} \sum_{l'_1, l'_2} H(R |\bar{x}(\kappa, l'_1, l'_2, \kappa'')|) \\
 & \left. + \frac{\pi}{R s_a} \sum_{\kappa''} \xi_{\kappa''} \sum_{h_1, h_2} H(\pi |\bar{y}(h_1, h_2)| / R) \exp[-2\pi i \bar{y}(h_1, h_2) \cdot \bar{x}_\parallel(\kappa, \kappa'')] - \frac{2R}{\sqrt{\pi}} \xi_{\kappa} + T(l_3, N) \right\}, \quad (13)
 \end{aligned}$$

where the primed summation signs mean that terms with  $l'_1, l'_2$  for  $\kappa'' = \kappa$  or  $(h_1, h_2) = (00)$  have to be omitted and  $T(l_3, N)$  is just the sum of the  $(h_1, h_2) = (00)$  terms given by

$$T(l_3, N) = \frac{2\sqrt{\pi}}{s_a} \sum_{\substack{l'_3 \\ l'_3 \neq l_3}} \sum_{l_3} \sum_{\substack{\kappa'' \\ \kappa'' \neq \kappa'}} \sum_{\kappa''} \xi_{\kappa''} \int_0^{\infty} \exp[-|\bar{x}_1(l_3, \kappa, l'_3, \kappa')|^2 \rho^2] \frac{d\rho}{\rho^2} + \frac{2\sqrt{\pi}}{s_a} \sum_{\kappa'} \xi_{\kappa'} \int_0^R \frac{d\rho}{\rho^2} \quad (14)$$

The function  $T(l_3, N)$  diverges for  $\rho$  equal to zero. Its limit for  $\rho \rightarrow 0$  is

$$T(l_3, N) = -\frac{2\sqrt{\pi}}{s_a} \left[ \sqrt{\pi} \sum_{\substack{l'_3 \\ l'_3 \neq l_3}} \sum_{l_3} \sum_{\substack{\kappa'' \\ \kappa'' \neq \kappa'}} \sum_{\kappa''} \xi_{\kappa''} |\bar{x}_1(l_3, \kappa, l'_3, \kappa')| + \frac{1}{R} \sum_{\kappa''} \xi_{\kappa''} \right] \quad (15a)$$

since

$$\left[ \sum_{\substack{l'_3 \\ l'_3 \neq l_3}} \sum_{l_3} \sum_{\substack{\kappa'' \\ \kappa'' \neq \kappa'}} \sum_{\kappa''} \xi_{\kappa''} + \sum_{\kappa''} \xi_{\kappa''} \right] \lim_{\rho \rightarrow 0} \left[ \frac{1}{\rho} \right] = 0 \quad (15b)$$

due to the neutrality of the unit cell.

Evaluating the remaining integral in Eq. (13) and using the result (15a) we find

$$\begin{aligned} a(l_3, N) = & \frac{r_0}{2s_a} \sum_{\kappa} \sum_{\substack{l'_3=1 \\ l'_3 \neq l_3}}^N \sum_{l_3=1}^N \sum_{\substack{\kappa'=1 \\ \kappa' \neq \kappa}}^N \sum_{\kappa'=1}^N \sum'_{h_1, h_2} \frac{\xi_{\kappa} \xi_{\kappa'}}{|\bar{y}(h_1, h_2)|} \exp[-2\pi |\bar{y}(h_1, h_2)| |\bar{x}_1(l_3, \kappa, l'_3, \kappa')| \\ & - 2\pi i \bar{y}(h_1, h_2) \cdot \bar{x}(l_3, \kappa, l'_3, \kappa')] \\ & + \frac{r_0 R}{2} \sum_{\kappa} \sum_{\kappa'} \xi_{\kappa} \xi_{\kappa'} \sum'_{l'_1, l'_2} H(R |\bar{x}(\kappa, l'_1, l'_2, \kappa'')|) - \frac{r_0 R}{\sqrt{\pi}} \sum_{\kappa} \xi_{\kappa}^2 - \frac{r_0 \sqrt{\pi}}{R s_a} \sum_{\kappa} \sum_{\kappa'} \xi_{\kappa} \xi_{\kappa'} \\ & + \frac{r_0 \pi}{2R s_a} \sum_{\kappa} \sum_{\kappa'} \xi_{\kappa} \xi_{\kappa'} \sum'_{h_1, h_2} H(\pi |\bar{y}(h_1, h_2)| / R) \exp[-2\pi i \bar{y}(h_1, h_2) \cdot \bar{x}(\kappa, \kappa'')] \\ & - \frac{\pi r_0}{s_a} \sum_{\kappa} \sum_{\kappa'} \xi_{\kappa} \xi_{\kappa'} |\bar{x}_1(\kappa, \kappa')|, \quad (16) \end{aligned}$$

where we dropped the subscript  $||$  as of no importance since the vector  $\bar{y}(h_1, h_2)$  has no component perpendicular to the plane of the slab, and where we also reduced the first sum in (15a) since for the pair of terms with  $\kappa = \kappa_1, \kappa' = \kappa'_1$  and  $\kappa = \kappa'_1, \kappa' = \kappa_1$ , one has

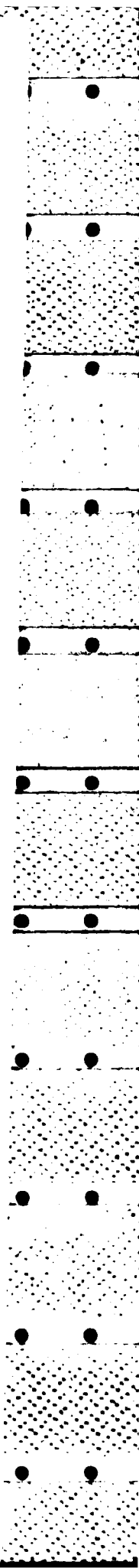
$$|\bar{x}_1(l_3, \kappa_1, l'_3, \kappa'_1)| + |\bar{x}_1(l_3, \kappa'_1, l'_3, \kappa_1)| = 2 |\bar{x}_1(l_3, l'_3)| \quad (17)$$

for all  $l'_3 \neq l_3$ , and hence the sum over  $\kappa$  and  $\kappa'$  is zero for all  $l'_3 \neq l_3$  due to the neutrality of the unit cell.

Equation (16) is our final result. In this expression the sums of  $H(x)$  functions converge rapidly and so does the first sum provided that  $|\bar{x}_1(l_3, \kappa, l'_3, \kappa')|$  is not too small, the slowest convergence occurring when  $l'_3 = l_3$ . For  $N \rightarrow \infty$  and  $l_3$  well away from the surface  $a(l_3, \infty)$  will give the Madelung constant only if the depolarization field is zero as we will show in the next paragraph.

### III. THE DEPOLARIZATION FIELD

The function  $V(x, N)$  defined by Eq. (4) gives the potential at a point  $\bar{x}$  of the space due to all ions in the slab. Its values at a point  $P(\bar{x}_P)$  outside the slab is given by



$$V(x_p, N) = V_f(x_p, N) + V_c(x_p, N), \quad (17a)$$

where

$$V_f(x_p, N) = \frac{1}{s_a} \sum_{l'_3=1}^N \sum_{\kappa'=1}^N \xi_{\kappa'} \sum_{h_1, h_2} \frac{\exp[-2\pi |\bar{y}(h_1, h_2)| |\bar{x}_1(l'_3, \kappa') - \bar{x}_{p1}|]}{|\bar{y}(h_1, h_2)|} \times \exp\{-2\pi i \bar{y}(h_1, h_2) \cdot [\bar{x}_{11}(l'_3, \kappa') - \bar{x}_{p11}]\} \quad (17b)$$

and

$$V_c(x_p, N) = -\frac{2\pi}{s_a} \sum_{l'_3=1}^N \sum_{\kappa'=1}^N \xi_{\kappa'} |\bar{x}_1(l'_3, \kappa') - \bar{x}_{p1}| \quad (17c)$$

as obtained by using only the form of the first sum in Eq. (10) and taking the limit of the first integral in Eq. (14).

The first term,  $V_f(x_p, N)$ , in Eq. (17a) represents the local fluctuations of the potential and it goes to zero for a point  $P$  very distant from the slab. The second term,  $V_c(x_p, N)$ , represents a constant potential and it is independent of the position of the point  $P$  (considered on the same side of the slab). This can be easily shown by taking the charge fraction  $\xi_{\kappa_1}$  of a particular ion  $\kappa_1$  to be

$$\xi_{\kappa_1} = - \sum_{\substack{\kappa' \neq \kappa_1 \\ \kappa'}} \xi_{\kappa'}. \quad (18)$$

Then, assuming a positive  $x_{p1}$  and a unit vector  $\bar{v}_0 = \bar{a}_1 \times \bar{a}_2 / |\bar{a}_1 \times \bar{a}_2|$ ,  $V_c(x_p, N)$  from Eq. (17c) becomes

$$V_c(x_p, N) = V(+\infty, N) = NV(+, 1), \quad (19)$$

where

$$V(+, 1) = -\frac{2\pi}{s_a} \sum_{\substack{\kappa' \neq \kappa_1 \\ \kappa'}} \xi_{\kappa'} [\bar{x}_1(\kappa_1) - \bar{x}_1(\kappa')] \cdot \bar{v}_0 \quad (20)$$

is the potential created on the one side of a set of parallel uniform charged planes through the positions of the ions in a slab of one-unit-cell thickness.

Considering now the potential at a point  $P'$  on the other side of the slab, one finds, apart from the term describing the local fluctuations, a constant term

$$V_c(x_{p'}, N) = V(-\infty, N) = -V(+\infty, N). \quad (21)$$

Hence there is a constant potential difference  $\Delta V_c$  between the two surfaces of the slab, given by

$$\Delta V_c = V(-\infty, N) - V(+\infty, N) = \frac{4\pi}{s_a} N \sum_{\substack{\kappa' \neq \kappa_1 \\ \kappa', \kappa_1}} \xi_{\kappa'} [\bar{x}_1(\kappa_1) - \bar{x}_1(\kappa')] \cdot \bar{v}_0, \quad (22)$$

which is locally modified by the difference of the corresponding terms (17b) for local fluctuations.

Defining a dipole moment for the unit cell by

$$\bar{P}_c = \sum_{\substack{\kappa' \neq \kappa_1 \\ \kappa', \kappa_1}} \xi_{\kappa'} [\bar{x}_1(\kappa_1) - \bar{x}_1(\kappa')] \quad (23)$$

the potential difference  $\Delta V_c$  of Eq. (22) becomes

$$\Delta V_c = \frac{4\pi}{s_a} N \bar{P}_c \cdot \bar{v}_0. \quad (24)$$

The distance between the two surfaces of the slab is

$$L = (N-1)a_1 + d, \quad (25)$$

where  $a_1 = |\bar{a}_3 \cdot \bar{v}_0|$  is the thickness of one unit cell and  $d$  is the distance of the outermost planes of ions belonging to the same cell (Fig. 1).

Assuming that the potential  $\Delta V_c$  [Eq. (24)] drops uniformly across the thickness of the slab, the following field is created:

$$\bar{E}_1(N) = \frac{4\pi}{v_a} \frac{Na_1}{(N-1)a_1 + d} (\bar{P}_c \cdot \bar{v}_0) \bar{v}_0, \quad (26)$$

where  $v_a = s_a \cdot a_1$  is the volume of the unit cell.

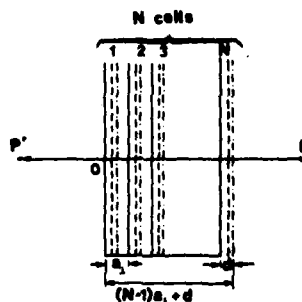


FIG. 1. Schematic representation of a slab consisting of  $N$  one-cell layers.

Increasing the thickness of the slab and taking the limit of Eq. (26) for  $N \rightarrow \infty$ , we find

$$\vec{E}_1(\infty) = \frac{4\pi}{v_a} (\vec{P}_c \cdot \vec{v}_0) \vec{v}_0. \quad (27)$$

Hence the presence of surfaces parallel to charged planes of the crystal produces a macroscopic field  $\vec{E}_1(\infty)$  perpendicular to the surfaces, and consequently the ions are no longer under the same conditions as in the infinite crystal, where no surfaces are present.<sup>3</sup>

To make the slab equivalent from that point of view, with an infinite crystal without surfaces, one has to apply an external field  $\vec{E}_{ex}(N)$  equal in strength and opposite in direction for the total macroscopic field in the slab to be zero. By doing that, the energy per cell changes by the amount

$$W_c(N) = \frac{1}{2} \sum_{\kappa} \xi_{\kappa} V_{ex}(\kappa, N), \quad (28)$$

where  $V_{ex}(\kappa, N)$  is the potential at ion site  $\kappa$  due to the externally applied field.

Using again Eqs. (18) and (23) we find for the change of the energy per cell

$$W_c(N) = \frac{1}{2} \vec{E}_{ex}(N) \cdot \vec{P}_c$$

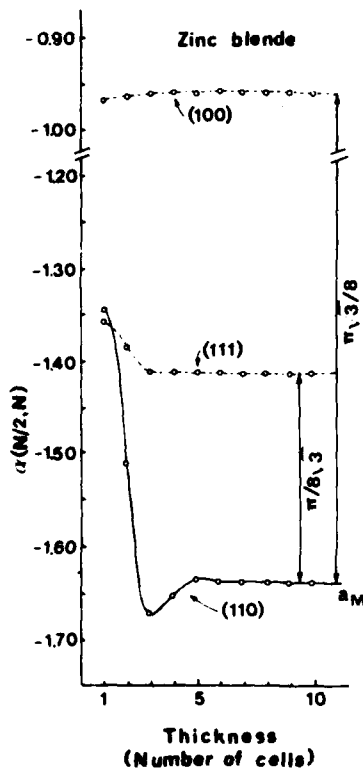


FIG. 2. Electrostatic energy per cell for the central layer, as a function of the thickness of the slab, for slabs of the zinc-blende structure oriented parallel to (100), (11 $\bar{1}$ ), and (110) planes.

$$= -\frac{2\pi}{v_a} \frac{Na_1}{(N-1)a_1+d} (\vec{P}_c \cdot \vec{v}_0)^2, \quad (29)$$

which is a negative quantity or zero if  $\vec{P}_c$  lies on the plane of the slab. The factor depending on  $N$  goes to unity as  $N \rightarrow \infty$ , and in the limit we get

$$W_c(\infty) = -\frac{2\pi}{v_a} (\vec{P}_c \cdot \vec{v}_0)^2. \quad (30)$$

Hence the value of the electrostatic energy per unit cell, obtained by Eq. (16) for  $N \rightarrow \infty$  and  $l_3$  well inside the slab, is higher than that given by the Madelung constant, by  $W_c(\infty)$ ,

$$a_M = \lim_{N \rightarrow \infty} a(N/2, N) + r_0 W_c(\infty), \quad (31)$$

where we multiply  $W_c(\infty)$  by  $r_0$ , the nearest-neighbor distance in order to be consistent with the other terms.

#### IV. RESULTS AND DISCUSSION

Using a variant of the Ewald's summation method we calculated the Coulomb energy per unit

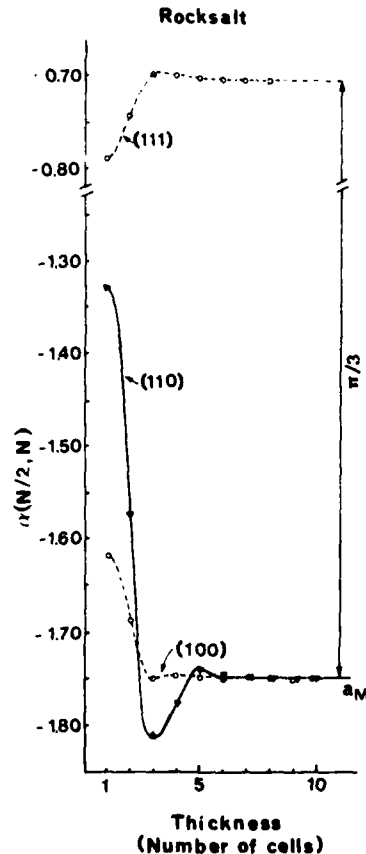


FIG. 3. Electrostatic energy per cell for the central layer, as a function of the thickness of the slab, for slabs of the rock-salt structure oriented parallel to (100), (11 $\bar{1}$ ), and (110) planes.

TABLE I. Electrostatic energy per cell for central cells of thin slabs.

Number of layers ( $N$ )	Central cell ( $N/2$ )	$a(N/2, N)$ for zinc blende <sup>a</sup>			$a(N/2, N)$ for rocksalt <sup>a</sup>		
		(100)	(110)	(11 $\bar{1}$ )	(100)	(110)	(11 $\bar{1}$ )
1	1	0.967 95	1.344 48	1.358 32	1.615 54	1.331 29	0.786 46
2	1	0.963 33	1.508 20	1.384 84	1.682 32	1.570 97	0.743 11
3	2	0.958 71	1.671 92	1.411 36	1.749 10	1.810 64	0.699 75
4	2	0.958 29	1.653 47	1.411 35	1.748 32	1.775 88	0.700 06
5	3	0.957 88	1.635 01	1.411 34	1.747 54	1.741 12	0.700 37
6	3	0.957 88	1.636 70	1.411 34	1.747 55	1.744 70	0.700 37
7	4	0.957 89	1.638 38		1.747 56	1.748 28	
8	4	0.957 89	1.638 21		1.747 56	1.747 88	
9	5		1.638 03			1.747 49	
10	5		1.638 05			1.747 53	

<sup>a</sup>The minus sign is omitted.

cell of thin slabs of the zinc-blende and rocksalt structures for cells of the central layer (or layers when  $N$  is even). In Fig. 2 we show the dependence of  $a(N/2, N)$  on  $N$  for thin slabs of the zinc-blende structure oriented parallel to (100), (11 $\bar{1}$ ), and (110) planes. For each orientation,  $a(N/2, N)$  converges very rapidly to a different limit. The only limit which coincides with the Madelung constant ( $a_M = 1.63806$ ) of an infinite crystal is that for the slab parallel to (110) planes since these planes are through both positive and negative ions and hence neutral. The limit for a slab parallel to (11 $\bar{1}$ ) planes is higher by  $\pi/8\sqrt{3}$ , which is exactly the energy of the unit cell given by Eq. (30) (multiplied by  $r_0$ ). In the case of the slab parallel to (100) planes the limit is higher by  $\pi\sqrt{3}/8$  in accordance with Eq. (30). In both of the latter cases the infinite planes forming the slab are through only one kind of ion (positive or negative) and hence there is a net dipole moment perpendicular to the plane of the slab.

A common feature to all three cases is that  $a(N/2, N)$  tends to its limiting value through an extremum, a maximum in the case of the (100) slab and a minimum in the cases of (11 $\bar{1}$ ) and (110) slabs, in an oscillatory way. For the (110) slab the minimum is most pronounced, lying more than 2% lower than the limiting value  $a_M$ .

In Fig. 3 the dependence of  $a(N/2, N)$  on  $N$  is shown for thin slabs of the rocksalt structure oriented parallel to (100), (11 $\bar{1}$ ), and (110) planes. In both (100) and (110) cases,  $a(N/2, N)$  tends to the value of the Madelung constant (1.74756) since both these planes are neutral, through a minimum which is almost 4% lower than the limiting value for the (110) slab. For slabs parallel to (11 $\bar{1}$ ) planes the limit is higher by  $\pi/3$  in accordance with Eq. (30).

In Table I we summarize the numerical results for the six slabs of different orientations and structures

previously described. The most rapid convergence of  $a(N/2, N)$  to its limiting value is observed for slabs of (11 $\bar{1}$ ) orientation in both structures, and the slowest is for slabs oriented parallel to (110) planes.

In Table II we give the values of the electrostatic energy per cell  $a(l_3, N)$  for cells at different distances from the surface for a thin slab of the zinc-blende structure, oriented parallel to (100), (110), and (11 $\bar{1}$ ) planes. It can be seen that the limiting value is reached within even the second layer for the (11 $\bar{1}$ ) slab, while for the (110) slab it is reached at a deeper layer.

In Fig. 4 we give the dependence of the electrostatic energy per cell [ $r_0 W_c(N)$ , Eq. (29)] due to a macroscopic field equal in strength and opposite in direction to the field created by the slab of  $N$  layers. Among the cases considered here, such a field is created by the (11 $\bar{1}$ ) and (100) slabs of the zinc-blende structure and by the (11 $\bar{1}$ ) slab of rocksalt structure. The corresponding limiting values are reached very slowly but the convergence is the same

TABLE II. Electrostatic energy per cell, in a slab of 20 layers, for layers in different distances from the surface.

Layer from surface ( $l_3$ )	$a(l_3, 20)$ for zinc blende <sup>a</sup>		
	(100)	(110)	(11 $\bar{1}$ )
0	0.962 92	1.491 27	1.384 82
1	0.958 30	1.654 99	1.411 34
2	0.957 89	1.636 54	1.411 34
3	0.957 89	1.638 22	1.411 34
4		1.638 05	
5		1.638 07	
6		1.638 06	

<sup>a</sup>The minus sign is omitted.

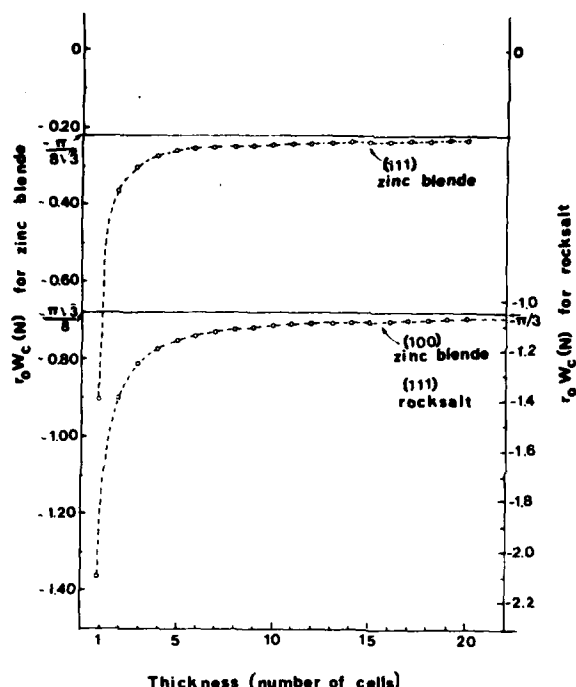


FIG. 4. Electrostatic energy of a cell in the macroscopic field of the slab as a function of its thickness, for  $(11\bar{1})$  and  $(100)$  slabs of the zinc-blende structure (left-hand scale) and  $(11\bar{1})$  slab of the rocksalt structure (right-hand scale).

for the  $(100)$  zinc-blende and the  $(11\bar{1})$  rocksalt slabs. For slabs with 50–70 layers the calculated values are within 1% of their limits.

It is worthwhile to note that although for  $N \rightarrow \infty$  Eq. (2) is the definition of the Madelung constant, its limit for  $N \rightarrow \infty$  depends on the orientation of the slab. This is due to the fact that the series in the right-hand side of Eq. (2) is not absolutely convergent and hence its limit depends on the way of summation. Any method summing first on infinite planes cannot avoid creating a constant potential outside the planes and hence a depolarization field if the dipole moment of the cell has a nonzero component perpendicular to the plane of summation.

Monkhorst and Schwalm<sup>2</sup> calculated the electrostatic energy of a layer of the NaCl structure parallel to the  $(100)$  plane in different distorted configurations. Our result for one layer of the undistorted

lattice is in exact agreement with their corresponding result (namely the value  $-1.61554$ ). The increase of the energy, as their layer is separated into two oppositely charged sheets, is due to the same reason we already explained and the term  $E_3$  in their energy of the layer is equivalent to our result of Eq. (28).

A final remark concerns their suggestion to treat the electrostatic energy of systems of point charges in terms of coefficients  $\phi_{\kappa\kappa'}$  of the  $\xi_{\kappa}\xi_{\kappa'}$  products. For diatomic ionic crystals there is only one such coefficient, the Madelung constant itself (since  $\xi_2 = -\xi_1$ ). For crystals with more atoms per unit cell, with at least three different  $\xi_{\kappa}$ , such an expression will save considerable computation time and will point out relations between structure factors in structures and superstructures. We have found that the Madelung constant of the chalcopyrite structure (which is a superstructure of the zinc blende) can be expressed as

$$a_{\text{ch}} = -2.13925(\xi_1^2 + \xi_2^2) - 2.27378\xi_1\xi_2, \quad (32)$$

where  $\xi_1$  and  $\xi_2$  are the two cation charge fractions. For  $\xi_1 = \xi_2 = 1$ ,  $a_{\text{ch}}$  equals 4 times the Madelung constant of the zinc-blende structure, since the unit cell for the ideal chalcopyrite is 4 times larger.

After this paper was submitted for publication, V. V. Avilov<sup>4</sup> proposed formulas to calculate the electrostatic energy of planar lattices. Apart from an obvious typing error, the potential of a planar lattice of charges at a distance  $|z|$  from its plane, represented as a Fourier series in the plane, is given in this paper as exactly the same as in our calculations. In our opinion, the uniform background charge distribution of opposite sign assumed to remove the divergence of the sum results in an unrealistic picture for a slab or an infinite crystal with two parallel surfaces. It does in fact implicitly compensate for the depolarization field through a multilayer (or a two-layer) sandwich of uniform charge distributions of opposite polarity, but without its source and importance being demonstrated.

One of us (G.K.) thanks Dr. K. Kunc and Dr. M. Kanehisa for many helpful discussions. This research was supported by Direction des Recherches Etudes et Technique (DRET) Contract No. 79/1101.

\*Permanent address: First Laboratory of Physics, University of Thessaloniki, Thessaloniki, Greece.

<sup>1</sup>F. W. de Wette and G. E. Schacher, Phys. Rev. **137**, A78 (1965).

<sup>2</sup>H. J. Monkhorst and W. A. Schwalm, Phys. Rev. B **23**,

1729 (1981).

<sup>3</sup>M. Born and K. Huang, *Dynamical Theory of Crystal Lattices* (Oxford University Press, New York, 1968), see Appendix II.

<sup>4</sup>V. V. Avilov, Solid State Commun. **44**, 555 (1982).

Errata

Erratum: Lattice dynamics of thin ionic slabs. I. The electrostatic energy  
[Phys. Rev. B 28, 3390 (1983)]

G. Kanellis, J. F. Morhange, and M. Balkanski

Please make the following changes to our paper.

(1) Page 3391, in Eq. (2), instead of

$$\frac{1}{2} \sum_{l=1}^N \sum_{l'=1}^N \sum_{\kappa=1}^N \sum_{\kappa'=1}^N$$

write

$$\frac{1}{2} \sum_{\kappa} \sum_{l'} \sum_{\kappa'}$$

(2) Page 3391, in Eqs. (4) and (8), the sum over  $\kappa'$  runs from 1 to the number of ions in the unit cell (not to  $N$ ).  
 (3) Page 3392, in the first line of Eqs. (10) and (13), instead of

$$\frac{2\sqrt{\pi}}{s_a} \sum_{l'_3=1}^N \sum_{l_3=1}^N \sum_{\kappa'=1}^N \sum_{\kappa''=1}^N \xi_{\kappa'} \dots$$

write

$$\frac{2\sqrt{\pi}}{s_a} \sum_{l'_3=1}^N \sum_{\kappa'} \xi_{\kappa'} \dots$$

(4) Page 3393, in the first line of the text, instead of ... terms with  $l'_1, l'_2$  for ..., write ... terms with  $(l'_1, l'_2) = (0, 0)$  for

(5) Page 3393, in Eqs. (14), (15a), and (15b), instead of

$$\sum_{l'_3=1}^N \sum_{l_3=1}^N \sum_{\kappa'} \sum_{\kappa''} \xi_{\kappa'} \dots$$

write

$$\sum_{l'_3=1}^N \sum_{\kappa'} \xi_{\kappa'} \dots$$

(6) Page 3393, in the first line of Eq. (16), instead of

$$\sum_{\kappa} \sum_{l'_3=1}^N \sum_{l_3=1}^N \sum_{\kappa'=1}^N \sum_{\kappa''=1}^N \sum_{h_1, h_2} \dots$$

write

$$\sum_{\kappa} \sum_{l'_3=1}^N \sum_{\kappa'} \sum_{h_1, h_2} \dots$$

## Lattice dynamics of thin ionic slabs. II. The long-range forces

G. Kanellis,\* J. F. Morhange, and M. Balkanski

Laboratoire de Physique des Solides de l'Université Pierre et Marie Curie associé au Central National de la Recherche Scientifique, 4 Place Jussieu, F-75230 Paris Cedex 05, France

(Received 15 March 1982; revised manuscript received 11 March 1983)

The Coulomb interaction is calculated for thin ionic slabs of any structure and orientation. For ions lying on different planes, parallel to the plane of the slab, the direct-space double sum is transformed into a rapidly converging double sum in reciprocal space only, while for ions lying on the same plane, a two-dimensional version of Ewald's method is used. Finally we comment on the macroscopic field associated with long-wavelength vibrations of an infinite lattice on the basis of a two-dimensional summation method.

### I. INTRODUCTION

There is great interest in the physics of surfaces and thin-film phenomena and much attention has been drawn to the study of surface-localized vibrational modes of crystals. To investigate these modes in thin slabs of ionic crystals by direct lattice-dynamical calculations, one needs to calculate the long-range interaction between plane lattices. This task involves the evaluation of dipole lattice sums with an infinite number of terms, in two dimensions. Since lattice sums in general are conditionally converged, two-dimensional summation methods in themselves imply conditions leading to different results which have to be interpreted.

Niiboer and de Wette<sup>1</sup> and de Wette and Schachet<sup>2</sup> discussed these matters when calculating the internal field in dipole lattices and they pointed out how the sums are influenced by the orientation of the planes on which the summation is performed with respect to the dipole direction. They propose a planewise summation method which can be used to calculate the long-range interaction in thin slabs, but they do not derive expressions for such a case.

Detailed calculations on finite ionic slabs have been carried out by Tong and Maradudin.<sup>3</sup> These authors treated in detail the long-range interaction in the case of a slab of the rocksalt structure parallel to the (100) plane, using a method proposed by Mackenzie. The same case has also been treated by Bryksin and Firsov<sup>4</sup> and by Jones and Fuchs<sup>5</sup> for retarded and unretarded interaction, but on different bases.

In this paper we derive explicit expressions for the coupling coefficients due to unretarded long-range forces between the plane lattices in an ionic slab, whatever its structure and orientation. This is done following a procedure similar to the one presented in the preceding paper, referred to as paper I, where we

calculated the electrostatic energy per cell in thin ionic slabs. We believe the method we propose here, a variant of Ewald's method, is quite general, straightforward, and simple, and hence more convenient to use.

Finally we comment on the macroscopic field associated with long-wavelength vibrations of an infinite lattice. In fact a planewise (two-dimensional) summation method for the Coulomb interactions can never give the formal results of Ewald's method for the macroscopic field without additional assumptions concerning the effect due to the presence of surfaces.

### II. COULOMB INTERACTIONS BETWEEN IONS

We consider, as in paper I, a crystal slab consisting of  $N$  one-cell layers, parallel to the  $(hkl)$  plane of the crystal structure. By appropriate choice of the unit cell, the primitive translation vectors  $\bar{a}_1$  and  $\bar{a}_2$  can be taken to lie on the  $(hkl)$  plane, while  $\bar{a}_3$  lies out of it. The slab is considered as a two-dimensional periodic structure and a two-dimensional reciprocal lattice is associated with it, defined by the vectors  $\bar{b}_1$  and  $\bar{b}_2$  [Eq. (3) of paper I].

The field at a point  $\bar{x}$  due to all point dipoles  $\bar{p}(l', \kappa')$  at lattice sites  $\bar{x}(l', \kappa')$ ,  $l' = (l'_1, l'_2, l'_3)$ , is given by

$$E_\alpha(\bar{x}) = \sum_{l'_1, l'_2} \sum_{\beta} p_\beta(l'_1, \kappa') \frac{\partial^2}{\partial x_\alpha \partial x_\beta} \times \sum_{l'_1, l'_2} \frac{\exp[2\pi i \bar{y} \cdot \bar{x}(l', \kappa')]}{|\bar{x}(l', \kappa') - \bar{x}|}, \quad (1)$$

where  $\alpha, \beta = (1, 2, 3)$  number the axis of some Cartesian coordinate system  $Ox_1x_2x_3$ ,  $\kappa'$  runs over all

ions in the unit cell,  $l'$  runs over all unit cells from  $(-\infty, -\infty, 0)$  to  $(\infty, \infty, N)$ , and  $\vec{y}$  is a two-dimensional wave vector.

We note that the index  $l_3$  labels the one-unit-cell layers of the slab. Hence the index  $(l_3, \kappa)$  labels the atoms in the long unit cell of the two-dimensional

periodic structure defined by the vectors  $(\vec{a}_1, \vec{a}_2, N\vec{a}_3)$ . To evaluate the sum over  $l'_1, l'_2$  on the right-hand side of Eq. (1) we proceed the same way as in evaluating the double sums in paper I.

Using the integral representation of  $1/x$  [Eq. (7) of paper I] and again setting

$$|\vec{x}(l', \kappa') - \vec{x}|^2 = |\vec{x}(l'_1, l'_2) + \vec{x}_{||}(l'_3, \kappa') - \vec{x}_{||}|^2 + |\vec{x}_{\perp}(l'_3, \kappa') - \vec{x}_{\perp}|^2, \quad (2)$$

where  $||$  and  $\perp$  designate the components of the vectors parallel and perpendicular to the plane  $(hkl)$ , respectively, relation (1) becomes

$$E_{\alpha}(\vec{x}) = \sum_{l'_3, \kappa'} \sum_{\beta} \rho_{\beta}(l'_3, \kappa') \frac{\partial^2}{\partial x_{\alpha} \partial x_{\beta}} \int_0^{\infty} \exp[-|\vec{x}_{\perp}(l'_3, \kappa') - \vec{x}_{\perp}|^2 \rho^2 + 2\pi i \vec{y} \cdot \vec{x}] \\ \times \frac{2}{\sqrt{\pi}} \sum_{l'_1, l'_2} \exp\{-|\vec{x}(l'_1, l'_2) + \vec{x}_{||}(l'_3, \kappa') - \vec{x}_{||}|^2 \rho^2 \\ + 2\pi i \vec{y} \cdot [\vec{x}(l'_1, l'_2) + \vec{x}_{||}(l'_3, \kappa') - \vec{x}_{||}]\} d\rho, \quad (3)$$

since the vector  $\vec{y}$  lies on the plane of the slab.

The sum over  $l'_1, l'_2$  on the right-hand side of Eq. (3) is a periodic function in two dimensions and can be expanded in Fourier series

$$\frac{2}{\sqrt{\pi}} \sum_{l'_1, l'_2} \exp\{-|\vec{x}(l'_1, l'_2) + \vec{x}_{||}(l'_3, \kappa') - \vec{x}_{||}|^2 \rho^2 + 2\pi i \vec{y} \cdot [\vec{x}(l'_1, l'_2) + \vec{x}_{||}(l'_3, \kappa') - \vec{x}_{||}]\} \\ = \frac{2\sqrt{\pi}}{s_a \rho^2} \sum_{h_1, h_2} \exp\{-\pi^2 |\vec{y}(h_1, h_2) + \vec{y}|^2 / \rho^2 - 2\pi i \vec{y}(h_1, h_2) \cdot [\vec{x}_{||}(l'_3, \kappa') - \vec{x}_{||}]\}, \quad (4)$$

where  $s_a = |\vec{a}_1 \times \vec{a}_2|$  and  $\vec{y}(h_1, h_2)$  is a vector of the two-dimensional reciprocal lattice.

Here again, as explained in paper I, one can introduce a dividing point  $R$  on the  $\rho$  axis and evaluate the integral in Eq. (3) separately over the interval  $(0, R)$  using the right-hand side of relation (4) and over the interval  $(R, \infty)$  keeping the integrand as it is.

Splitting the integral in Eq. (3) is necessary only if  $|\vec{x}_{\perp}(l'_3, \kappa') - \vec{x}_{\perp}| = 0$  for some  $(l'_3, \kappa')$ , i.e., if the vector  $\vec{x}(l'_3, \kappa') - \vec{x}$  lies entirely on the plane  $(hkl)$  through the ion  $(l'_3, \kappa')$ .

In calculating the Coulomb interaction between ions, one is interested in the field at ion sites  $\vec{x}(l_3, \kappa)$ . It will happen then to be  $|\vec{x}_{\perp}(l'_3, \kappa') - \vec{x}_{\perp}(l_3, \kappa)| = 0$  for  $l'_3, \kappa' = l_3, \kappa''$ , where  $\kappa''$  labels all ions of the unit cell on the same  $(hkl)$  plane through ion  $\kappa$  ( $\kappa$  includ-

ed).

Hence we can consider the field  $E_{\alpha}(\vec{x})$  as being the sum of two components,

$$E_{\alpha}(\vec{x}) = E_{\alpha}^{(1)}(\vec{x}) + E_{\alpha}^{(2)}(\vec{x}), \quad (5)$$

where  $E_{\alpha}^{(1)}(\vec{x})$  is the field at point  $\vec{x}$  due to all ions outside the plane  $(hkl)$  through that point and  $E_{\alpha}^{(2)}(\vec{x})$  is the field at the same point due to all ions lying on the plane  $(hkl)$ . We distinguish the following two cases:

*Case A:*  $|\vec{x}_{\perp}(l'_3, \kappa') - \vec{x}_{\perp}| \neq 0$ . Since we are later going to replace  $\vec{x}$  by  $\vec{x}(l_3, \kappa)$ , this will be the case for  $(l'_3, \kappa') \neq (l_3, \kappa'')$  as already indicated. We proceed by evaluating the integral in Eq. (3), using only the right-hand side of relation (4). Then for  $E_{\alpha}^{(1)}(\vec{x})$  we have

$$E_{\alpha}^{(1)}(\vec{x}) = \sum_{\substack{l'_3, \kappa' \neq l_3, \kappa'' \\ l'_3, \kappa', l_3, \kappa''}} \sum_{\beta} \rho_{\beta}(l'_3, \kappa') \frac{\partial^2}{\partial x_{\alpha} \partial x_{\beta}} \frac{1}{s_a} \exp(2\pi i \vec{y} \cdot \vec{x}) \\ \times \sum_{h_1, h_2} \frac{1}{|\vec{y}(h_1, h_2) + \vec{y}|} \exp\{-2\pi |\vec{y}(h_1, h_2) + \vec{y}| |\vec{x}_{\perp}(l'_3, \kappa') - \vec{x}_{\perp}| \\ - 2\pi i \vec{y}(h_1, h_2) \cdot [\vec{x}_{||}(l'_3, \kappa') - \vec{x}_{||}]\}. \quad (6)$$

Before carrying out the differentiation in Eq. (6), we note that the unit vector  $\vec{v}_0$  perpendicular to the plane ( $hkl$ ) is, by the assumption for the choice of the unit cell,

$$\vec{v}_0 = \frac{\vec{a}_1 \times \vec{a}_2}{|\vec{a}_1 \times \vec{a}_2|} = \cos\alpha \vec{x}_{01} + \cos\beta \vec{x}_{02} + \cos\gamma \vec{x}_{03}, \quad (7)$$

with respect to the coordinate system  $Ox_1x_2x_3$ .

Hence

$$\frac{\partial}{\partial x_\alpha} |\vec{x}_1(l'_3, \kappa') - \vec{x}_1| = s_g \frac{\partial}{\partial x_\alpha} [\vec{x}(l'_3, \kappa') \cdot \vec{v}_0 - \vec{x} \cdot \vec{v}_0] = -s_g \cos\alpha, \quad (8a)$$

where

$$s_g = \begin{cases} +1 & \text{if } \vec{x}(l'_3, \kappa') \cdot \vec{v}_0 > \vec{x} \cdot \vec{v}_0 \\ -1 & \text{if } \vec{x}(l'_3, \kappa') \cdot \vec{v}_0 < \vec{x} \cdot \vec{v}_0 \end{cases} \quad (8b)$$

and

$$\frac{\partial^2}{\partial x_\alpha \partial x_\beta} |\vec{x}_1(l'_3, \kappa') - \vec{x}_1| = 0. \quad (8c)$$

Carrying out the differentiation and evaluating the derivatives for  $\vec{x} = \vec{x}(l_3, \kappa)$ , we get

$$E_\alpha^{(1)}(l_3, \kappa) = \sum_{\substack{l'_3, \kappa' \neq l_3, \kappa \\ l'_3, \kappa', l_3, \kappa}} \sum_{\beta} p_\beta(l'_3, \kappa') Q_{\alpha\beta}(l_3, \kappa; l'_3, \kappa' | \vec{y}) \exp[2\pi i \vec{y} \cdot \vec{x}(l_3, \kappa)], \quad (9)$$

where

$$Q_{\alpha\beta}(l_3, \kappa; l'_3, \kappa' | \vec{y}) = \frac{4\pi^2}{s_\alpha} \sum_{h_1, h_2} \left\{ -\frac{[y_\alpha(h_1, h_2) + y_\alpha][y_\beta(h_1, h_2) + y_\beta]}{|\vec{y}(h_1, h_2) + \vec{y}|} + |\vec{y}(h_1, h_2) + \vec{y}| \cos\alpha \cos\beta \right. \\ \left. + i s_g \{ [y_\alpha(h_1, h_2) + y_\alpha] \cos\beta + [y_\beta(h_1, h_2) + y_\beta] \cos\alpha \} \right\} \\ \times \exp[-2\pi i |\vec{y}(h_1, h_2) + \vec{y}| |\vec{x}_1(l_3, \kappa, l_3, \kappa') - \vec{x}| - 2\pi i \vec{y}(h_1, h_2) \cdot \vec{x}(l_3, \kappa, l'_3, \kappa')]. \quad (10)$$

In the last equation we dropped the index  $||$  as of no importance, since the vector  $\vec{y}(h_1, h_2)$  lies on the plane of the slab.

It is worthwhile noticing that the above expression for  $Q_{\alpha\beta}(l_3, \kappa; l'_3, \kappa' | \vec{y})$  is a regular function of  $|\vec{y}|$  having a well-defined limit for  $|\vec{y}| \rightarrow 0$ . This can be easily verified by separating the  $(h_1, h_2) = (0, 0)$  terms on the right-hand side of Eq. (10). Their sum tends always to zero for  $\vec{y} \rightarrow 0$  regardless of the direction of the vector  $\vec{y}$ .

*Case B:*  $|\vec{x}_1(l'_3, \kappa') - \vec{x}_1| = 0$ . This will be the case for  $\vec{x} = \vec{x}(l_3, \kappa)$  and  $(l'_3, \kappa') = (l_3, \kappa'')$  where  $\kappa''$  runs over all ions of the unit cell lying on the same ( $hkl$ ) plane with ion  $\kappa$ . In this case we split the integral in Eq. (3) into two integrals over the intervals  $(0, R)$  and  $(R, \infty)$  using both sides of relation (4). We get for  $E_\alpha^{(2)}(\vec{x})$ ,

$$E_\alpha^{(2)}(\vec{x}) = \sum_{\kappa''} \sum_{\beta} p_\beta(l_3, \kappa'') \frac{\partial^2}{\partial x_\alpha \partial x_\beta} \left\{ R \sum_{l'_1, l'_2} H(R | \vec{x}(l'_1, l'_2, l_3, \kappa'') - \vec{x} |) \exp[2\pi i \vec{y} \cdot \vec{x}(l'_1, l'_2, l_3, \kappa'')] \right. \\ \left. + \frac{\pi}{R s_\alpha} \sum_{h_1, h_2} H(\pi |\vec{y}(h_1, h_2) + \vec{y}| / R) \right. \\ \left. \times \exp[2\pi i \{ \vec{y}(h_1, h_2) + \vec{y} \} \cdot \vec{x} - 2\pi i \vec{y}(h_1, h_2) \cdot \vec{x}(l_3, \kappa'')] \right\}, \quad (11)$$

where we used the function

$$H(x) = \frac{2}{\sqrt{\pi}} \frac{1}{x} \int_x^\infty e^{-t^2} dt \quad (12)$$

to express both integrals.

The function  $H(x)$  diverges for  $x=0$ . Hence the term  $(l'_1 l'_2) = (00)$  on the right-hand side of Eq. (11) will diverge for  $\kappa'' = \kappa$ . Performing the differentiation and replacing  $\bar{x}$  by  $\bar{x}(l_3, \kappa)$  we get for  $E_a^{(2)}(\bar{x})$ ,

$$E_a^{(2)}(\bar{x}) = \sum_\beta \left[ \sum_{\substack{\kappa'' \neq \kappa \\ \kappa'', \kappa}} p_\beta(l_3, \kappa'') Q_{\alpha\beta}(l_3, \kappa; l_3, \kappa'' | \bar{y}) + Q_{\alpha\beta}(l_3, \kappa; l_3, \kappa | \bar{y}) \right] \exp[2\pi i \bar{y} \cdot \bar{x}(l_3, \kappa)], \quad (13)$$

where

$$\begin{aligned} Q_{\alpha\beta}(l_3, \kappa; l_3, \kappa'' | \bar{y}) = & R^3 \sum_{l'_1, l'_2} H_{\alpha\beta}(R | \bar{x}(\kappa, l'_1, l'_2, \kappa'') |) \exp[2\pi i \bar{y} \cdot \bar{x}(\kappa, l'_1, l'_2, \kappa'')] \\ & - \frac{4\pi^2}{R s_a} \sum_{h_1, h_2} [\gamma_\alpha(h_1, h_2) + \gamma_\alpha] [\gamma_\beta(h_1, h_2) + \gamma_\beta] H(\pi | \bar{y}(h_1, h_2) + \bar{y} | / R) \\ & \times \exp[2\pi i \bar{y}(h_1, h_2) \cdot \bar{x}(\kappa'', \kappa)], \end{aligned} \quad (14)$$

$Q_{\alpha\beta}(l_3, \kappa; l_3, \kappa | \bar{y})$  is the diverged term, to be evaluated, and

$$H_{\alpha\beta}(|\bar{x}|) = \frac{\partial^2}{\partial x_\alpha \partial x_\beta} H(|\bar{x}|). \quad (15)$$

To find  $Q_{\alpha\beta}(l_3, \kappa; l_3, \kappa | \bar{y})$  one has to subtract from the right-hand side of Eq. (11) the contribution in the potential at ion site  $(l_3, \kappa)$  due to the ion  $(l_3, \kappa)$  itself.

This is done by taking the limit

$$\begin{aligned} \lim_{\bar{x} \rightarrow \bar{x}(l_3, \kappa)} \left[ \frac{\partial^2}{\partial x_\alpha \partial x_\beta} \left[ H(R | \bar{x}(0, 0, l_3, \kappa) - \bar{x} |) - \frac{1}{|\bar{x}(l_3, \kappa) - \bar{x}|} \right] \right] \\ = \lim_{\bar{x} \rightarrow \bar{x}(l_3, \kappa)} \left[ \frac{\partial^2}{\partial x_\alpha \partial x_\beta} \left[ -\frac{1}{R |\bar{x}(l_3, \kappa) - \bar{x}|} \frac{2}{\sqrt{\pi}} \int_0^{R |\bar{x}(l_3, \kappa) - \bar{x}|} \exp(-t^2) dt \right] \right] = \frac{4}{3\sqrt{\pi}} \delta_{\alpha\beta}, \end{aligned} \quad (16)$$

where  $\delta_{\alpha\beta}$  is Kronecker's  $\delta$ . By naming the function in the square brackets of Eq. (16) as  $H_{\alpha\beta}^0(x)$  and considering the above-found result as its limit for  $x \rightarrow 0$ , we can retain Eq. (14) as the general formal expression for  $Q_{\alpha\beta}(l_3, \kappa; l_3, \kappa'' | \bar{y})$  bearing in mind that in the case of  $\kappa = \kappa''$ , one has to replace in the term  $(l_1 l_2) = (00)$  the function  $H_{\alpha\beta}(x)$  by  $H_{\alpha\beta}^0(x)$ .

We note again that the right-hand side of Eq. (14) is a regular function of  $|\bar{y}|$ . The sum of the  $h_1 h_2 = (00)$  terms goes to zero for  $|\bar{y}| \rightarrow 0$ , whatever the direction of the vector  $\bar{y}$  is.

For the coefficients  $Q_{\alpha\beta}(l_3, \kappa; l'_3, \kappa'' | \bar{y})$  given by Eqs. (10) and (14), the following symmetry relations hold:

$$Q_{\alpha\beta}(l_3, \kappa; l'_3, \kappa' | \bar{y}) = Q_{\beta\alpha}(l_3, \kappa; l'_3, \kappa' | \bar{y}), \quad (17a)$$

$$Q_{\alpha\beta}(l_3, \kappa; l'_3, \kappa' | \bar{y}) = Q_{\alpha\beta}^*(l'_3, \kappa'; l_3, \kappa | \bar{y}), \quad (17b)$$

$$Q_{\alpha\beta}(l_3, \kappa; l'_3, \kappa' | \bar{y}) = Q_{\alpha\beta}^*(l_3, \kappa; l'_3, \kappa' | -\bar{y}). \quad (17c)$$

Relation (17a) can be verified by inspection from Eq. (10) and by calculating  $H_{\alpha\beta}(x)$  for Eq. (14),  $H_{\alpha\beta}(x)$  being also symmetric in  $x_\alpha, x_\beta$ . Relation (17b) is also true for Eq. (10) because of the condition (8b) while for Eq. (14) the summation indices  $l'_1, l'_2$  have to be replaced by  $-l'_1, -l'_2$ . Finally, relation (17c) is verified for both Eqs. (10) and (14) by replacing the indices  $h_1, h_2$  by  $-h_1, -h_2$ .

### III. ON THE MACROSCOPIC FIELD

In the three-dimensional case the macroscopic field is produced by the infinite charged planes, through the positions of the vibrating ions, perpendicular to the direction of the wave vector  $\bar{q}$ , for long-wavelength vibrations ( $\bar{q} \rightarrow \bar{0}$ ). Its value turns out to be equal to a nonregular, for the  $\bar{q} \rightarrow \bar{0}$  term, of the sum of the  $(h_1 h_2 h_3) = (000)$  terms in the expression for the exciting field at a dipole site.<sup>6</sup> It is

given by

$$\vec{E}^{\text{mac}} = -\frac{4\pi}{v_a} \frac{\vec{q}}{|\vec{q}|} \frac{\vec{q}}{|\vec{q}|} \cdot \sum_{\kappa} \vec{p}(\kappa), \quad (18)$$

where  $v_a$  is the volume of the unit cell and  $\vec{p}(\kappa)$  is the dipole moment associated with the ion  $\kappa$ .

In the preceding paragraph we have shown that such a term exists neither in Eq. (8) nor in Eq. (11) for the exciting field. Since the macroscopic field, according to Eq. (18), is on the same direction with vector  $\vec{q}$ , we have to conclude that there is not a macroscopic field lying on the plane of the slab. This is of course what one should expect, since in the present case there exist no infinite oscillating charged planes perpendicular to the plane of the slab, but rather, plane-charged "strips" infinite in one dimension. Consequently in slab-shaped crystals, longitudinal and transverse phonons propagated on the plane of the slab must be of the same frequency, as far as no displacements perpendicular to the plane of the slab are involved.

On the other hand, there are infinite oscillating charged planes parallel to the plane of the slab. Hence a macroscopic field must appear perpendicular to that plane due to vibrations along this direction. To calculate that field we consider the potential distribution inside the slab (Fig. 1). We have shown in paper I [Eq. (22)] that, depending on the orientation, a constant potential difference  $\Delta V_c(N)$

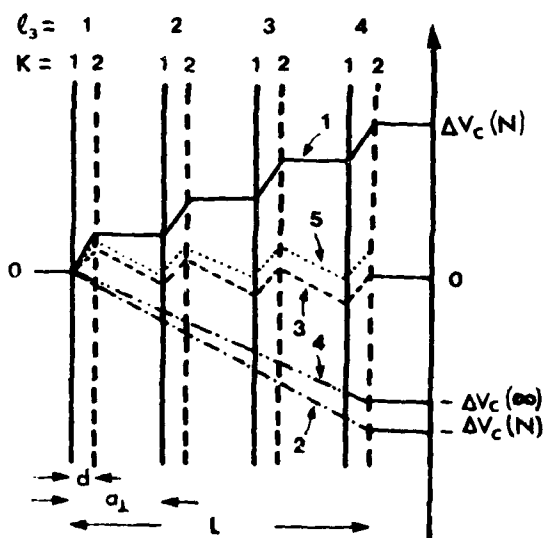


FIG. 1. Potential distribution in a thin slab. (1) Static potential created by the charged planes, (2) external potential compensating the former one, (3) final distribution resulting from the superposition of (1) and (2), (4) external potential when the slab is considered as part of an infinite structure, (5) potential distribution in an infinite crystal, i.e., superposition of (1) and (4).

is created between its two free surfaces.

We would like to emphasize at this point that the interaction due to electrostatic potentials calculated in a preceding paragraph is correct and accurate as far as the slab is considered to be taken out of an infinite structure. Moreover, no question arises for the zero-wave-vector limit perpendicular to the plane of the slab, since no periodic boundary condition has been imposed along that direction. What we are going to show is that the well-known macroscopic field in the infinite-crystal case is due to infinite distant planes (missing in the case of a slab) and moreover how this field could be taken into account especially in the case where the surfaces of the slab are not free.

To derive an appropriate expression for the constant potential difference  $\Delta V_c$  between the two surfaces of the slab, we recall Eq. (17c) of paper I for the constant term  $V_c$  of the potential at a point  $P(\vec{x}_p)$  outside the slab,

$$V_c(x_p, N) = -\frac{2\pi}{s_a} \sum_{l'_3=1}^N \sum_{\kappa'=1}^N \xi_{\kappa'} |\vec{x}_1(l'_3, \kappa') - \vec{x}_{p1}|, \quad (19a)$$

where  $\xi_{\kappa'}$  is the fraction of the electronic charge attributed to ion  $\kappa'$ . At a point  $P'(\vec{x}_{p'})$  on the other side of the slab, the same term of the potential will be

$$V_c(x_{p'}, N) = -\frac{2\pi}{s_a} \sum_{l'_3=1}^N \sum_{\kappa'=1}^N \xi_{\kappa'} |\vec{x}_1(l'_3, \kappa') - \vec{x}_{p'1}|. \quad (19b)$$

Assuming  $|\vec{x}_{p1}| > |\vec{x}_1(l'_3, \kappa')|$  and  $\vec{x}_{p'} = -\vec{x}_p$ , we find for the constant potential difference

$$\begin{aligned} \Delta V_c(N) &= V_c(x_{p'}, N) - V_c(x_p, N) \\ &= -\frac{4\pi}{s_a} \sum_{l'_3=1}^N \sum_{\kappa'=1}^N \xi_{\kappa'} \vec{x}_1(l'_3, \kappa') \cdot \vec{v}_0. \end{aligned} \quad (20)$$

We note that the above expression is completely equivalent to the one given by Eq. (22) of paper I.

If we consider the slab as a part in the infinite crystal, the above potential difference is almost compensated by the result of the crystal, resulting in the regular potential distribution of the infinite structure. Instead, we will consider the slab free and an external potential to be applied, equal in magnitude and opposite in sign, to the one given by Eq. (20), which we assume to drop uniformly across the slab. The resulting potential distribution is illustrated in Fig. 1 for a slab of the zinc-blende structure, parallel to the  $(11\bar{1})$  direction, consisting of four layers.

In the general case where the unit cell may con-

tain many atoms we have to assume that these atoms are distributed over several parallel (*hkl*) planes. Let us denote the position vector of an atom lying on the first surface plane by  $\bar{x}(1, \kappa_1)$  and the position vector of an atom lying on the other surface plane of the slab by  $\bar{x}(N, \kappa_n)$ . Then its thickness will be given by

$$L = [\bar{x}(N, \kappa_n) - \bar{x}(1, \kappa_1)] \cdot \vec{v}_0. \quad (21)$$

Having applied the above-mentioned external potential, the total potential at ion site ( $l_3, \kappa$ ), apart from the fluctuating term already encountered in Eq. (6) for  $\bar{y} = \vec{0}$ , will be

$$V^i(l_3, \kappa) = -\frac{4\pi}{s_a} \sum_{l'_3=1}^{l_3} \sum_{\kappa'=1}^{\kappa} \xi_{\kappa'} [\bar{x}(l'_3, \kappa') - \bar{x}(1, \kappa_1)] \cdot \vec{v}_0 + \frac{4\pi}{s_a} \frac{[\bar{x}(l'_3, \kappa') - \bar{x}(1, \kappa_1)] \cdot \vec{v}_0}{[\bar{x}(N, \kappa_n) - \bar{x}(1, \kappa_1)] \cdot \vec{v}_0} \sum_{l'_3=1}^N \sum_{\kappa'=1}^N \xi_{\kappa'} \bar{x}(l'_3, \kappa') \cdot \vec{v}_0, \quad (22)$$

where the first sum extends over all ions of the unit cell from the first surface plane up to those ( $l_3, \kappa''$ ) lying on the same plane with ion ( $l_3, \kappa$ ). In Eq. (22) we assume, for reference, that the potential on the first surface plane is equal to zero.

The total electrostatic energy of the ions in a long unit cell of the slab, due to the above-described macroscopic potentials, will be

$$W^i = \frac{1}{2} \sum_{l_3=1}^N \sum_{\kappa=1}^N \xi_{\kappa} V^i(l_3, \kappa), \quad (23)$$

and the interaction force constant between the planes ( $l_3, \kappa$ ) and ( $l'_3, \kappa'$ ), due to their vibrations as solid planes, is given by

$$\Phi_{\alpha\beta}^{\text{mac}}(l_3, \kappa; l'_3, \kappa') = \frac{\partial^2 W^i}{\partial x_{\alpha}(l_3, \kappa) \partial x_{\beta}(l'_3, \kappa')}, \quad (24)$$

or, by using Eqs. (22) and (23) and taking the second derivative,

$$\Phi_{\alpha\beta}^{\text{mac}}(l_3, \kappa; l'_3, \kappa') = \frac{4\pi}{s_a L} \xi_{\kappa} \xi_{\kappa'} \cos\alpha \cos\beta + \Phi_{\alpha\beta}^{\text{surf}}(l_3, \kappa; l'_3, \kappa'), \quad (25a)$$

where

$$\Phi_{\alpha\beta}^{\text{surf}}(l_3, \kappa; l'_3, \kappa') = \frac{\Delta V_c(N)}{L^2} \left[ -(\delta_{l_3, 1} \delta_{\kappa\kappa_1} - \delta_{l_3, N} \delta_{\kappa\kappa_n}) \xi_{\kappa'} - (\delta_{l'_3, 1} \delta_{\kappa'\kappa_1} - \delta_{l'_3, N} \delta_{\kappa'\kappa_n}) \xi_{\kappa} \right. \\ \left. + \frac{\Delta V_c(N)}{L} (\delta_{l_3, 1} \delta_{\kappa\kappa_1} - \delta_{l_3, N} \delta_{\kappa\kappa_n}) (\delta_{l'_3, 1} \delta_{\kappa'\kappa_1} - \delta_{l'_3, N} \delta_{\kappa'\kappa_n}) \right] \cos\alpha \cos\beta \quad (25b)$$

and where  $\delta$ 's are Kronecker's  $\delta$ 's.

From Eqs. (25a) and (25b) it is evident that for a given slab there exists a constant long-range interaction between any pair of ion planes, depending on the thickness of the slab [first term in Eq. (25a)], plus an interaction between each surface plane and the rest of the slab. This latter interaction given by the term  $\Phi_{\alpha\beta}^{\text{surf}}(l_3, \kappa; l'_3, \kappa')$  in Eq. (25a) is a consequence of the change in the thickness of the slab due to vibrations of the surface planes.

We should note that the interaction between any pair of ion planes exists even if we consider the slab as a part of an infinite crystal and as we shall see below it gives an alternative for the calculation of the macroscopic field following a two-dimensional summation method. For a slab which consists, in part, of a different structure (e.g., heterostructure),

the interaction of Eq. (25a) has to be calculated on the basis of a more realistic assumption.

The total force on the ion plane ( $l_3, \kappa$ ) due to the displacements of all other ion planes is ( $\alpha$  component)

$$F_{\alpha}(l_3, \kappa) = - \sum_{l'_3, \kappa', \beta} \Phi_{\alpha\beta}^{\text{mac}}(l_3, \kappa; l'_3, \kappa') u_{\beta}(l'_3, \kappa') \quad (26a)$$

or

$$F_{\alpha}(l_3, \kappa) = -\frac{4\pi}{s_a L} \xi_{\kappa} \cos\alpha \sum_{l'_3, \kappa', \beta} \xi_{\kappa'} \cos\beta u_{\beta}(l'_3, \kappa') \\ - \sum_{l'_3, \kappa', \beta} \Phi_{\alpha\beta}^{\text{surf}}(l_3, \kappa; l'_3, \kappa') u_{\beta}(l'_3, \kappa'). \quad (26b)$$

To make a comparison with the three-dimensional case, we take the limit of  $F_{\alpha}(l_3, \kappa)$  for very thick slabs. We recall [Eq. (25) of paper I] that

$$L = (N-1)a_1 + d, \quad (27)$$

where  $a_1$  is the thickness of a one-unit-cell layer and  $d$  is the distance between the two outermost ion planes belonging to the same unit cell. For  $N \rightarrow \infty$  we can introduce the cyclic boundary condition, neglecting the deviations near the surfaces, and we can put

$$u_\alpha(l_3, \kappa) = u_\alpha(\kappa) \exp[-2\pi i \bar{y}_1 \cdot \bar{x}(l_3)], \quad (28a)$$

where  $\bar{y}_1$  is the wave vector perpendicular to the plane of the slab. Then for long-wavelength vibrations

$$\bar{y}_1 \rightarrow 0 \text{ and } u_\alpha(l_3, \kappa) \simeq u_\alpha(\kappa). \quad (28b)$$

Taking the limit of the first term in Eq. (26b) for  $N \rightarrow \infty$ , we get

$$\begin{aligned} \lim_{N \rightarrow \infty} F_\alpha(l_3, \kappa) &= F_\alpha(\kappa) \\ &= \lim_{N \rightarrow \infty} \left[ -\frac{4\pi}{s_a} \frac{N \cos \alpha}{(N-1)a_1 + d} \xi_\kappa \right. \\ &\quad \left. \times \sum_{\kappa'} \xi_{\kappa'} \bar{u}(\kappa') \cdot \bar{v}_0 \right] \quad (29) \end{aligned}$$

since the second term in Eq. (26b) tends obviously to zero, and finally

$$F_\alpha(\kappa) = -\frac{4\pi}{s_a} \cos \alpha \xi_\kappa \sum_{\kappa'} \bar{p}(\kappa') \cdot \bar{v}_0, \quad (30a)$$

where  $\bar{p}(\kappa')$  is the point dipole at ion site  $\kappa'$ .

Hence the total force on ion  $\kappa$  is

$$\bar{F}(\kappa) = \xi_\kappa \bar{E}^{\text{mac}}, \quad (30b)$$

where

$$\bar{E}^{\text{mac}} = -\frac{4\pi}{s_a} \bar{v}_0 \bar{v}_0 \cdot \sum_{\kappa} \bar{p}(\kappa). \quad (31)$$

The field of Eq. (31) is exactly the macroscopic field of Eq. (18) in the limit of zero wave vector from the direction perpendicular to the plane of the slab.

It is also possible to obtain a more general expression for the interaction constant between ion planes of the slab for wave vector  $\bar{y} \neq \bar{0}$ , in the same sense as in Eq. (25a), if necessary. This can be done by using the  $(h_1 h_2) = (00)$  term of Eq. (6) where the double differential and the sum over  $\beta$  is neglected,  $p_\beta(l_3, \kappa')$  is replaced by  $\xi_{\kappa'}$ , and a summation is performed over all  $(l_3, \kappa')$  in order to take an appropriate expression for the potential.

#### IV. DISCUSSION

We have calculated the Coulomb interaction in the case of ionic slabs of arbitrary orientation in any

structure. As far as interactions between plane lattices on different planes are concerned the infinite two-dimensional sums in direct space are converted into sums in reciprocal space only, which converge rapidly, depending on the distance of the plane lattices. In the case of a slab of the zinc-blende structure parallel to the  $(11\bar{1})$  plane, ten to twelve terms are needed for an accuracy of the order of  $10^{-6}$  (in units of  $e^2/v_a$ ) to calculate the interaction of the closest plane lattices, while three or four terms are enough to calculate the interaction of more distant planes. On the other hand, this interaction drops off very rapidly with the distance between the interacting planes, becoming about 8 orders of magnitude weaker for the fourth neighborhood, for zero wave vector, in the above example.

For interactions between plane lattices lying on the same plane, a two-dimensional version of the Ewald's method of summation is used. Comparing our results with the formulas given by Tong and Maradudin for NaCl we find that in case A, they are practically the same, while in case B they are different since Mackenzie's method sums both, in direct (over infinite ion lines) and reciprocal space (one-dimensional transform for each line). We consider the formulas given here as accurate and of easy and direct use in any case. We also note that the dependence of the interaction coefficients of Eq. (14) on the dividing point  $R$  is unimportant. A value of  $R$  equal to  $(\pi/s_a)^{1/2}$  is quite adequate without any further test.

Finally we should add that the given formulas for the interaction coefficients contain the macroscopic field. If, for instance, one uses the present formulas to calculate the Coulomb interaction in the usual single-cell approach of the infinite-crystal case, summing in direct space as implied, what will be obtained are the longitudinal solutions for the corresponding direction. A two-dimensional summation method, such as the present one, implies the presence of surfaces even at infinity, and does not separate out explicitly the macroscopic field. A slab of infinite thickness is not equivalent to an infinite crystal, since it presents an infinite potential difference between its two surfaces. Compensation of this potential results in a definite field. The variation of that field, due to vibrations of the parallel to the surface's ion planes, is the well-known macroscopic field responsible for the higher frequency of longitudinal modes in polar crystals. The calculation presented above shows how this field could be calculated in more complicated cases, such as the recently developed heterostructures.

\*Permanent address: First Laboratory of Physics, University of Thessaloniki, Thessaloniki, Greece.

<sup>1</sup>B. R. A. Nijboer and F. W. de Wette, *Physica (Utrecht)* **24**, 422 (1958).

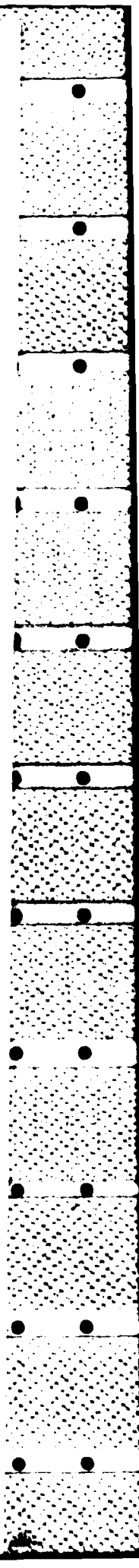
<sup>2</sup>F. W. de Wette and G. E. Schacher, *Phys. Rev.* **137**, A78 (1965).

<sup>3</sup>S. Y. Tong and A. A. Maradudin, *Phys. Rev.* **181**, 1318 (1969).

<sup>4</sup>V. V. Bryksin and Yu. A. Firsov, *Fiz. Tverd. Tela (Leningrad)* **11**, 2167 (1969) [*Sov. Phys.—Solid State* **11**, 1751 (1970)].

<sup>5</sup>W. E. Jones and R. Fuchs, *Phys. Rev. B* **4**, 3581 (1971).

<sup>6</sup>M. Born and K. Huang, *Dynamical Theory of Crystal Lattices* (Oxford University Press, New York, 1968), p. 253.



**Erratum: Lattice dynamics of thin ionic slabs. II. The long-range forces**  
**[Phys. Rev. B 28, 3398 (1983)]**

G. Kanellis, J. F. Morhange, and M. Balkanski

Please make the following changes to our paper.

- (1) Page 3399, in the first line of Eq. (6), instead of

$$\sum_{l_3, \kappa' \neq l_3, \kappa''} \sum_{\beta} \dots$$

write

$$\sum_{l_3, \kappa'} \sum_{\beta} \dots$$

- (2) Page 3400, in Eq. (9), do the same as above.

- (3) Page 3400, in the first line of Eq. (10), instead of

$$\frac{4\pi^2}{s_a} \sum_{h_1, h_2} \dots$$

write

$$\frac{4\pi^2}{s_a} \sum_{h_1, h_2} \dots$$

- (4) Page 3401, in Eq. (13), the quantity in the large parentheses must read

$$\left[ \sum_{\kappa''} p_{\beta}(l_3, \kappa'') Q_{\alpha\beta}(l_3, \kappa; l_3, \kappa'') \bar{Y} + p_{\beta}(l_3, \kappa) Q_{\alpha\beta}(l_3, \kappa; l_3, \kappa) \bar{Y} \right]$$

- (5) Page 3401, second line of Eq. (14), instead of

$$\frac{4\pi^2}{Rs_a}$$

write

$$\frac{4\pi^3}{Rs_a}$$

- (6) Page 3402, in Eqs. (19a), (19b), and (20), the sum over  $\kappa'$  runs from 1 to the number of ions in the unit cell (not to  $N$ ).

- (7) Page 3402, 10th line from the bottom of the right column, instead of ... by the result of the crystal ..., write ... by the rest of the crystal ...

- (8) Page 3403, in Eq. (22), delete  $N$  on the rightmost summation symbol (over  $\kappa'$ ).

- (9) Page 3403, in Eq. (23), delete  $N$  on the summation symbol over  $\kappa$ .

- (10) Page 3403, last two lines of the left column, instead of ... which consists, in part, of a ..., write ... which consists part of a ...

## Lattice dynamics of thin ionic slabs. III. Application to GaAs slabs

G. Kanellis,<sup>\*</sup> J. F. Morhange, and M. Balkanski*Laboratoire de Physique des Solides de l'Université Pierre et Marie Curie associé au Centre National de la Recherche Scientifique, 4 Place Jussieu, F-75230 Paris Cedex 05, France*

(Received 15 March 1982; revised manuscript received 11 March 1983)

The lattice vibrations of thin slabs (up to 25 layers) of GaAs are calculated for zero wave vector, on the basis of a rigid-ion model fitted on the phonon dispersion curves of the infinite crystal. It is shown that all the modes, except the surface ones, fall on the branches of the dispersion curves of the infinite crystal, while the surface modes seem to be combinations of those missing near the zone-edge modes. Comparison is made with former calculations and the influence of the short-range interaction near the surfaces and that of possible macroscopic fields is discussed.

## I. INTRODUCTION

Normal modes of vibrations of thin ionic slabs have been investigated theoretically by many authors,<sup>1-9</sup> mainly on the basis of a rigid-ion model, and the existence of surface modes have been well established. Jones and Fuchs<sup>7</sup> calculated the unretarded modes of a thin NaCl slab; they developed a theory for the infrared optical properties of ionic slabs and discussed previously published results on surface modes. Since most of the work mentioned above has been done on NaCl slabs a more substantial comparison is possible between their results. Benedek<sup>9</sup> calculated surface dispersion curves and phonon densities for thin ionic slabs on the basis of a breathing shell model using Green's-function formalism. This approach suitably extended proves to give very good results compared to those from direct calculations on thin slabs.

A very general approach to the effect of surfaces on the vibrational modes of crystalline solids is given by Feuchtwang<sup>10</sup> based on the assumption of finite-range interaction. Although in ionic crystals long-range electrostatic interaction is important, infinite-range forces arise only in the presence of a macroscopic field. Hence his results must be, in general, valid. Different features may appear to apply only to modes depending strongly on forces due to such fields. The influence of a macroscopic field on the vibrational modes of a slab will be discussed briefly in the last paragraph of Sec. IV.

Dispersion relations for surface modes are given by Fuchs and Kliewer<sup>1</sup> who found all long-wavelength optical modes of an ionic slab to have either TO or LO frequencies. Tong and Maradudin<sup>3</sup> treated in detail the case of a NaCl slab parallel to

the (100) plane and pointed out the importance of some approximations made in the former work. Further comments on this point are given by Jones and Fuchs.<sup>7</sup> We also found the proper description of the short-range interaction between atoms near the surface to be of fundamental importance in calculating the correct frequencies of the surface modes.

Among the considerable experimental works on infrared absorption or Raman scattering on thin films and powders, which show vibrational states either between the TO and LO frequencies of the infinite crystal or below the TO frequency, we mention the infrared transmission and reflection measurements on thin (up to 68  $\mu\text{m}$ ) films on GaAs by Cochran *et al.*<sup>11</sup> and Fray *et al.*<sup>12</sup> They observed in a 25  $\mu\text{m}$  thin film, lattice absorption on the TO and LO frequencies and also two other strong peaks on frequencies lying between these two. Each of those peaks seems to consist of three or four fine-structure peaks. These features are attributed to the size, shape, and orientation of the specimens used.

Raman spectra on laser-annealed GaAs (Ref. 13) show a gradual transition from the amorphous spectrum to the crystalline one involving a continuous variation of degree of order versus the annealing density energy. The above experimental results and also analogous results on other materials reveal the need for a complete calculation of infrared and Raman spectra of small crystallites in order to justify the hypothesis of size effects.

In the present paper we report on calculations of vibrational modes of thin GaAs slabs parallel to (11 $\bar{1}$ ) planes, on the basis of a rigid-ion model. This model has been used by Kunc<sup>14</sup> to fit measured phonon dispersion curves, hence our results are directly

comparable to the ones of an infinite crystal. The long-range interaction has been calculated in a former paper<sup>15</sup> referred to as paper II.

In the next section we briefly review the equations of motion and the resulting dynamical matrix to be solved. In the third section we describe in short the rigid-ion model used for the calculation and the procedure applied to calculate the short-range interaction of atoms lying near the surfaces. Finally, in the last section we describe the results obtained and we discuss them in comparison with other results.

## II. EQUATIONS OF MOTION AND DYNAMICAL MATRIX

We consider a crystal slab of zinc-blende structure (particularly GaAs) parallel to the (111) plane. Choosing a Cartesian coordinate system  $Ox_1x_2x_3$ , whose axes are parallel to the edges of the cubic fcc unit cell and its origin on an ion site (for instance, a Ga site), the primitive translation vectors are

$$\begin{pmatrix} \bar{a}_1 \\ \bar{a}_2 \\ \bar{a}_3 \end{pmatrix} = \frac{a}{2} \begin{pmatrix} 0 & 1 & 1 \\ 1 & 0 & 1 \\ 1 & 1 & 0 \end{pmatrix} \begin{pmatrix} \bar{x}_{01} \\ \bar{x}_{02} \\ \bar{x}_{03} \end{pmatrix}, \quad (1)$$

where  $a$  is the lattice constant. Vectors  $\bar{a}_1$  and  $\bar{a}_2$  lie on the plane (111) while  $\bar{a}_3$  lies out of it.

The equations of motion for a lattice are<sup>16</sup>

$$m_\kappa \ddot{u}_\alpha(l, \kappa) = - \sum_{l', \kappa'} \sum_{\beta} \phi_{\alpha\beta}(l, \kappa; l', \kappa') u_\beta(l', \kappa'), \quad (2)$$

where  $m_\kappa$  is the mass of the  $\kappa$ th kind of ion,  $u_\alpha(l, \kappa)$  is the  $\alpha$ th Cartesian component of the displacement from the equilibrium position,  $\phi_{\alpha\beta}(l, \kappa; l', \kappa')$  are the atomic force constants, and  $l = (l_1, l_2, l_3)$  labels the unit cells.

Applying cyclic boundary conditions along the directions  $\bar{a}_1$  and  $\bar{a}_2$  [on the infinite (111) plane] we put

$$u_\alpha(l, \kappa) = \frac{v_\alpha(l_3, \kappa)}{m_\kappa^{1/2}} \exp[-i\omega t + 2\pi i \bar{y} \cdot \bar{x}(l, \kappa)], \quad (3)$$

where  $\bar{y}$  is a two-dimensional wave vector. Equation (2) becomes

$$\omega^2 v_\alpha(l_3, \kappa) = \sum_{l'_3, \kappa'} \sum_{\beta} D_{\alpha\beta}(l_3, \kappa; l'_3, \kappa' | \bar{y}) v_\beta(l'_3, \kappa'), \quad (4)$$

where

$$D_{\alpha\beta}(l_3, \kappa; l'_3, \kappa' | \bar{y}) = \sum_{l''_1, l''_2} \frac{\phi_{\alpha\beta}(l, \kappa; l'', \kappa')}{(m_\kappa m_{\kappa'})^{1/2}} \times \exp[2\pi i \bar{y} \cdot \bar{x}(l, \kappa; l'', \kappa')] \quad (5)$$

are the elements of the  $6N \times 6N$  dynamical matrix ( $N$  is the number of layers in the slab). Since no periodic boundary condition is used along the finite dimension, any further reduction of the dynamical matrix will be likely possible only from symmetry considerations.

It has been shown<sup>17</sup> that for the above chosen orientation of the slab one can use a new coordinate system  $Ox'_1x'_2x'_3$ , related to the old one associated with the crystallographic unit cell, by the transformation

$$\begin{pmatrix} \bar{x}'_{01} \\ \bar{x}'_{02} \\ \bar{x}'_{03} \end{pmatrix} = \frac{1}{\sqrt{6}} \begin{pmatrix} -\sqrt{3} & \sqrt{3} & 0 \\ 1 & 1 & 2 \\ \sqrt{2} & \sqrt{2} & -\sqrt{2} \end{pmatrix} \begin{pmatrix} \bar{x}_{01} \\ \bar{x}_{02} \\ \bar{x}_{03} \end{pmatrix}, \quad (6)$$

whose  $Ox'_1$  and  $Ox'_2$  axes are coplanar with the slab, while axis  $Ox'_3$  is perpendicular to it. Since it is always possible to find such a coordinate system, whatever the orientation of the slab might be, let us denote the corresponding transformation matrix by  $H$  [in the present case  $H$  is the  $3 \times 3$  unitary matrix used in Eq. (6)].

With the use of transformation  $H$  and the representation of the space group  $G$  of the three-dimensional structure with respect to the old coordinate system, one can construct a new space group  $G'$  appropriate for the two-dimensional structure of the slab, by transforming the representation of  $G$  to the new coordinate system and by picking up those elements which act only parallel to the plane of the slab.

Group  $G'$  can then be used to provide the form of the force-constant matrices and the relations between the elements of the dynamical matrix. In the present case and for wave vector  $\bar{y} = \bar{0}$ , we find that the interaction between the plane lattices assumes the general form

$$D(l_3, \kappa; l'_3, \kappa') = \begin{pmatrix} A & B & -B \\ B & A & -B \\ -B & -B & A \end{pmatrix} \quad (7)$$

in the old coordinate system  $Ox_1x_2x_3$ , while in the system  $Ox'_1x'_2x'_3$  it takes the form

$$D'(l_3, \kappa; l'_3, \kappa') = \begin{pmatrix} A - B & 0 & 0 \\ 0 & A - B & 0 \\ 0 & 0 & A + 2B \end{pmatrix} \quad (8)$$

through the transformation

$$\underline{D}'(l_3, \kappa; l_3', \kappa') = \underline{H} \underline{D}(l_3, \kappa; l_3', \kappa') \underline{H}^{-1} \quad (9)$$

The form of Eq. (8) implies that for the so-chosen orientation of the slab, the solutions of Eq. (4) fall into two groups, one doubly degenerate consisting of the in-plane solutions ( $x$ - $y$  modes) and one nondegenerate consisting of the out-of-plane solutions ( $z$  modes).

The matrix whose elements are defined by Eq. (5) expresses the interaction between plane lattices and has to be calculated on the basis of some model. In the next section we give a brief description of the applied rigid-ion model. Since both short- and long-range forces are taken into account, it is customary to consider the dynamical matrix as consisting of two parts, the short-range (sr) and the Coulomb parts;

$$\underline{D}(l_3, \kappa; l_3', \kappa') = \underline{D}^{sr}(l_3, \kappa; l_3', \kappa') + \underline{D}^C(l_3, \kappa; l_3', \kappa') \quad (10)$$

The form of the interaction matrices between the plane lattices of the slab for zero wave vector, is given in the Appendix.

The Coulomb part can be expressed in terms of the  $Q$  coefficients calculated in paper II [Eqs. (10) and (14)], and for the general wave vector it assumes the form

$$\begin{aligned} D_{\alpha\beta}^C(l_3, \kappa; l_3', \kappa' | \vec{y}) &= \delta_{l_3, l_3'} \delta_{\kappa, \kappa'} \frac{\xi_\kappa}{m_\kappa} \\ &\times \sum_{l_3'', \kappa''} \xi_{\kappa''} Q_{\alpha\beta}(l_3, \kappa; l_3'', \kappa'' | \vec{0}) \\ &- \frac{\xi_\kappa \xi_{\kappa'}}{(m_\kappa m_{\kappa'})^{1/2}} Q_{\alpha\beta}(l_3, \kappa; l_3', \kappa' | \vec{y}), \end{aligned} \quad (11)$$

where  $\xi_\kappa$  is the charge fraction attributed to ion  $\kappa$ . Values of the  $Q$  coefficients for zero wave vector are also given in the Appendix (Table I).

TABLE I. Values of the Coulomb coefficient  $\beta$  [in units of  $(Ze)^2/v\mu$ ].

$\kappa$	$\kappa'$	$l'$	$\beta$
1	2	0	5.59135
1	1	1	-0.14341
1	2	1	0.03349
2	1	1	1.43762
2	2	1	-0.14341
1	1	2	-0.00040
1	2	2	0.00018
2	1	2	-0.00175
2	2	2	-0.00040

### III. THE MODEL

In the present case we use the rigid-ion model (RIM) developed and applied to several binary compounds of the zinc-blende structure by Kunc.<sup>14</sup> Apart from the effective charge  $q^*$  the model parameters are ten tensorial force constants,  $A$  and  $B$  for first-neighbor central and noncentral interaction,  $C_1$ ,  $D_1$ ,  $E_1$ ,  $F_1$ ,  $C_2$ ,  $D_2$ ,  $E_2$ , and  $F_2$ , for second-neighbor central and noncentral interaction, for the two different kinds of ions.

All of the above parameters have been fitted to experimentally known phonon dispersion curves, the elastic constants, and the piezoelectric constant. In order to use the above model in the case of a slab the following adaptations have to be made:

(a) Long-range forces have to be recalculated on the basis of new suitable formulas as already mentioned.

(b) Short-range interaction of the near-the-surface atoms has to be modified, so as to take the missing ions into account. For the short-range part of the dynamical matrix the following procedure has been followed. From the ten fitted tensorial force constants, the values of a set of ten valence force field (VFF) force constants are deduced, namely the  $\xi$ ,  $\lambda$ ,  $\rho$ ,  $\mu$ ,  $\sigma$ ,  $\nu$ ,  $k_\theta$ ,  $k'_\theta$ ,  $k_{rr}$ , and  $k'_{rr}$  according to the following model for the potential energy:

$$\begin{aligned} \Phi &= r_0 \xi \sum_{\text{Ga-As}} \Delta r_{ij} + \frac{\lambda}{2} \sum_{\text{Ga-As}} (\Delta r_{ij})^2 + r_1 \rho \sum_{\text{Ga-Ga}} \Delta r_{ik} + \frac{\mu}{2} \sum_{\text{Ga-Ga}} (\Delta r_{ik})^2 + r_1 \sigma \sum_{\text{As-As}} \Delta r_{jl} + \frac{\nu}{2} \sum_{\text{As-As}} (\Delta r_{jl})^2 \\ &+ \frac{k_\theta r_0^2}{2} \sum_{\text{As-Ga-As}} (\Delta \theta_{jll})^2 + \frac{k'_\theta r_0^2}{2} \sum_{\text{Ga-As-Ga}} (\Delta \theta_{ijk})^2 + \frac{k_{rr}}{2} \sum_{\text{As-Ga-As}} \Delta r_{ji} \Delta r_{il} + \frac{k'_{rr}}{2} \sum_{\text{Ga-As-Ga}} \Delta r_{ij} \Delta r_{jk}, \end{aligned} \quad (12)$$

where  $r_0$  and  $r_1$  are the first- and second-nearest-neighbor distances, respectively.

The interaction of the near-the-surface ions is calculated on the basis of the above VFF model. It

should be noted that the ten VFF parameters are not independent, but have to fulfill the equilibrium condition. For the given values of the tensorial force constants this condition does not hold. Hence we

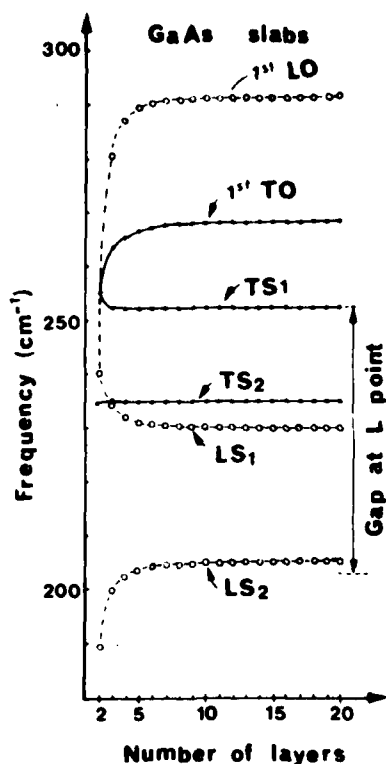


FIG. 1. Variation of the frequencies of six modes vs the thickness of the slab.

decompose the tensorial force constants into the VFF parameters disregarding this condition.

By so doing, only the interaction of atoms lying near the surfaces may be influenced. Since the correct description of the above interaction is of critical importance in calculating the surface mode frequencies, one needs a faithful VFF model in order to obtain unambiguous results for these modes. In the next section we comment on the results based on the above consideration and on those obtained when the short-range interaction of surface atoms is considered to be the same as for atoms in the interior of the slab.

#### IV. RESULTS AND DISCUSSION

We have calculated the frequencies and the eigenvectors for thin slabs of GaAs oriented parallel to the (111) plane with thicknesses from 2 up to 25 cells (10–130 Å thick) for zero (two-dimensional) wave vector.

The main feature displayed by the solutions is that, by increasing the number of layers of the slab (i.e., its thickness) all of the solutions tend rapidly to certain limits, while the new solutions appearing in

each thicker slab are interpolated between the solutions of the thinner one. For a slab 20 layers thick all the frequencies are within 1% of their limits.

In Fig. 1 we show the variation of the frequencies of six modes versus the thickness of the slabs: the highest-frequency  $z$  mode (first LO), the highest-frequency  $x$ - $y$  mode (first TO), and four surface modes, i.e., two surface  $x$ - $y$  modes (TS1 and TS2) and two surface  $z$  modes (LS1 and LS2). We see that the surface modes TS1 and TS2 have practically constant frequency for any slab as thin as three layers, while the frequencies of the rest of the modes tend very rapidly to their limiting values.

The two-dimensional Brillouin zone corresponding to the slab structure is a section through the center of the three-dimensional zone of the fcc lattice, perpendicular to the  $\Lambda$  direction  $(-\xi, -\xi, \xi)$ . Comparing the frequencies of the above modes with the frequencies of the modes belonging to the dispersion branches of the  $\Lambda$  direction of the infinite crystal, we find that the first LO and first TO modes tend to have frequencies equal to those of the LO and TO modes of the  $\Gamma$  point of the infinite structure, respectively. The surface mode TS1 has a frequency almost equal to the TO mode at the  $L$  point, while modes TS2, LS1, and LS2 have frequencies which fall into the gap at the  $L$  point of the infinite crystal.

Before making any further comments on the surface modes and on the rest of the modes, we will turn our attention to the eigenvectors. For a GaAs slab  $N$  layers thick, there are  $2N$   $x$ - $y$  modes, which are doubly degenerate (the transverse modes), and  $2N$   $z$  modes (the longitudinal ones). From the  $2N$  modes in each configuration,  $N$  are optical and the remaining  $N$  are acoustic. Among the  $N$  optical modes in each case there are two whose amplitudes decay exponentially along the finite dimension of the slab, from the one surface to the other, and are therefore called surface modes. For wave vectors different from zero the so-called Rayleigh waves<sup>16</sup> appear, among the acoustic modes. For each optic mode  $m$  we construct the difference of the reduced displacements,

$$f_m^{\text{op}}(l_3) = \frac{u(l_3, 1 | m)}{\sqrt{M_1}} - \frac{u(l_3, 2 | m)}{\sqrt{M_2}}, \quad (13)$$

where 1 denotes the Ga atom, 2 the As atom,  $l_3$  numbers the layers of the slab, and  $M$  is the mass. Accordingly, for the acoustic modes, we construct the sum of the same quantities.

$$f_m^{\text{ac}}(l_3) = \frac{u(l_3, 1 | m)}{\sqrt{M_1}} + \frac{u(l_3, 2 | m)}{\sqrt{M_2}}. \quad (14)$$

In Fig. 2 we plot  $f_m^{\text{op}}(l_3)$  and  $f_m^{\text{ac}}(l_3)$  vs  $z = l_3 a_1$ ,

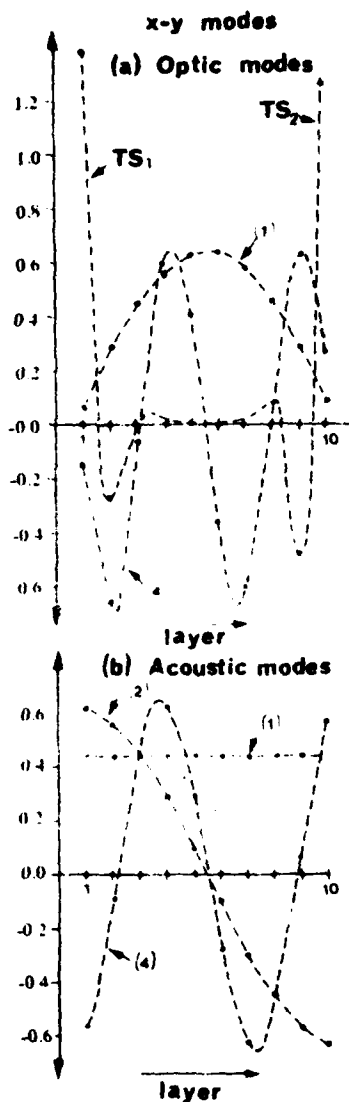


FIG. 2. For a slab of ten layers: (a) Relative reduced ionic displacements for some x-y optic modes. Numbering starts with the mode of highest frequency. (b) Sum of reduced ionic displacements for some x-y acoustic modes. Numbering starts with the zero-frequency mode.

the coordinate along the finite dimension of the slab, for some x-y modes (transverse modes), and in Fig. 3 we plot the same functions for some z modes (longitudinal). It is evident from these figures that all the optic modes, except the surface ones, can almost be described (neglecting the sign) as

$$f_m^{op}(z) \approx \frac{2}{\sqrt{N}} \sin \frac{m\pi z}{L}, \quad (15)$$

where  $L$  is the thickness of the slab, while the acoustic modes can be described as

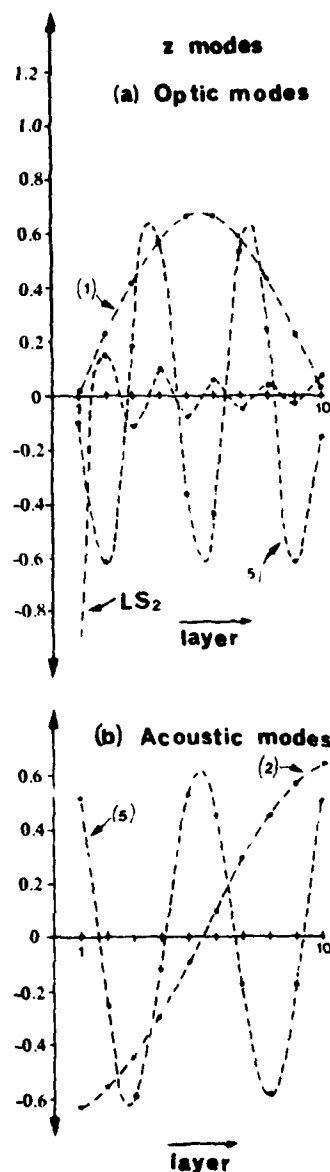


FIG. 3. For a slab of ten layers: (a) Relative reduced ionic displacements for some z optic modes. Numbering starts with the mode of highest frequency. (b) Some of reduced ionic displacements for some z acoustic modes. Numbering starts with the zero-frequency mode.

$$f_m^{ac}(z) \approx \frac{2}{\sqrt{N}} \cos \frac{(m-1)\pi z}{L} \quad (16)$$

( $m = 1, 2, \dots, N$ , numbers the optic modes starting from the highest-frequency one and the acoustic modes starting from the zero-frequency one).

We note that the above simple trigonometric expressions do not describe exactly the functions of the displacement defined by Eqs. (13) and (12), but rath-

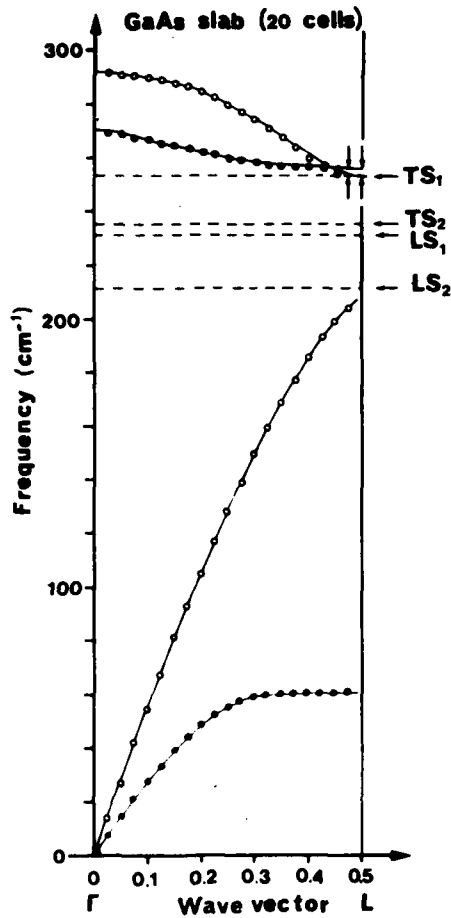


FIG. 4. Phonon dispersion curves of GaAs along the  $A$  direction (solid lines).  $x$ - $y$  modes (solid circles) and  $z$  modes (open circles) for a slab of 20 layers thick. Broken lines show the position of surface modes. The positions of TO and LO missing modes near and on the zone boundary are shown by arrows.

er, give a good picture of what these functions look like. Moreover, although the functions sketched in Figs. 2 and 3 refer to a slab ten layers thick, the picture is the same for slabs of any thickness.

From Eqs. (15) and (16) we see that there is an implicit dependence of the modes on a wave vector along the finite dimension of the slab, although such an assumption has not been made. All the modes, except the surface ones, on which we will comment later on, seem to be characterized by the values of a wave vector

$$z = n \frac{\pi}{L} \quad (17)$$

There is no optic mode with  $n=0$ , i.e., there is no mode of infinite wavelength. Since the surface

modes cannot be described by the same function  $f_m^{op}$ , only  $N-2$  optic modes could be attributed to the wave vectors of Eq. (17). On the other hand, all the  $N$  acoustic modes can be regarded as corresponding to some wave vector  $y_z$ . We should note that the solution of zero frequency for  $y_z=0$  has been imposed by using relation (A5) when calculating the self-terms of the dynamical matrix.

According to the above observations, we plot in Fig. 4 the dispersion curves of GaAs along the  $A$  direction, as they have been calculated by Kunc<sup>14</sup> on the basis of the same model and we put on the same graph the solutions for a slab 20 layers thick. We have chosen this thickness where each solution has reached its limit within less than 1%. Acoustic modes start from zero wave vector, while optic modes start from wave vector equal to  $0.5/20$ . We see that all the modes, except the surface ones, fall on the corresponding branches:  $x$ - $y$  modes on the transverse branches and  $z$  modes on the longitudinal ones. There are four optic modes missing. Instead there are four surface modes shown by dotted lines on the graph along the zonewidth, although they seem to belong to a value of the wave vector very close to the zone boundary. Hence we conclude that the surface modes could be regarded as superpositions of the missing optical modes, and perhaps the corresponding acoustic modes of the zone edge, in each configuration (transverse or longitudinal). The longitudinal surface modes ( $z$  modes), considered as being superpositions of modes of higher frequency, appear to have lower frequencies than the transverse ones. They also show considerably less decay along the finite dimension of the slab. Both of these features could be explained, qualitatively at the moment, by the weaker short-range forces near the surfaces and by the assumption that these modes are strongly damped by the long-range forces. We should note at this point that the slowest convergence of the frequencies to their limiting values, with increasing thickness of the slab, is observed for the longitudinal modes of shorter wavelength (wave vector near the zone edge). Indeed, the frequencies of the surface modes depend very strongly on the short-range forces assumed for the surface layers. If we restore on these layers the same short-range forces as for the rest of the slab, then all the modes, except the surface ones, tend faster to the same limiting frequencies. The surface modes have higher limits as follows: The TS1 mode,  $253.3 \text{ cm}^{-1}$  (instead of  $252.5 \text{ cm}^{-1}$ ), the TS2 mode,  $247.3 \text{ cm}^{-1}$  (instead of  $235 \text{ cm}^{-1}$ ), the LS1 mode,  $250.7 \text{ cm}^{-1}$  (instead of  $230.7 \text{ cm}^{-1}$ ), and the LS2 mode,  $249.6 \text{ cm}^{-1}$  (instead of  $210.5 \text{ cm}^{-1}$ ). We see that the longitudinal surface modes have a much stronger dependence on the short-range forces assumed for the sur-

face layers, but still at least one of them should have higher frequency than the transverse modes if no damping due to long-range forces was existing. Hence the correct description of the short-range forces near the surfaces is of critical importance in calculating the surface mode frequencies. Of course, the eigenvectors are also influenced by the change of the forces near the surface, in particular the eigenvectors of the longitudinal modes, but they retain their main features. Stronger forces between the surface layers result in deeper penetration of those modes in the slab.

On the basis of the above observations it is clear that the continuum of frequencies for "bulk" modes obtained by several authors when calculating solutions for different wave vectors on the plane of a slab, is the projection of the dispersion surfaces of the infinite crystal on the two-dimensional Brillouin zone appropriate for the slab. Comparing our results with those of Tong and Maradudin,<sup>3</sup> who calculated the solutions for a slab of NaCl parallel to (001) plane, we could note the following: The frequency of the transverse surface mode in NaCl, lying just below the lower limit of the "bulk" optical modes, is in agreement with our results. The near degeneracy of both pairs of surface modes they found can be explained by the fact that the two surfaces of the NaCl slab in the above orientation are completely equivalent. Moreover, the thickness of this slab is an integer multiple of the lattice constant, while in our case it is not. This feature may be of importance when superimposing plane waves, due to the phase difference it may introduce. As far as it concerns the higher-frequency surface modes for zero wave vector in the case of the NaCl slab, they can be considered as unlocalized surface modes whose wave vector perpendicular to the plane of the slab can assume values either at the center or at the zone boundary<sup>10</sup> in the present case. The corresponding modes in our case are of the same type as those found by Wallis.<sup>18</sup> This difference may be due to the fact that the NaCl slab consists of identical "neutral" planes.

Fuchs and Kliewer<sup>1</sup> treated the case of long-wave optical vibrations in a slab in the electrostatic approximation. Apart from the influence on their results due to approximations concerning the short-range forces near the surfaces and the replacement of infinite sums by integrals, which have been dis-

cussed by Tong and Maradudin,<sup>3</sup> we would like to note that their results for "bulk" modes concern those modes which lie on the corresponding branches but very near to the  $\Gamma$  point. Hence for a thick slab there are many modes which have the zone-center TO and LO frequencies with small wave vectors  $m\pi/L$ . For optic modes we have found only the sine dependence of the displacements with odd and even values of  $m$ . Their point, that this dependence is such that there are exactly  $m$  half waves across the thickness of the slab, is correct even for very thin slabs and for the acoustic modes also. The quantization of the wave vector along the finite dimension is of course the same for all dispersion branches.

The surface modes found by these authors reduce, for zero wave vector on the plane of the slab, in unlocalized surface modes, corresponding to zone-center modes of the infinite crystal. It has been shown by Feuchtwang<sup>10</sup> that these modes are a special case of bulk modes. Since the above authors treated the case of long waves, these modes may be the only ones which, for finite wave vectors ( $\neq 0$ ) on the plane of the slab, became surface modes. Lucas<sup>4</sup> and Jones and Fuchs<sup>7</sup> attribute the above behavior of these modes to the neglect of the changes of the forces acting on atoms near the surfaces. The results of the latter author at  $\vec{y} = \vec{0}$  are in agreement to those of Lucas, and Tong and Maradudin, as to the number and type of surface modes.

A final remark concerns the possible influence of macroscopic fields. We have shown in paper II that vibrations involving ionic displacements perpendicular to the plane of the slab give rise to a potential difference between its two surfaces. This potential does not influence the vibrations of a free slab, except if it results in additional surface charges, or if the slab is considered in some polarizable environment. In such cases, assuming complete compensation of the above potential, all the frequencies of the  $z$  modes tend slower to the same limits, while an additional phase difference is introduced in the displacements of atoms in neighboring cells. This phase difference moves all the optic modes one step toward the zone boundary. Hence for a slab thicker than ten layers, the relative displacements show the same pattern as described by Eq. (15), but now modes with  $m = 0$ ,  $m = 1$ , and  $m = N - 1$  are missing.

#### APPENDIX

The form of force-constant matrices (interaction between individual ions) for the zinc-blende structure is the following:

$$\Phi(l,1;l,2) = \begin{pmatrix} A & B & B \\ B & A & B \\ B & B & A \end{pmatrix}, \quad \Phi(l,2;l',1) = \begin{pmatrix} A & B & -B \\ B & A & -B \\ -B & -B & A \end{pmatrix}, \quad (\text{A1})$$

$$\Phi(l,1;l',1) = \begin{pmatrix} C_1 & D_1 & E_1 \\ D_1 & C_1 & E_1 \\ -E_1 & -E_1 & F_1 \end{pmatrix}, \quad \Phi(l,2;l',2) = \begin{pmatrix} C_2 & D_2 & E_2 \\ D_2 & C_2 & E_2 \\ -E_2 & -E_2 & F_2 \end{pmatrix},$$

where  $l = (l_1, l_2, l_3)$  and  $l' = (l_1, l_2, l_3 + 1)$ .

For the surface layers  $l_0 = (l_1, l_2, 1)$  and  $l_N = (l_1, l_2, N)$  the force-constant matrices in the present case take the form

$$\Phi(l_0,1;l_0,2) = \begin{pmatrix} A_1 & B_1 & B_1 \\ B_1 & A_1 & B_1 \\ B_2 & B_2 & A_2 \end{pmatrix}, \quad \Phi(l_N,1;l_N,2) = \begin{pmatrix} A_3 & B_3 & B_4 \\ B_3 & A_3 & B_4 \\ B_3 & B_3 & A_5 \end{pmatrix}. \quad (\text{A2})$$

The decomposition of the tensorial force constants into parameters of the VFF model used can be found in Ref. 14 for all interactions, except the ones between ions in the surface layers, which are listed below:

$$A_1 = A - k_{rr}/6, \quad A_2 = A + 4k_\theta/3 + k_{rr}/6, \quad A_3 = A - k'_{rr}/6, \quad A_4 = 4k'_\theta/3 + k'_{rr}/6, \quad (\text{A3})$$

$$B_1 = B - k_{rr}/6, \quad B_2 = B - 2k_\theta/3 + k_{rr}/6, \quad B_3 = B - k'_{rr}/6, \quad B_4 = B - 2k'_\theta/3 + k'_{rr}/6.$$

The interaction matrices for plane lattices for zero wave vector (submatrices of the dynamical matrix) assume the following forms (with  $l'_3 = l_3 + 1$ ):

$$\underline{D}(l_3,1;l_3,2) \sim \begin{pmatrix} 3A & -B & B \\ -B & 3A & B \\ B & B & 3A \end{pmatrix}, \quad \underline{D}(l_3,2;l'_3,1) \sim \begin{pmatrix} A & B & -B \\ B & A & -B \\ -B & -B & A \end{pmatrix}, \quad (\text{A4a})$$

$$\underline{D}(l_3,1;l'_3,1) \sim \begin{pmatrix} 2C_1 + F_1 & D_1 & -D_1 \\ D_1 & 2C_1 + F_1 & -D_1 \\ -D_1 & -D_1 & 2C_1 + F_1 \end{pmatrix}, \quad \underline{D}(l_3,2;l'_3,2) \sim \begin{pmatrix} 2C_2 + F_2 & D_2 & -D_2 \\ D_2 & 2C_2 + F_2 & -D_2 \\ -D_2 & -D_2 & 2C_2 + F_2 \end{pmatrix}. \quad (\text{A4b})$$

Self terms, for zero wave vector, are calculated on the basis of the equation<sup>16</sup>

$$\sum_{l',\kappa'} \Phi_{\alpha\beta}(l\kappa;l'\kappa') = 0. \quad (\text{A5})$$

The corresponding interaction matrices for planes of the surface layers ( $l_3 = 1$  and  $l_3 = N$ ) take the form

$$\underline{D}(1,1;1,2) \sim \begin{pmatrix} 2A_1 + A_2 & -B_2 & B_2 \\ -B_2 & 2A_1 + A_2 & B_2 \\ B_2 & B_2 & 2A_1 + A_2 \end{pmatrix}, \quad \underline{D}(N,1;N,2) \sim \begin{pmatrix} 2A_3 + A_4 & -B_4 & B_4 \\ -B_4 & 2A_3 + A_4 & B_4 \\ B_4 & B_4 & 2A_3 + A_4 \end{pmatrix}. \quad (\text{A6})$$

All the Coulomb interaction matrices assume for zero wave vector the form

$$\underline{Q}(0,\kappa;l',\kappa') = \begin{pmatrix} 0 & \beta & -\beta \\ \beta & 0 & -\beta \\ -\beta & -\beta & 0 \end{pmatrix}. \quad (\text{A7})$$

The values of  $\beta$  are given in Table I for  $l' = 0, 1$ , and 2. All more distant interactions are less than  $10^{-5}$  [in units of  $(Ze)^2/v_a$ ].

- \*Permanent address: First Laboratory of Physics, University of Thessaloniki, Thessaloniki, Greece.
- <sup>1</sup>R. Fuchs and K. L. Kliewer, *Phys. Rev.* **140**, A2076 (1965).
  - <sup>2</sup>R. Englman and R. Ruppin, *J. Phys. C* **1**, 614 (1967).
  - <sup>3</sup>S. Y. Tong and A. A. Maradudin, *Phys. Rev.* **181**, 1518 (1968).
  - <sup>4</sup>A. A. Lucas, *J. Chem. Phys.* **48**, 3156 (1968).
  - <sup>5</sup>V. V. Bruksin and Yu. A. Firsov, *Fiz. Tverd. Tela (Leningrad)* **11**, 2167 (1969) [*Sov. Phys.—Solid State* **11**, 1751 (1970)].
  - <sup>6</sup>R. E. Allen, G. P. Alldredge, and F. W. de Wette, *Phys. Rev. B* **4**, 1648 (1971).
  - <sup>7</sup>W. E. Jones and R. Fuchs, *Phys. Rev. B* **4**, 3581 (1971).
  - <sup>8</sup>W. E. W. Ludwig, *Jpn. J. Appl. Phys. Suppl.* **2**, 879 (1974).
  - <sup>9</sup>G. Benedek, *Sarf. Sci.* **61**, 603 (1974).
  - <sup>10</sup>T. E. Feuchtwang, *Phys. Rev.* **152**, 731 (1967).
  - <sup>11</sup>W. Cochran, S. J. Fray, F. A. Johnson, J. E. Quarrington, and N. Williams, *J. Appl. Phys. Suppl.* **32**, 2102 (1961).
  - <sup>12</sup>S. J. Fray, F. A. Johnson, J. E. Quarrington, and N. Williams, *Proc. Phys. Soc. London* **77**, 215 (1961).
  - <sup>13</sup>J. F. Morhange, G. Kanelis, and M. Balkanski, *J. Phys. Soc. Jpn. Suppl. A* **49**, 1295 (1980).
  - <sup>14</sup>K. Kunc, *Ann. Phys. (Paris)* **8**, 319 (1973-74).
  - <sup>15</sup>G. Kanelis, J. F. Morhange, and M. Balkanski, preceding paper, *Phys. Rev. B* **28**, 3398 (1983).
  - <sup>16</sup>A. A. Maradudin, E. W. Montroll, G. H. Weiss, and I. P. Ipatova, *Theory of Lattice Dynamics in the Harmonic Approximation*, Supplement 3 of *Solid State Physics* (Academic, New York, 1971).
  - <sup>17</sup>G. Kanelis, J-F. Morhange, and M. Balkanski, *Phys. Rev. B* **21**, 1543 (1980).
  - <sup>18</sup>R. F. Wallis, *Phys. Rev.* **105**, 540 (1957).

Erratum: Lattice dynamics of thin ionic slabs. III. Application to GaAs slabs  
[Phys. Rev. B 28, 3406 (1983)]

G. Kanellis, J. F. Morhange, and M. Balkanski

Please make the following changes to our paper.

(1) Page 3413, in Eq. (A2), instead of

$$\underline{\Phi}(l_N, 1; l_N, 2) = \begin{pmatrix} A_3 B_3 B_4 \\ B_3 A_3 B_4 \\ B_3 B_3 A_3 \end{pmatrix} .$$

write

$$\underline{\Phi}(l_N, 1; l_N, 2) = \begin{pmatrix} A_3 B_3 B_4 \\ B_3 A_3 B_4 \\ B_3 B_3 A_4 \end{pmatrix} .$$

(2) Page 3413, in Eq. (A3), instead of

$$4_s = 4k_\theta/3 + \lambda_{\mu\mu}^2/6 .$$

write

$$4_s = 4k_\theta/3 + \lambda_{\mu\mu}^2/6 + A$$

Anharmonic effects in light scattering due to optical phonons in silicon

M. Balkanski, R. F. Wallis,\* and E. Haro

Laboratoire de Physique des Solides, associé au Centre National de la Recherche Scientifique,  
 Université Pierre et Marie Curie, Tour 13, Deuxième Etage,  
 4 Place Jussieu, F-75230 Paris Cedex 05, France

(Received 13 July 1982; revised manuscript received 21 April 1983)

Systematic measurements by light scattering of the linewidth and frequency shift of the  $\vec{q}=0$  optical phonon in silicon over the temperature range of 5–1400 K are presented. Both the linewidth and frequency shift exhibit a quadratic dependence on temperature at high temperatures. This indicates the necessity of including terms in the phonon proper self-energy corresponding to four-phonon anharmonic processes.

I. INTRODUCTION

Experimental studies of the inelastic scattering of light by crystals have provided a great deal of information concerning the optical modes of vibration at the center of the Brillouin zone. In pure materials one finds typically that both the line center and the linewidth vary with temperature. This temperature dependence can be attributed to the anharmonic terms in the vibrational potential energy.<sup>1</sup>

If one restricts oneself to cubic anharmonicity in second order, the damping constant which characterizes the linewidth is proportional to the absolute temperature  $T$  in the high-temperature limit, but when one includes quartic anharmonicity to second order and/or cubic anharmonicity to fourth order, the damping constant involves terms proportional to  $T^2$  in the high-temperature limit.<sup>2</sup> For the case of silicon, Hart, Aggarwal, and Lax<sup>3</sup> have measured the frequency shift of the line center and the damping constant over a range of temperatures from 20 to 770 K. They found that their data for the frequency shift agree rather well with the theoretical calculations of Cowley<sup>4</sup> based on cubic anharmonicity to second order, but their data for the damping constant show significant deviations from Cowley's results. Hart *et al.* were able to show, however, that their data for the damping constant can be fitted satisfactorily by the cubic anharmonic model of Klemens<sup>5</sup> if the zero-temperature value of the damping constant is properly chosen.

Recently, Tsu and Hernandez<sup>6</sup> have reported measurements of the frequency shifts of both one-phonon and two-phonon Raman lines for silicon over the temperature range 20–900°C. Where their results overlap with those of Hart *et al.*, the agreement is good. No data on the linewidth is presented by Tsu and Hernandez.

In the present paper, measurements of the light scattering spectrum of silicon are reported for the temperature range between 5 and 1400 K. The temperature dependences of the frequency shift and damping constant of the Raman active LO phonon are analyzed in terms of cubic and quartic anharmonic contributions. It is found that at the higher temperatures, cubic anharmonic terms to second order are not sufficient to fit the data, but the inclusion of higher-order terms involving cubic and/or quartic anharmonicity makes possible a satisfactory fit.

II. ANHARMONICITY IN LIGHT SCATTERING BY OPTICAL PHONONS

For a system whose equilibrium atomic positions are specified by

$$\vec{R}^{(0)}(l, \kappa) = \vec{R}(l) + \vec{R}(\kappa), \tag{2.1}$$

where  $\vec{R}(l) = l_1 \vec{\tau}_1 + l_2 \vec{\tau}_2 + l_3 \vec{\tau}_3$ , the  $\vec{\tau}_i$  are primitive translation vectors, the  $l_i$  are integers, and  $\vec{R}(\kappa)$  is a vector of the basis; the vibrational Hamiltonian can be written as

$$H = \frac{1}{2} \sum_{l, \kappa, \alpha} \frac{1}{M_\alpha} P_\alpha^2(l, \kappa) + \frac{1}{2} \sum_{l, \kappa, \alpha} \sum_{l', \kappa', \beta} \Phi_{\alpha\beta}(l, \kappa; l', \kappa') u_\alpha(l, \kappa) u_\beta(l', \kappa') + \frac{1}{6} \sum_{l, \kappa, \alpha} \sum_{l', \kappa', \beta} \sum_{l'', \kappa'', \gamma} \Phi_{\alpha\beta\gamma}(l, \kappa; l', \kappa'; l'', \kappa'') u_\alpha(l, \kappa) u_\beta(l', \kappa') u_\gamma(l'', \kappa'') + \frac{1}{24} \sum_{l, \kappa, \alpha} \sum_{l', \kappa', \beta} \sum_{l'', \kappa'', \gamma} \sum_{l''', \kappa''', \delta} \Phi_{\alpha\beta\gamma\delta}(l, \kappa; l', \kappa'; l'', \kappa''; l''', \kappa''') u_\alpha(l, \kappa) u_\beta(l', \kappa') u_\gamma(l'', \kappa'') u_\delta(l''', \kappa''') + \dots, \tag{2.2}$$

where  $\vec{u}(l, \kappa)$  is the displacement of atom  $l, \kappa$  from its equilibrium position and  $\Phi_{\alpha\beta}$ ,  $\Phi_{\alpha\beta\gamma}$ , and  $\Phi_{\alpha\beta\gamma\delta}$  are the harmonic, cubic anharmonic, and quartic anharmonic force constants, respectively. The first two terms are the harmonic Hamiltonian  $H_0$ . The remaining terms are the anharmonic Hamiltonian  $H_A$ . We diagonalize the har-

monic Hamiltonian by means of the normal-coordinate transformation

$$\vec{u}(l, \kappa) = \left[ \frac{\hbar}{2M_\alpha N} \right]^{1/2} \sum_{\vec{q}, j} \frac{\vec{W}(\kappa | \vec{q}, j)}{(\omega_{\vec{q}, j})^{1/2}} e^{i\vec{q} \cdot \vec{R}(l)} A_{\vec{q}, j}, \tag{2.3}$$

$$\bar{P}(l, \kappa) = -i \left( \frac{\hbar M_\kappa}{2N} \right)^{1/2} \sum_{\vec{q}, j} (\omega_{\vec{q}, j})^{1/2} \bar{W}(\kappa | \vec{q}, j) \times e^{i\vec{q} \cdot \vec{R}^{(l)}} B_{\vec{q}, j}. \quad (2.4)$$

Here  $\omega_{\vec{q}, j}$  is the normal-mode frequency for wave vector  $\vec{q}$  and branch index  $j$ ,  $\bar{W}(\kappa | \vec{q}, j)$  is the polarization vector for the normal mode,  $M_\kappa$  is the mass of an atom of type  $\kappa$ ,

and  $N$  is the number of unit cells in the crystal. The field operators  $A_{\vec{q}, j}$  and  $B_{\vec{q}, j}$  are specified in terms of the phonon creation and annihilation operators  $b_{\vec{q}, j}^\dagger$  and  $b_{\vec{q}, j}$  by the relations

$$A_{\vec{q}, j} = b_{\vec{q}, j} + b_{-\vec{q}, j}^\dagger, \quad (2.5)$$

$$B_{\vec{q}, j} = b_{\vec{q}, j} - b_{-\vec{q}, j}^\dagger. \quad (2.6)$$

After making the normal-coordinate transformation, the contributions to the Hamiltonian take the forms

$$H_0 = \frac{1}{4} \sum_{\vec{q}, j} \hbar \omega_{\vec{q}, j} (A_{\vec{q}, j}^\dagger A_{\vec{q}, j} + B_{\vec{q}, j}^\dagger B_{\vec{q}, j}) = \sum_{\vec{q}, j} \hbar \omega_{\vec{q}, j} (b_{\vec{q}, j}^\dagger b_{\vec{q}, j} + \frac{1}{2}), \quad (2.7)$$

$$H_A = \sum_{\vec{q}, j; \vec{q}', j'; \vec{q}'', j''} V(\vec{q}, j; \vec{q}', j'; \vec{q}'', j'') A_{\vec{q}, j}^\dagger A_{\vec{q}', j'}^\dagger A_{\vec{q}'', j''} + \sum_{\vec{q}, j; \vec{q}', j'; \vec{q}'', j''; \vec{q}''', j'''} V(\vec{q}, j; \vec{q}', j'; \vec{q}'', j''; \vec{q}''', j''') A_{\vec{q}, j}^\dagger A_{\vec{q}', j'}^\dagger A_{\vec{q}'', j''}^\dagger A_{\vec{q}''', j'''} + \dots \quad (2.8)$$

The anharmonic coefficients  $V$  are given by

$$V(\vec{q}, j; \vec{q}', j'; \vec{q}'', j'') = \frac{1}{6} \left( \frac{\hbar}{2N} \right)^{3/2} (\omega_{\vec{q}, j} \omega_{\vec{q}', j'} \omega_{\vec{q}'', j''})^{-1/2} N \Delta(\vec{q} + \vec{q}' + \vec{q}'') \times \sum_{\kappa, \alpha} \sum_{\Gamma, \kappa', \beta} \sum_{\Gamma'', \kappa'', \gamma} \Phi_{\alpha\beta\gamma}(0, \kappa; \Gamma', \kappa'; \Gamma'', \kappa'') \times \frac{W_\alpha(\kappa | \vec{q}, j) W_\beta(\kappa' | \vec{q}', j') W_\gamma(\kappa'' | \vec{q}'', j'')}{(M_\kappa M_{\kappa'} M_{\kappa''})^{1/2}} e^{i[\vec{q} \cdot \vec{R}(\Gamma) + \vec{q}' \cdot \vec{R}(\Gamma') + \vec{q}'' \cdot \vec{R}(\Gamma'')]} \quad (2.9)$$

$$V(\vec{q}, j; \vec{q}', j'; \vec{q}'', j''; \vec{q}''', j''') = \frac{1}{24} \left( \frac{\hbar}{2N} \right)^2 (\omega_{\vec{q}, j} \dots \omega_{\vec{q}''', j'''})^{-1/2} N \Delta(\vec{q} + \vec{q}' + \vec{q}'' + \vec{q}''') \times \sum_{\kappa, \alpha} \sum_{\Gamma, \kappa', \beta} \dots \sum_{\Gamma''', \kappa''', \delta} \Phi_{\alpha\beta\gamma\delta}(0, \kappa; \Gamma', \kappa'; \Gamma'', \kappa''; \Gamma''', \kappa''') \times \frac{W_\alpha(\kappa | \vec{q}, j) W_\beta(\kappa' | \vec{q}', j') W_\gamma(\kappa'' | \vec{q}'', j'') W_\delta(\kappa''' | \vec{q}''', j''')}{(M_\kappa \dots M_{\kappa'''})^{1/2}} \times e^{i[\vec{q} \cdot \vec{R}(\Gamma) + \vec{q}' \cdot \vec{R}(\Gamma') + \vec{q}'' \cdot \vec{R}(\Gamma'') + \vec{q}''' \cdot \vec{R}(\Gamma''')]} ,$$

where

$$\Delta(\vec{q}) = \begin{cases} 1 & \text{if } \vec{q} = \vec{G} \\ 0 & \text{otherwise} \end{cases} \quad (2.10)$$

and  $\vec{G}$  is a vector of the reciprocal lattice.

In the case of light scattering, the efficiency for Stokes scattering by zone-center LO phonons in a homopolar crystal is given<sup>7</sup> by

$$\frac{d^2 S}{d\omega d\Omega} = \frac{e^4 L V}{2\pi \hbar^3 m^4 a^2 M N c^4 \omega_{\vec{0}, j}} \left( \frac{\omega_S}{\omega_I} \right) \times (n_0 + 1) |R(j; I, S)|^2 \times \frac{\Gamma(\vec{0}, j; \omega)}{[\omega - \Omega(\vec{0}, j; \omega)]^2 + \Gamma^2(\vec{0}, j; \omega)}, \quad (2.11)$$

where  $R(j; I, S)$  is the Raman tensor, the branch index  $j$  refers to the longitudinal optical branch,  $\vec{\eta}_I$  ( $\vec{\eta}_S$ ) is the wave vector of the incident (scattered) radiation,  $a$  is the lattice constant,  $L$  is the crystal thickness,  $\omega_{\vec{0}, j}$  is the zone-center LO-phonon frequency, and  $n_0$  is the mean number of LO phonons.

The resonant frequency  $\Omega(\vec{0}, j; \omega)$  in Eq. (2.11) determines the scattering line position and is given to first approximation by

$$\Omega(\vec{0}, j; \omega) = \omega_{\vec{0}, j} + \Delta(\vec{0}, j; \omega). \quad (2.12)$$

The quantities  $\Delta(\vec{0}, j; \omega)$  and  $\Gamma(\vec{0}, j; \omega)$  specify the real and imaginary parts of the proper self-energy,  $P(\vec{0}, j; \omega)$ , according to the relation<sup>1</sup>

$$\lim_{\epsilon \rightarrow 0^+} P(\vec{0}, j; \omega + i\epsilon) = -\beta \hbar [\Delta(\vec{0}, j; \omega) - i\Gamma(\vec{0}, j; \omega)] \quad (2.13)$$

and are referred to as the frequency shift and damping constant, respectively. Each of these quantities is the sum of contributions arising from the cubic, quartic, and

higher-order terms in the anharmonic Hamiltonian  $H_A$ . The cubic and quartic contributions up to and including second-order terms are given by<sup>1</sup>

$$\Delta^{(3)}(\bar{0}, j; \omega) = -\frac{18}{\hbar^2} \sum_{\bar{q}_1, j_1} \sum_{\bar{q}_2, j_2} |V(\bar{0}, j; \bar{q}_1, j_1; \bar{q}_2, j_2)|^2 \times \mathcal{P} \left( \frac{n_1 + n_2 + 1}{\omega + \omega_1 + \omega_2} - \frac{n_1 + n_2 + 1}{\omega - \omega_1 - \omega_2} + \frac{n_1 - n_2}{\omega - \omega_1 + \omega_2} - \frac{n_1 - n_2}{\omega + \omega_1 - \omega_2} \right), \quad (2.14a)$$

$$\Delta^{(4a)}(\bar{0}, j; \omega) = \frac{24}{\hbar} \sum_{\bar{q}_1, j_1} V(\bar{0}, j; \bar{0}, j; \bar{q}_1, j_1; -\bar{q}_1, j_1) (n_1 + \frac{1}{2}), \quad (2.14b)$$

$$\Delta^{(4b)}(\bar{0}, j; \omega) = -\frac{96}{\hbar^2} \sum_{\bar{q}_1, j_1} \sum_{\bar{q}_2, j_2} \sum_{\bar{q}_3, j_3} |V(\bar{0}, j; \bar{q}_1, j_1; \bar{q}_2, j_2; \bar{q}_3, j_3)|^2 \times \mathcal{P} \left[ [(n_1 + 1)(n_2 + 1)(n_3 + 1) - n_1 n_2 n_3] \times \left[ \frac{1}{\omega + \omega_1 + \omega_2 + \omega_3} - \frac{1}{\omega - \omega_1 - \omega_2 - \omega_3} \right] + 3[n_1(n_2 + 1)(n_3 + 1) - (n_1 + 1)n_2 n_3] \times \left[ \frac{1}{\omega - \omega_1 + \omega_2 + \omega_3} - \frac{1}{\omega + \omega_1 - \omega_2 - \omega_3} \right] \right], \quad (2.14c)$$

$$\Delta^{(4c)}(\bar{0}, j; \omega) = -\frac{576}{\hbar^2} \sum_{\bar{q}_1, j_1} \sum_{j_2} \sum_{\bar{q}_3, j_3} V(\bar{0}, j; \bar{0}, j; -\bar{q}_1, j_1; \bar{q}_1, j_2) V(\bar{q}_1, j_1; -\bar{q}_1, j_2; \bar{q}_3, j_3; -\bar{q}_3, j_3) \times \mathcal{P} \left( \frac{n_1 + n_2 + 1}{\omega_1 + \omega_2} - \frac{n_1 - n_2}{\omega_1 - \omega_2} \right) (n_3 + \frac{1}{2}), \quad (2.14d)$$

$$\Gamma^{(3)}(\bar{0}, j; \omega) = \frac{18\pi}{\hbar^2} \sum_{\bar{q}_1, j_1} \sum_{\bar{q}_2, j_2} |V(\bar{0}, j; \bar{q}_1, j_1; \bar{q}_2, j_2)|^2 \times \{ (n_1 + n_2 + 1)[\delta(\omega - \omega_1 - \omega_2) - \delta(\omega + \omega_1 + \omega_2)] + (n_1 - n_2)[\delta(\omega + \omega_1 - \omega_2) - \delta(\omega - \omega_1 + \omega_2)] \}, \quad (2.15a)$$

$$\Gamma^{(4)}(\bar{0}, j; \omega) = \frac{96\pi}{\hbar^2} \sum_{\bar{q}_1, j_1} \sum_{\bar{q}_2, j_2} \sum_{\bar{q}_3, j_3} |V(\bar{0}, j; \bar{q}_1, j_1; \bar{q}_2, j_2; \bar{q}_3, j_3)|^2 \times \{ [(n_1 + 1)(n_2 + 1)(n_3 + 1) - n_1 n_2 n_3][\delta(\omega - \omega_1 - \omega_2 - \omega_3) - \delta(\omega + \omega_1 + \omega_2 + \omega_3)] + 3[n_1(n_2 + 1)(n_3 + 1) - (n_1 + 1)n_2 n_3] \times [\delta(\omega + \omega_1 - \omega_2 - \omega_3) - \delta(\omega - \omega_1 + \omega_2 + \omega_3)] \}, \quad (2.15b)$$

where  $\mathcal{P}$  denotes the principal value. In Eqs. (2.14) and (2.15) we have written

$$\omega_i = \omega_{\vec{q}_i, j_i}, \quad i = 1, 2, 3 \quad (2.16a)$$

$$n_i \equiv n_{\vec{q}_i, j_i} = \frac{1}{e^{\beta \hbar \omega_{\vec{q}_i, j_i}} - 1}, \quad i = 1, 2, 3 \quad (2.16b)$$

where  $\beta = 1/k_B T$ . The various contributions to the frequency shift and damping constant are shown diagrammatically in Fig. 1. In addition, there are other diagrams not shown in Fig. 1 which can give nonzero contributions due to the fact that the atoms in silicon do not lie at centers of inversion symmetry.

A specific remark should be made about the temperature behavior of  $\Delta$  and  $\Gamma$ . At high temperatures, i.e., temperatures larger than the Debye temperature, the cubic anharmonic terms in  $\Delta$  and  $\Gamma$  given by Eqs. (2.14a) and (2.15a), respectively, vary linearly with  $T$ . The quartic anharmonic term in  $\Delta$  corresponding to Eq. (2.14b) also varies linearly with  $T$ , but the quadratic terms corresponding to Eqs. (2.14c) and (2.14d) vary quadratically with  $T$ . The quartic anharmonic term in  $\Gamma$  corresponding to Eq. (2.15b) also varies quadratically with  $T$ . Additional  $T^2$  contributions to both  $\Delta$  and  $\Gamma$  arise from terms corresponding to the diagrams in Fig. 2.

The light scattering process can be viewed as involving the absorption of a photon  $\hbar\omega_j$ , the emission of a photon  $\hbar\omega_s$ , and the creation of an optical phonon  $0j$  which then decays via anharmonicity into two phonons, three phonons, etc. The production of two and three phonons is

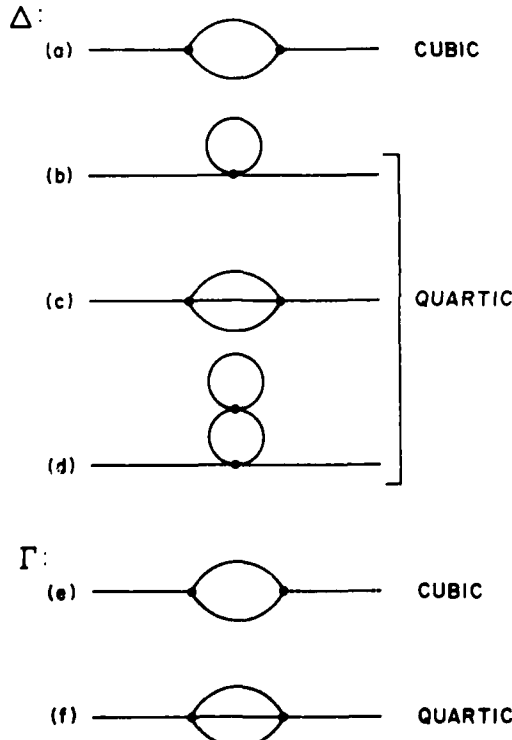


FIG. 1. Diagrams representing contributions to the frequency shift  $\Delta$  and damping constant  $\Gamma$  for the Raman-active LO mode in silicon.

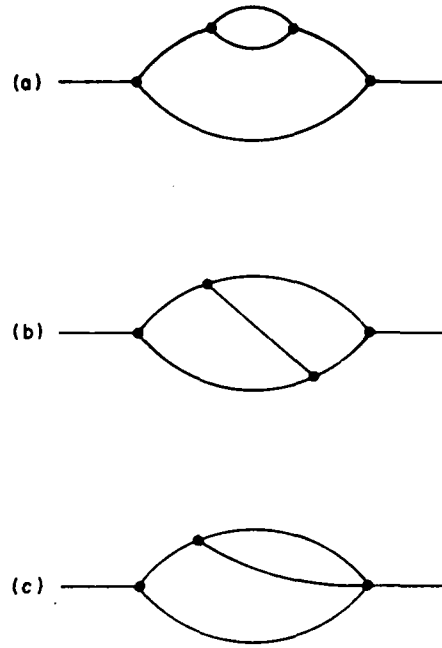


FIG. 2. Diagrams representing higher-order contributions to the proper self-energy of the Raman-active LO mode in silicon.

shown diagrammatically in Figs. 3(a) and 3(c). At nonzero temperatures, processes can also occur in which the decay of the optical phonon  $0j$  is accompanied by the absorption of another phonon, and the emission of one or more phonons, as shown in Figs. 3(b) and 3(d) for the cases of one and two emitted phonons, respectively.

### III. EXPERIMENTAL RESULTS

Light scattering measurements have been performed with a CODERG PHO spectrometer and an excitation laser on single crystal nondoped silicon with a resistivity of 100  $\Omega$  cm and oriented with a (111) face perpendicular to the incident beam. In view of the large temperature range explored the temperature was regulated in a liquid-He cryostat for low temperatures, an electrically heated furnace for the intermediate temperatures, and by laser heating at high temperatures.

The sample temperature was measured by a platinum resistor for low temperatures, by a thermocouple in the intermediate range, and by an optical pyrometer at high temperatures. Verification of the measured temperature was made by two additional methods. The first used the integrated ratio of the Stokes to anti-Stokes Raman peaks. The intensity of the Stokes and anti-Stokes peaks being proportional, respectively, to  $n_0 + 1$  and  $n_0$ , the intensity ratio is

$$\frac{I_S}{I_{AS}} = \exp \left[ \frac{\hbar\omega_0}{k_B T} \right], \quad (3.1)$$

where  $\omega_0$  is the Raman frequency. (We omit the subscript  $j$  from here on.)

The second method was based on the black-body radiation of the sample. If we admit that the sample is a black body we can apply Planck's law for the power emitted per

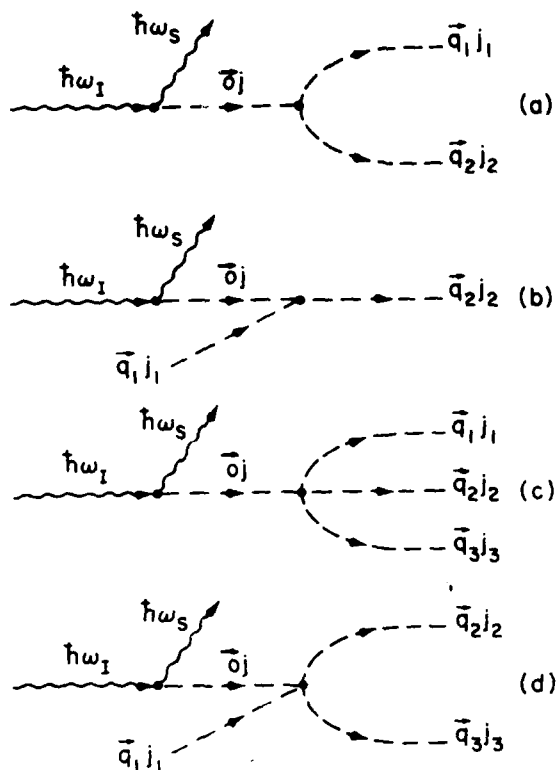


FIG. 3. Diagrams representing three- and four-phonon anharmonic processes contributing to the decay of the Raman-active LO mode in silicon.

unit area,

$$P_e(\omega)d\omega = a(\omega) \frac{\hbar}{4\pi^2 c^2} \frac{\omega^3}{e^{\hbar\omega/k_B T} - 1} d\omega, \quad (3.2)$$

and with  $a(\omega) = 1$  get the sample temperature.

The shape and the position of the peak due to scattering by the Raman-active LO mode in silicon vary for different temperatures. In Fig. 4 we show for comparison two spectra taken at 295 and 1140 K. From these spectra we can deduce the values of  $\Gamma$  and  $\Omega$  for these two temperatures: for  $T = 295$  K,  $\Gamma(0, \text{LO}) = 4$   $\text{cm}^{-1}$ , and  $\Omega(0, \text{LO}) = 520$   $\text{cm}^{-1}$  and for  $T = 1140$  K,  $\Gamma(0, \text{LO}) = 14$   $\text{cm}^{-1}$  and

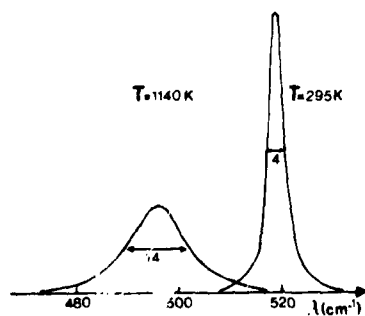


FIG. 4. First-order Raman spectra for silicon at 295 and 1140 K. The line position of the zone-center LO mode shifts from 520  $\text{cm}^{-1}$  at 295 K to 498  $\text{cm}^{-1}$  at 1140 K and the linewidth from 4  $\text{cm}^{-1}$  at 295 K to 14  $\text{cm}^{-1}$  at 1140 K.

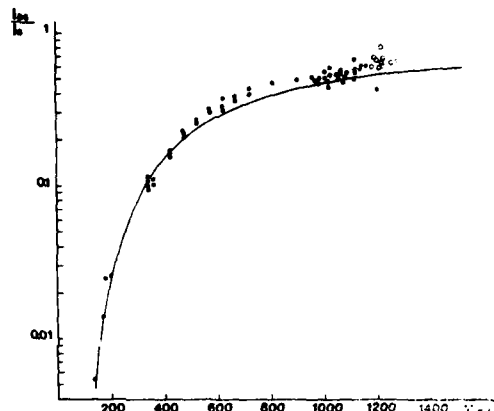


FIG. 5. Anti-Stokes to Stokes intensity ratio vs temperature, considering the correction as discussed in the text. The closed circles represent points for which temperature was measured by a Pt resistor, a thermocouple and for temperatures above 600° C by an optical pyrometer. The open circles are points obtained by heating the sample with the laser and the oven; their temperature is not precisely determined. The theoretical curve  $\exp(-\hbar\omega_0/k_B T)$  is represented by a solid line

$\Omega(0, \text{LO}) = 498$   $\text{cm}^{-1}$ . The Stokes to anti-Stokes ratio of the intensity of these peaks gives the temperature by using the solid line representation given in Fig. 5. In this figure the black line circles represent the Pt resistor, thermocouple, and pyrometric measurements of the temperature. In order to reach the melting point, we heated the sample with the oven and the laser, by increasing the power beam. This is represented by the circles. We should note that for these points we were unable to measure the temperature accurately. The calibration of the solid line applies after the measured Raman intensities have been corrected for the actual absorption coefficient and the frequency dependence of the Raman efficiency. In applying these corrections the expression for the intensity ratio becomes

$$\frac{I_S}{I_{AS}} = \frac{\alpha_I + \alpha_{AS}}{\alpha_I + \alpha_S} \left[ \frac{\omega_S}{\omega_{AS}} \right]^3 \frac{S(\omega_I, \omega_S)}{S(\omega_I, \omega_{AS})} \exp \left[ \frac{\hbar\omega_0}{k_B T} \right], \quad (3.3)$$

where  $\alpha_I, \alpha_{AS}, \alpha_S$  are the absorption constants at the frequencies  $\omega_I, \omega_{AS}, \omega_S$  (incident beam, anti-Stokes, and Stokes) and  $S(\omega_I, \omega_S)$  and  $S(\omega_I, \omega_{AS})$  are the Raman cross sections at the involved frequencies. Practically all the points obtained by pyrometric measurements are above the curve given by the Raman intensity ratio. This indicates that the temperature determined by this method is systematically higher than that obtained by other measurements. A better knowledge of the correction factors is therefore necessary in order for this method to be used for temperature measurements.

The damping constant and the frequency shift have been investigated systematically as a function of temperature. Figure 6 gives the temperature variation of the damping constant  $\Gamma(T)$  between 5 and 1400 K. The dashed curve represents  $\Gamma(T)$  calculated from the relation<sup>3</sup>

$$\Gamma(T) = \Gamma(0) \left[ 1 + \frac{2}{e^x - 1} \right], \quad (3.4)$$

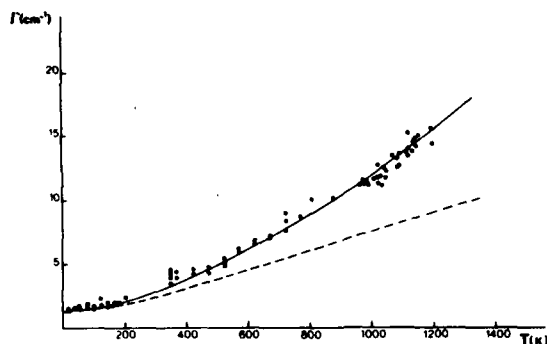


FIG. 6. Temperature dependence of the damping constant  $\Gamma$  for the Raman-active LO mode in silicon. The solid curve gives the theoretical fit using both three- and four-phonon processes. The dashed curve gives the theoretical fit using only three-phonon processes. The open and closed circles have the same significance as in Fig. 5.

where  $x = \hbar\omega_0/2k_B T$  and  $\Gamma(0) = 1.40 \text{ cm}^{-1}$ . Equation (3.4) is an approximate expression for the temperature dependence of the damping constant based on three-phonon processes (cubic anharmonicity in second order) and the simple Klemens<sup>5</sup> model. It seriously underestimates the damping constant at high temperatures. We attribute this discrepancy at least in part to the neglect of four-phonon processes associated with the diagrams in Figs. 1(f) and 2(a)–2(c).

It is of interest to investigate whether this discrepancy can be eliminated by generalizing Eq. (3.4) to include the contribution of four-phonon processes. Following the approach of Klemens<sup>5</sup> we write the kinetic equation for the net rate of decay of an incident phonon into three thermal phonons in the form

$$\frac{d}{dt}(\delta n_0) = -B [(\delta n_0 + n_0)(n_1 + 1)(n_2 + 1)(n_3 + 1) - (\delta n_0 + n_0 + 1)n_1 n_2 n_3], \quad (3.5)$$

where  $\delta n_0$  is the deviation of the incident phonon occupation number from its thermal equilibrium value  $n_0$  and  $B$  is a constant. Using the equilibrium condition

$$n_0(n_1 + 1)(n_2 + 1)(n_3 + 1) - (n_0 + 1)n_1 n_2 n_3 = 0, \quad (3.6)$$

we can rewrite Eq. (3.5) as

$$\frac{d}{dt}(\delta n_0) = -B(n_1 n_2 + n_1 n_3 + n_2 n_3 + n_1 + n_2 + n_3 + 1)\delta n_0. \quad (3.7)$$

Energy conservation can be satisfied in the simple Klemens fashion by setting  $\omega_1 = \omega_2 = \omega_3 = \omega_0/3$ . Consequently,  $n_1 = n_2 = n_3$ . The generalization of Eq. (3.4) to four-phonon processes then takes the form

$$\Gamma(T) = A \left[ 1 + \frac{2}{e^x - 1} \right] + B \left[ 1 + \frac{3}{e^y - 1} + \frac{3}{(e^y - 1)^2} \right], \quad (3.8)$$

where  $y = \hbar\omega_0/3k_B T$  and  $A$  and  $B$  are constants. In the high-temperature limit, the factors multiplying  $A$  and  $B$  in Eq. (3.8) vary as  $T$  and  $T^2$ , respectively.

Equation (3.8) has been used to fit the experimental data presented in Fig. 6 by suitably choosing the constants  $A$  and  $B$ . The best values of  $A$  and  $B$  are found to be 1.295 and  $0.105 \text{ cm}^{-1}$ , respectively, and the resulting plot of  $\Gamma(T)$  vs  $T$  is given by the solid curve in Fig. 6. We see that the agreement between the calculated curve and the experimental points is now quite good.

The experimental results for the line position  $\Omega(T)$  as a function of  $T$  are shown in Fig. 7. Also shown is the fit to the data (solid curve) specified by the expressions

$$\Omega(T) = \omega_0 + \Delta(T) \quad (3.9)$$

and

$$\Delta(T) = C \left[ 1 + \frac{2}{e^x - 1} \right] + D \left[ 1 + \frac{3}{e^y - 1} + \frac{3}{(e^y - 1)^2} \right], \quad (3.10)$$

where  $\omega_0$ ,  $C$ , and  $D$  are constants with the values 528,  $-2.96$ , and  $-0.174 \text{ cm}^{-1}$ , respectively. Equation (3.10) is the analog of Eq. (3.8) and specifies the contributions of three-phonon and four-phonon processes to the frequency shift. The agreement between the experimental points and the solid curve is seen to be good.

If we try to fit the experimental data with three-phonon processes only by omitting the term in Eq. (3.10) with the factor  $D$ , we obtain the dashed curve in Fig. 7 with  $\omega_0 = 529 \text{ cm}^{-1}$  and  $C = -4.24 \text{ cm}^{-1}$ . Although this curve fits the data well at temperatures up to 600 K, it is clearly inadequate at higher temperatures. This demonstrates the necessity of including terms corresponding to four-phonon processes in the expression for  $\Delta(T)$ .

In principle, the four-phonon contributions in Eqs. (3.8) and (3.10) should include terms arising from difference processes of the type represented by Fig. 3(d). We have omitted such terms on the grounds that their inclusion

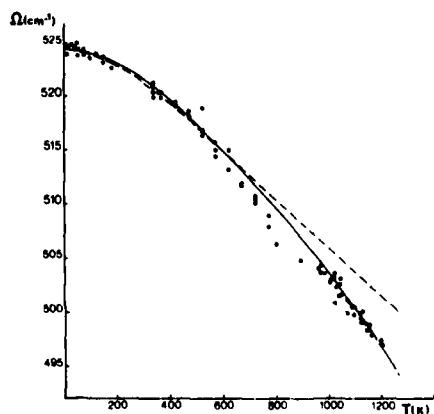


FIG. 7. Temperature dependence of the line position  $\Omega$  for the Raman-active LO mode in silicon. The solid curve gives the theoretical fit using both three- and four-phonon processes. The dashed curve gives the theoretical fit using only three-phonon processes. The open and closed circles have the same significance as in Fig. 5.

would simply introduce additional terms varying as  $T$  and as  $T^2$  in the high-temperature limit and would not add any new qualitative features.

#### IV. DISCUSSION

We have seen in the previous section that the extension of the Klemens-Hart-Aggarwal-Lax model<sup>3,5</sup> to include four-phonon processes provides a good fit to the experimental values for the frequency shift and damping constant of the Raman-active mode in silicon up to 1400 K. This fit is achieved by suitably choosing two adjustable parameters for each of the two quantities. Since one would expect the contribution of four-phonon processes to be small compared to that of three-phonon processes, the ratios  $B/A$  and  $D/C$  should be small. The actual values of these ratios are 0.08 and 0.06, respectively, so this expectation is fulfilled.

It would, of course, be desirable to carry out a first-principles calculation of the frequency shift and damping constant arising from both cubic and quartic anharmonicity. However, such a calculation is by no means trivial. The principal difficulty is that a simple model such as a nearest-neighbor model is inadequate to describe either the harmonic or the anharmonic properties of silicon. This was shown a quarter century ago by Herman<sup>8</sup> and by Lax<sup>9</sup> for the harmonic properties and very recently by Wanser

and Wallis<sup>10</sup> for anharmonic properties. Long-range forces are necessary for a proper description and can be introduced via a shell model,<sup>11</sup> a bond charge model,<sup>12</sup> or a model containing dipole-dipole and/or quadrupole-quadrupole interactions.<sup>9,10,13</sup>

Cowley<sup>4</sup> has carried out a calculation of the frequency shift and damping constant for silicon at temperatures up to 500 K using a shell model for the harmonic forces and a nearest-neighbor model for the anharmonic forces. Reasonable agreement with the experimental data was obtained by Cowley for the frequency shifts, but not the damping constant.<sup>3</sup> We are currently engaged in making a calculation of these quantities using the long-range force model of Wanser and Wallis generalized to quartic anharmonicity.

#### ACKNOWLEDGMENTS

We wish to thank Consejo Nacional de Ciencia y Tecnología (CONACYT) of Mexico for supporting the work of one of us (E.H.), the U. S. National Science Foundation for supporting the work of another of us (R.F.W.) under Grant No. DMR-82-14214, and the European Research Office for supporting the work of another of us (M.B.) under Grant No. DAJA 37-81-C-0587. One of us (E.H.) wishes to thank J. F. Morhange for helpful discussions.

\*Permanent address: Department of Physics, University of California, Irvine, Irvine, California 92717.

<sup>1</sup>R. F. Wallis, I. P. Ipatova, and A. A. Maradudin, *Fiz. Tverd. Tela Leningrad* **8**, 1064 (1966) [*Sov. Phys.—Solid State* **8**, 850 (1966)]; I. P. Ipatova, A. A. Maradudin, and R. F. Wallis, *Phys. Rev.* **155**, 882 (1967).

<sup>2</sup>D. W. Jepsen and R. F. Wallis, *Phys. Rev.* **125**, 1496 (1962).

<sup>3</sup>T. R. Hart, R. L. Aggarwal, and B. Lax, *Phys. Rev. B* **1**, 638 (1970).

<sup>4</sup>R. A. Cowley, *J. Phys. (Paris)* **26**, 659 (1965).

<sup>5</sup>P. G. Klemens, *Phys. Rev.* **148**, 845 (1966).

<sup>6</sup>R. Tsu and J. G. Hernandez, *Appl. Phys. Lett.* **41**, 1016 (1982).

<sup>7</sup>R. Loudon, *Proc. R. Soc. London Ser. A* **275**, 218 (1963).

<sup>8</sup>F. Herman, *J. Phys. Chem. Solids* **8**, 405 (1959).

<sup>9</sup>M. Lax, *Phys. Rev. Lett.* **1**, 133 (1958).

<sup>10</sup>K. H. Wanser and R. F. Wallis, *J. Phys. (Paris) Colloq.* **42**, C6-128 (1981).

<sup>11</sup>W. Cochran, *Proc. R. Soc. London Ser. A* **253**, 260 (1959).

<sup>12</sup>W. Weber, *Phys. Rev. B* **15**, 4789 (1977).

<sup>13</sup>M. Lax, *Symmetry Principles in Solid State and Molecular Physics* (Wiley, New York, 1974).

## FUNDAMENTALS OF LASER ANNEALING

M. BALKANSKI

Laboratoire de Physique des Solides, Associé au C.N.R.S.,  
Université Pierre et Marie Curie  
4, Place Jussieu, 75230 PARIS CEDEX 05, France

### 1. INTRODUCTION

One of the most fascinating debates in the field of Semiconductors Physics in recent years, centers on the fundamental interpretation of laser annealing. The question of the energy transfer from an intense beam to a disordered material, such as amorphous silicon, resulting in the crystallization of the amorphous substance has been approached from two different points of view, both referring to a set of fairly clear experimental results. On one hand, a claim has been made that the laser beam simply heats the sample up to melting the amorphous material which on cooling crystallizes from melt [1-4]. On the other hand, one has considered that amorphous to crystalline phase transition can occur at low temperatures without passing through the molten state [5]. Many arguments have been developed in support of these interpretations. A large number of publications have appeared in the literature.

In addition to the fundamental interest, laser annealing has been considered to have a strong potential in the technology of semiconductor doping by ion implantation. For all these reasons, the attention of a large audience has been focussed on this problem.

### 2. STRUCTURAL ANALYSIS AFTER LASER ANNEALING

#### 2.1. Amorphous - Crystalline transformation

The aim of laser annealing is to achieve the transformation of the amorphous material obtained by ion implantation into perfect crystal. Therefore, we shall first discuss the results of the structural analysis after annealing.

One of the methods which seems to be most appropriate to define the degree of crystallinity of the material is light scattering. The light scattering spectrum of amorphous silicon for example, is very different from that of the perfect crystal.

Laser annealing performed with Ruby Q-switched laser delivering pulses of about one hundred nanoseconds with energy density of the order of one J/cm<sup>2</sup> is described by Morhange [6]. At this energy density, the diameter of the power laser beam was of the order of one mm. The annealed region is explored with an Argon laser probe beam focussed to a diameter of 80 μm. The probe beam is used for Raman spectroscopy. With this arrangement, it was possible to explore the annealed region in the xy plane by moving the sample with regard to the probe beam and in the z direction by varying the

frequency of the probe beam inducing changes in the penetration depth in the a-Si sample.

Two parameters characterize the annealed Si: the frequency position of the Raman line and its half width. For monocrystalline Si, the Raman active normal mode is observed at  $520,5 \text{ cm}^{-1}$  with a half width of  $3 \text{ cm}^{-1}$ . When ion implanted samples having a thickness of the amorphous layer of  $5000 \text{ \AA}$  are investigated, the annealed region does not show a uniform single crystal structure. At the center of the irradiated region, the Raman peak frequency is  $519 \text{ cm}^{-1}$ , shifted by  $1,5 \text{ cm}^{-1}$  towards lower frequencies. The width of the peak is  $6 \text{ cm}^{-1}$  significantly broader than the single crystal peak. When the probe beam is moved towards the periphery of the power laser irradiated region, the frequency shift increases and reaches  $5,5 \text{ cm}^{-1}$  at the edge of the annealed area. The band is also broader and has a width of  $10 \text{ cm}^{-1}$  near the edge. These results are displayed in Figure 1, where the circles represent the extent of the power laser beam and the dots indicate the position of the probe beam for the spectrum represented on the left side of the figure.

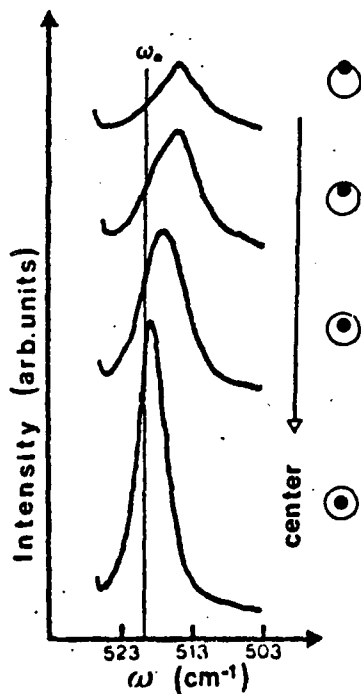


Figure 1. Raman spectra coming from various points along a diameter of a laser annealed region. From J.F. MORHANGE et al. Proceedings of the Material Research Society Annual Meeting, Boston, 1978 (American Institute of Physics, New-York 1979) p. 429.

These results could be viewed as follows. Even at the center of the annealed region, laser annealing does not lead to a large single crystal in the way it would be obtained in equilibrium epitaxial regrowth. Instead, the annealed material consists of large polycrystallites whose dimensions decrease as one approaches the interface between annealed and amorphous material. The recrystallization occurs as a result of random nucleation in the amorphous layer. The dimensions of the crystallites

depend on energy distribution in the incident power laser beam. The crystallite dimensions determine the frequency shift of the Raman active normal mode band. An account of the normal mode frequency shift as a function of the dimension of the crystallite is given by a simple lattice dynamics calculation developed by Kanellis [7]. The model used in this calculation is that of a thin slab limited in one direction and infinite in the plane perpendicular to that direction. In the case of Si, the results obtained are shown in Figure 2.

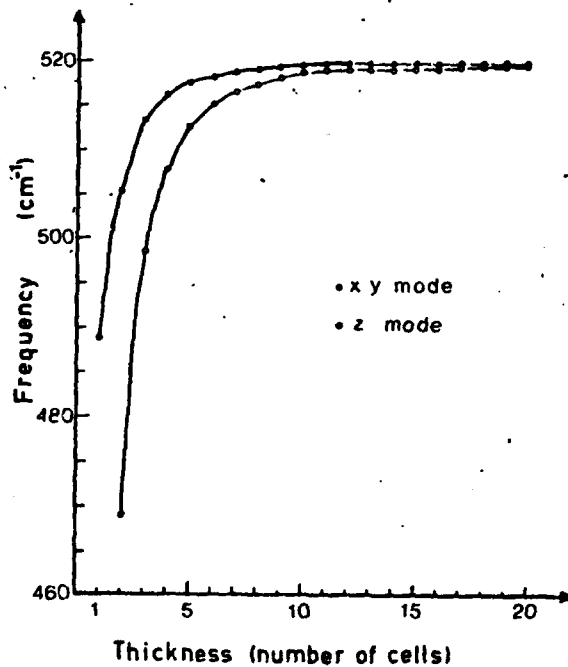


Figure 2. Frequency variation of the higher-frequency optical modes as a function of the number of cells. From G. KANELIS et al., Phys. Rev. B21, 1543 (1980)

In this figure the frequency shift of the two high frequency modes are represented. These are the surface modes which in the limit of infinite crystal tends toward the Raman active mode at the center of the Brillouin Zone. These calculations show that for crystallite having dimensions smaller than 80 Å, a noticeable frequency shift should occur. Indeed, the experimental observations show that in the region near the crystalline-amorphous interface a significant frequency shift is measured. From this theoretical model and the experimental results, we draw the conclusion that in laser annealing, the crystallization occurs randomly.

An amorphous network is not a perfectly regular structure. The energy supplied by the laser beam at threshold is sufficient to soften bonds in the less favourable topological situation and allow nucleation. Crystal-

lographic ordering develops around the randomly distributed nucleus embedded in the amorphous background creating microcrystalline clusters whose size depends on the energy density distribution.

First order phase transitions such as melting or crystallization take place, in general, via nucleation and growth of microphases. Unstable phases of Si have also been prepared in high-pressure experiments [8]. Phillips [9] has given evidence of metastable phases in laser-induced and thermally reversible microcrystallization in the chalcogenide glass formers  $\text{GeSe}_2$ . Recent light scattering experiments [10] shows the existence of microcrystallites embedded in the glass ( $\text{GeSe}_2$ ) during laser annealing. The microcrystalline clusters initially formed are free to rotate and form larger clusters, a fact which is expressed by Raman line narrowing and demonstrates a precursor effect in the laser induced glass to crystal transition. These experiments although achieved in different materials and in a very different time scale might be suggestive of the processes occurring in silicon.

## 2.2. Picosecond laser induced patterns on silicon single crystal surface

It is generally believed that monocrystalline silicon being a well defined target would yield unambiguous indication about the mechanism of the transformations produced by a laser beam on a semiconductor.

The surface of a silicon single crystal may be transformed into an amorphous layer by a single picosecond pulse [11]. Optical observation show the formation of an amorphous ring pattern on a (111) crystal surface after exposure to a laser pulse at 532 nm with an average duration of 30 ps and with a spot having a size of the order of  $5 \cdot 10^{-4} \text{ cm}^2$ . At lower intensities, the ring diameter becomes smaller, the amorphous region coalesces to a spot at the center and disappears below a critical intensity threshold. At 532 nm, the threshold is reported to be  $0,18 \text{ J/cm}^2$  for (100) and  $0,08 \text{ J/cm}^2$  for (111) surfaces. Amorphous rings rather than central spots are formed for intensity levels exceeding  $0,24 \text{ J/cm}^2$  for (100) and  $0,12 \text{ J/cm}^2$  for (111) surfaces. The center in this case is a single crystal with the same orientation as the substrate. The amorphous nature of the rings was deduced from an increase of the reflectivity compared to crystalline silicon and was confirmed by electron diffraction with a transmission electron microscope.

The annular pattern of the amorphous phase is interpreted in terms of cooling rate and crystal-growth speed. It is first assumed that above threshold, the laser pulse induces melting of the silicon target.

Following laser pulse melting, two limiting cases are then proposed : just above the threshold intensity, a layer of depth somewhat smaller than  $5 \cdot 10^{-6} \text{ cm}$  is cooled in  $t = 3 \cdot 10^{-11} \text{ s}$  and the condition,  $d/U_M > t$ , for nucleation of an amorphous solid phase, is fulfilled. Well above the threshold intensity, the temperature of the molten layer rises far above  $T_m$  and the cooling rate in the critical region below  $0.8 T_m$  becomes longer. This gives a description of the annular pattern of the amorphous phase.

## 2.3. Picosecond laser annealing of implanted silicon

Experiments analogous to that described in the previous chapter for silicon single crystal surface have been performed by Liu et al [12] on ion

implanted amorphous silicon.

With a laser beam of  $1.06 \mu\text{m}$ , beside the annular amorphous region and recrystallized center, one also observes a recrystallized ring. Both the ring and the center are polycrystals. The energy fluence level to form the ring is  $0.22 \text{ J/cm}^2$ . It is  $0.35 \text{ J/cm}^2$  for the a-Si region and  $0.85 \text{ J/cm}^2$  or the recrystallized region.

Rozgonyi et al [13] have re-examined the structural modification of amorphized silicon surfaces following picosecond laser irradiation using cross-section transmission electron microscopy and showed that the center is always a dislocation free single crystal encircled by poly-silicon ring. This observation is consistent with the results of Morhange et al [14] obtained by Raman spectroscopy.

More recently, Nissim et al [15] have performed light scattering measurements analogous to that reported by Morhange et al. [14] scanning the irradiated area with a probe laser beam focussed on a  $1 \mu\text{m}$  diameter spot. When a single 30ps pulse at  $1.06$  and  $0.532 \mu\text{m}$  wavelengths from a mode-locked neodymium : Yttrium Aluminium Garnet laser is used, a multi annular recrystallization pattern is observed on implanted silicon. At high incident energies, single crystal silicon is observed in the central spot and in the first recrystallized ring of the annealed area. With an irradiation at  $1.06 \mu\text{m}$ , the threshold of laser induced damage was found to be above  $2 \text{ J/cm}^2$ . The multi annular pattern has been ascribed to multiple melting resolidification process during the pulse duration leading to the superposition of basic structures of different sizes.

For the understanding of this complex structures, it should also be remembered that periodic surface structures on solids may result from inhomogeneous energy deposition associated with the interference of the incident beam with a surface scattered field as discussed by Van Driel et al [16].

### 3. TIME RESOLVED ANALYSIS OF PULSED LASER IRRADIATION OF SEMICONDUCTORS

For the discussion of the data obtained by short laser irradiation pulses one could distinguish three different time ranges : i) very short time scale,  $t \ll 10^{-12}$  s, where the system is in a far from equilibrium state, the seat of highly non linear processes, ii) intermediate time scale,  $t \sim 10^{-12}$  s when different elementary relaxation processes take place and iii) long time range  $t > 10^{-9}$  s when thermalization occurs and the system tends toward equilibrium.

#### 3.1. Investigations in the very short time range

A radiation beam, of energy density of  $1 \text{ J/cm}^2$ , is bound to produce a strong perturbation on the material at the instant of interaction. The photon density is such that a hot electron plasma might be produced.

The experiments in the shortest time scale are these of optical pulse induced phase transitions in silicon described by Shank, Yen and Hirlimann [17]. They reported the first observations of optically induced reflectivity changes in silicon with 90 fs optical pulses.

The results of reflectivity measurements are shown in Figure 3. The

energy  $E_{th}$  is defined as the excitation energy density where visual evidence of amorphous layer formation is observed. This energy corresponds to  $0.1 \text{ J/cm}^2$ .

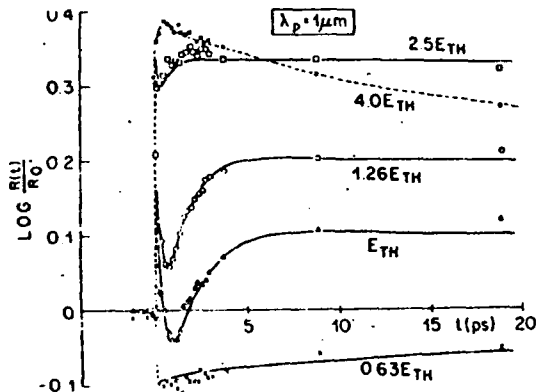


Figure 3. Transient reflectivity data in Silicon at probe wavelength  $1 \mu\text{m}$  and pump wavelength  $620 \text{ nm}$  at various incident energies.

From C.V. SHANK et al., Phys. Rev. Letters 50, 454 (1983).

Shank et al [17] discuss the results shown in Figure 3 in the following way. Optical excitation of Si with a  $2.0 \text{ eV}$  optical pulse results in the generation of a dense electron-hole plasma within the optical absorption depth:  $\alpha^{-1} = 3 \mu\text{m}$ . They suppose that during the earlier time following excitation, the reflectivity is dominated by the electron-hole plasma. As the pulse intensity is increased, the energy is transferred to the crystal lattice and the crystal melts. It is also supposed that melting begins at the surface and moves inward into the bulk.

Probably, the most important contribution of this investigation is the demonstration that when the crystal is excited with a short optical pulse of  $90 \text{ fs}$  a form of unstable highly excited silicon is created which persists for a fraction of picosecond. A challenging programme now is to determine the properties of this material with at least  $10 \%$  of the available electrons excited.

### 3.2. Intermediate time range. Picosecond irradiation

Most of the work on time resolved spectroscopy is in the range of the picosecond for the simple reason that this is the time scale for which short pulse laser sources are readily available.

Experiments in the picosecond range on transmission and reflectivity were performed by Liu et al. [18] at the fundamental and doubled frequency

of a mode-locked Nd : YAG laser producing a 30 ps single pulse. In this work are presented measurements on self reflectivity and self-transmission at  $\lambda = 532$  nm for increasing energy fluence with 20 ps pulses. The self-reflectivity of bulk silicon with (111) surface starts to increase when the energy fluence of the pump beam reaches  $0.2 \text{ J/cm}^2$ . The initial rise of the reflectivity from the crystalline value of 0.37 to a maximum value of 0.48 is in agreement with changes in the index of refraction due to melting of a thin surface layer. In this case, it is supposed that the hot e-h plasma transfers sufficient energy for melting within the duration of the pulse itself. Below the critical fluence level of  $0.2 \text{ J/cm}^2$ , the photoexcited e-h plasma causes a decrease in the real part  $n$  of the complex refractive index.

A pump and probe technique was also used where a picosecond excitation pulse is followed by a slightly focussed weak probe with a variable time delay.

At 100 ps delay, the probe pulse is temporarily completely separated from the pump pulse, and an abrupt rise in reflectivity at the threshold fluence of  $0.2 \text{ J/cm}^2$  is observed [18]. This discontinuity in the carrier density should be associated with local structural changes. The reflectivity rises to  $0.75 \pm 0.03$  which is characteristic of molten silicon at the probe wavelength of  $1.064 \mu\text{m}$ . This behaviour is observed even at zero delay indicating that melting occurs within the pulse duration of 20 ps.

### 3.3. Long time phenomena

At long time, the energy is transferred to the lattice which eventually melts. For the long time phenomena, we are faced with three major problems :

- i) what is the mechanism of melting,
- ii) do intermediate, metastable phase exist in the further thermalization,
- iii) what is the microscopic mechanism of resolidification.

There are two experimental approaches to these questions :

- a) determination of the temperature of the system,
- b) direct observation of the structural phase transformation during the evolution of the system towards thermalization.

We have discussed in paragraph 2 the structural observations and the insight they could be for the dynamical evolution of the system. We shall now focuss on considerations on the determination of the temperature of the system : the electron gas temperature and the lattice temperature.

### 3.4. Energy transfert and carrier density

Of particular interest for the understanding of the laser action on a solid is the analysis of the initial events following the irradiation by an intense optical pulse. Femtosecond spectroscopy has already shown to be a valuable method for such an analysis [17, 19, 20]. Measurements on the time dependent reflectivity leads to estimation of the electron hole density, initially created as well as its evolution with time. Such measurements are also suggestive for models for the energy transfer during and after the irradiation.

The questions to be considered are the following :

- i) what is the electron-hole (e-h) density resulting from the excitation.
- ii) what are the interaction processes behind the excitation.
- iii) how is the energy stored in the excited carriers and transferred to the rest of the system.

i) electron-hole density produced by femtosecond pulse

The high density electron-hole plasma in silicon created by a 90 femtosecond pulse has been investigated [17] by measuring the time dependent reflectivity over a 20 picoseconds time scale, at various laser energies. Such short pulses lead to the possibility to break so many covalent bonds that the crystal becomes fluid even at  $T = 0$  K. The carrier density created at this time scale was estimated to be of the order of  $5 \cdot 10^{21} \text{ cm}^{-3}$  under an incident energy density of  $0.063 \text{ J/cm}^2$ . The phenomena produced in such very short pulses can be viewed in the following way [20]. The part of the initial laser beam absorbed over a penetration depth of  $d = 3 \mu\text{m}$  creates an electron hole plasma with a decreasing density profile. After the surface density reaches a fraction of  $N_p$ , the plasma density, the reflectivity and the penetration depth fall, because of the decrease of the real part of the dielectric constant as well as of the increase of the induced free carrier absorption. For high enough power, the surface density goes beyond  $N_p$  within the pulse, yielding an instantaneous reflectivity larger than  $R_0$  the initially reflected beam. At that high surface density the laser beam becomes a vanishing wave which can create e-h pairs only very close to the surface.

The reflectivity during the pulse  $R(t)$  is obtained through a general resolution of the Maxwell equations, taking into account the variation of the dielectric constant via the modification of the e-h density profile.

The experimental data [20] are fitted with a relaxation time  $\tau = 3 \cdot 10^{-16}$  s. For  $\lambda = 0,31 \mu\text{m}$  the plasma frequency density can be as high as  $2 \cdot 10^{22} < N_p < 8 \cdot 10^{22} \text{ cm}^{-3}$  which is indeed very high in view of the total number of valence band electrons ( $2 \cdot 10^{23} \text{ cm}^{-3}$ ).

ii) electron-gas temperature

An interesting investigation on the photoexcited electron distribution is performed by non-linear photoemission from silicon by Bensoussan and Moison [21]. They show that in Si, at moderate fluences an equilibrium distribution coexists with the electrons at very high energies in the conduction band, generated by two and three quantum processes. The equilibrium distribution is described by a well-defined temperature which differs significantly from the lattice temperature. Because of the fast photogeneration of the carriers, and of the two photon absorption and biparticle Auger recombination processes in which carriers are sent continuously high in the bands, the electron gas can reach an internal equilibrium characterized by a temperature  $T_e$  higher than the lattice temperature  $T_l$ . The experimentally measured thermal emission is interpreted by the Richardson equation. The temperatures deduced for different fluences are shown in Figure 4.

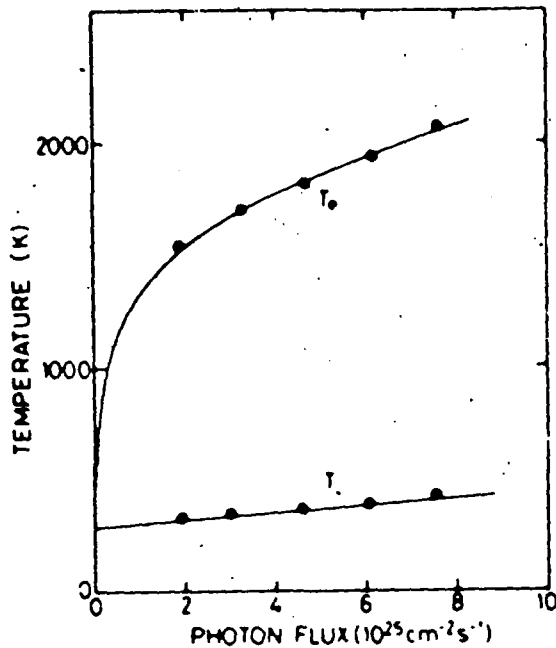


Figure 4. Electron and lattice temperatures vs. photon flux.

From M. BENSOUSSAN. Proceedings of the 16th International Conference on the Physics of Semiconductors. North-Holland, Editor M. Averous (1982) p. 405.

### iii) lattice temperature

Lattice temperature at equilibrium can be inferred from light scattering measurements of the frequency shift and line width of the LO mode 22 and Stokes to anti-Stokes ratio [23]. The Stokes to anti-Stokes ratio indicates a lattice temperature of 1400 K for a delay of 150 ns after excitation with a power beam of  $0.8 \text{ J/cm}^2$  at 532 nm. Raman measurements are evidently taken after the high reflectivity falls off.

## 4. DISCUSSION AND CONCLUSIONS

Laser annealing has now a long history and an abundant literature. The interesting question, which still remains to be answered, is what are the elementary processes in the interaction of a strong radiation field with matter.

The process of laser annealing consists of two sets of phenomena. The first concerns the effect of a dense radiation field on matter creating elementary excitation far from equilibrium. The initial hot plasma redistributes through interactions between carriers and ultimately thermalizes giving up energy to heavier particles which are the lattice constituents. The second set of phenomena, of a completely different nature, concerns the modifications induced to the solid as a result of the creation of the dense hot plasma. If the laser pulse is short enough, the e-h density reached corresponds to an amount of broken covalent bonds which is a significant portion of the total number of bonds, the crystal becomes fluid even at  $T = 0 \text{ K}$ . Ultimately, the solid sets in a new phase whose structure depends on the elementary mechanisms of interaction and organi-

AD-A146 979

LASER ANNEALING OF ION IMPLANTED SEMICONDUCTORS(U)  
PARIS-6 UNIV (FRANCE) J F MORHANGE ET AL. JUL 84  
DAJA37-81-C-0587

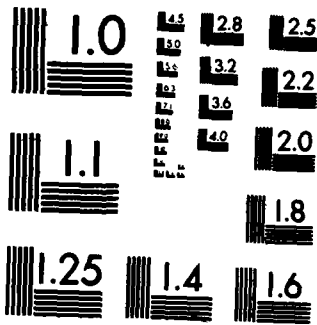
2/2

UNCLASSIFIED

F/G 20/12

NL





zation of the lattice constituents. We shall examine successively these two states as : i) direct laser effect and ii) consequences of the laser action.

#### 4.1. Direct laser effect

The incident laser energy is absorbed by electron-hole pairs creation and by free carrier excitation. In indirect gap semiconductors, electron-hole pairs are created via indirect absorption processes involving the emission and absorption of phonons. Because phonon energies are much smaller than photon energy, the amount of energy transferred to the lattice during absorption is negligible in comparison to the total amount absorbed. The rise of carrier density leads, in turn, to increased free carrier absorption. The net result is the production of hot-electrons and holes far from equilibrium which subsequently thermalize with the set of the carriers and eventually with the lattice. The observations by Shank et al [17] demonstrate that with short, 90 femtoseconds optical pulse, an unstable form of highly excited state is created near the surface which persists for a fraction of picosecond.

For very short impulsion of radiation, from the experiments [17, 20] one perceives clear indications that there are two steps of the laser action on a crystal well separated in time. In the first step, the electromagnetic energy transferred from the laser beam to the solid is retained in the highly excited non-equilibrium electronic state. In a second step, this energy is transferred to the lattice.

Recently, a theoretical model [20] is proposed which takes into account the space time evolution of the plasma during the pulse in order to explain the processes in densities higher than  $10^{22} \text{ cm}^{-3}$  reached in 100 fs pulses. The novelty in this model is the argument that free carrier absorption is dominated by e-h collisions with a characteristic relaxation time  $\tau = 3 \cdot 10^{-16} \text{ s}$ .

A different situation is reached with much longer pulses :  $\tau_L = 10 \text{ ns}$  and a photon absorption rate  $g \sim 10^{31} \text{ cm}^{-3} \text{ s}^{-1}$  : Auger recombination becomes the dominant recombination mechanism at these densities.

Most of the laser energy is absorbed by the carriers within the absorption depth. Eventually, these carriers loose their energy to the lattice, the rise of the lattice temperature then depends on the distance they have diffused before substantial phonon emission occurs. At moderate density, the phonon scattering time is  $\tau \sim 10^{-13} \text{ s}$ . Screening does not affect the rate of intervalley phonon emission until  $N_e \sim 10^{21} \text{ cm}^{-3}$ . Because screening increases the electron-phonon scattering time, it not only decreases the rate of phonon emission but also enhances diffusion. This increases the volume of the region in which the energy of the excited carriers is transferred to the lattice. Owing to the extreme non linearity of the hot carrier effects, it is impossible to make an accurate estimate of the precise temperature to which the lattice is heated or to determine the laser power threshold above which melting will occur.

#### 4.2. Consequences of the laser action

The equilibrium observations are clear : an amorphous or glass solid is transformed into crystal under laser action and a crystal submitted to

very short laser irradiation is transformed into amorphous material. An implication of both of these transformations is that melting precedes the transition. Another alternative is that the phase transition is directly induced in the highly excited state.

The effect of a dense plasma on the melting temperature is itself an interesting problem of solid state theory. This question has been recently addressed by Bok and Combescot [24]. It is shown that in the presence of a dense plasma, the melting temperature of a solid changes. The melting temperature decreases with increasing plasma density. For a laser pulse of  $1 \text{ J/cm}^2$  during 10 ns, it is considered that e-h plasma reaches a steady state in a time shorter than the laser pulse. Considering the plasma expansion due to its high pressure, its collision with phonons and Auger recombination, the highest plasma density is of the order  $10^{21} \text{ cm}^{-3}$ . This density is nevertheless considered to be sufficient to considerably reduce the melting temperature so that a metallic layer of liquid silicon is formed at the surface.

The role of a high plasma density in laser annealing has been discussed by Van Vechten et al. [5] in a quite different way but still involving electron-phonon coupling and lattice instability induced by this interaction. Above a critical carrier density estimated at  $8 \cdot 10^{21} \text{ cm}^{-3}$ , a second order phase transition occurs. At this plasma density, the bond charges will be so depleted that they will no longer be able to stabilize the TA phonon modes [25]. The crystal will no longer resist shearing stresses and will become fluid. This fluid is distinct from the normal molten phase of Si the latter being the result of a strictly first order phase transition driven by the atomic motion at high temperatures. The assumption of Van Vechten is that the plasma is supposed to directly induce the structural transformation. The energy is retained in the electronic system instead of being entirely associated with the atomic motion. As the plasma becomes less dense due to expansion and to transfer of energy to the lattice, the material will pass back through the second order phase transition at  $8 \cdot 10^{21} \text{ cm}^{-3}$  and covalent bonding will gradually appear. The material will finally recrystallize if this process is relatively slow or will solidify in the amorphous phase if the process is very fast.

This dense plasma phase could be compared to the highly excited silicon which persists for a fraction of a picosecond [17, 20]. The interpretation of the laser action differs nevertheless with regard to the following step; it is generally considered that the solid melts after the initial interaction stage.

In conclusion, few points appear clear today. The laser interaction with the solids results first in the creation of a dense plasma which persists for a fraction of a picosecond. Melting seems to occur after the excitation pulse. The mechanism of melting is not clear and consequently the mechanism of solidification is not clear either. Further investigation in the very short impulse regime are certainly desirable to clarify the physical processes in laser annealing.

#### ACKNOWLEDGMENT

The research reported here in has been sponsored in part by the United States Army through its European Research Office.

## REFERENCES

- 1 J.C. Wang, R.F. Wood and P.P. Pronko : Appl. Phys. Lett. 33, 455 (1978)
- 2 P. Baeri, S.U. Campisano, G. Foti and E. Rimini : J. Appl. Phys. 50, (1979)
- 3 C.M. Surko, A.L. Simons, D.H. Auston, J.A. Golovchenko and R.E. Slusher : Appl. Phys. Lett. 34, 635 (1979)
- 4 J.C. Schultz and R.J. Collins : Appl. Phys. Lett. 34, 363 (1979)
- 5 J.A. Van Vechten, R. Tsu and F.W. Saris : Phys. Lett. 74A, 417 (1979) and 74A, 422 (1979)
- 6 J.F. Morhange : Thesis, Paris (1982).
- 7 G. Kanellis, J.F. Morhange and M. Balkanski : Phys. Rev. B21, 1543 (1980)
- 8 J.S. Kasper and S.M. Richards : Acta Cryst. 17, 752 (1964)
- 9 J.C. Phillips, Comments Solid State Phys. 10, 165 (1982)
- 10 M. Balkanski, E. Haro, G.P. Espinosa, J.C. Phillips : Sol. Stat. Commun. 51, (1984)
- 11 P.L. Liu, R. Yen, N. Bloembergen and R.T. Hodgson : Mat. Res. Proc. Ed. White and Peercy (Academic Press), 1980, p. 156
- 12 J.M. Liu, R. Yen, H. Kurz and N. Bloembergen : Appl. Phys. Lett. 39, 755 (1981)
- 13 G.A. Rozgonyi, H. Baumgart, F. Phillipp, R. Uebbing and H. Oppolzer : Mat. Res. Soc. Proc. Ed. B.R. Appleton and B.K. Celler, (North Holland), 1982, p. 177
- 14 J.F. Morhange, G. Kanellis and M. Balkanski : Solid State Commun. 31, 805 (1979)
- 15 Y.I. Nissim, J. Sapriel and J.L. Oudar : Appl. Phys. Lett. 42, 504 (1983)
- 16 H.M. Van Driel, J.S. Preston and M.I. Galant : Appl. Phys. Lett. 40, 385 (1982)
- 17 C.V. Shank, R. Yen and C. Hirlimann : Phys. Rev. Lett. 50, 454 (1983)
- 18 J.M. Liu, H. Kurz and N. Bloembergen : Appl. Phys. Lett. 41, 643 (1982)
- 19 C.V. Shank, R. Yen and C. Hirlimann : Phys. Rev. Lett. 51, 900 (1983)  
D. Von der Linde and G. Wartmann : Appl. Phys. Lett. 41, 700 (1982)
- 20 D. Hulin, M. Combescot, J. Bok, A. Migus, J.Y. Vinet and A. Antonetti : Phys. Rev. Letters, 52, 1998 (1984)
- 21 M. Bensoussan and J. de Moison : Proceedings of the Intern. Conf. on the Physics of Semiconductors. Part I (Ed. by M. Averous, North Holland, Amsterdam) p. 404 (1982)
- 22 M. Balkanski, R.F. Wallis and E. Haro : Phys. Rev. B28, 1928 (1983)
- 23 A. Compaan : High Excitation and Short Pulse Phenomena, Trieste (1984)
- 24 J. Bok : Phys. Lett. 84A, 488 (1981)  
M. Combescot : Phys. Lett. 85A, 308 (1981)  
M. Combescot and J. Bok : Phys. Rev. Lett. 48, 1413 (1982)
- 25 R.M. Martin : Phys. Rev. 186, 871 (1969)

END

FILMED

11-84

DTIC